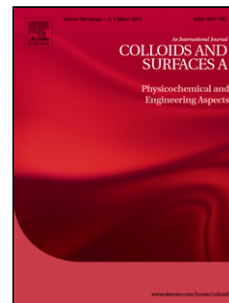


Accepted Manuscript

Title: Density Functional Theory Methods for
Characterization of Porous Materials

Authors: John Landers, Gennady Yu. Gor, Alexander V.
Neimark



PII: S0927-7757(13)00027-7
DOI: doi:10.1016/j.colsurfa.2013.01.007
Reference: COLSUA 18132

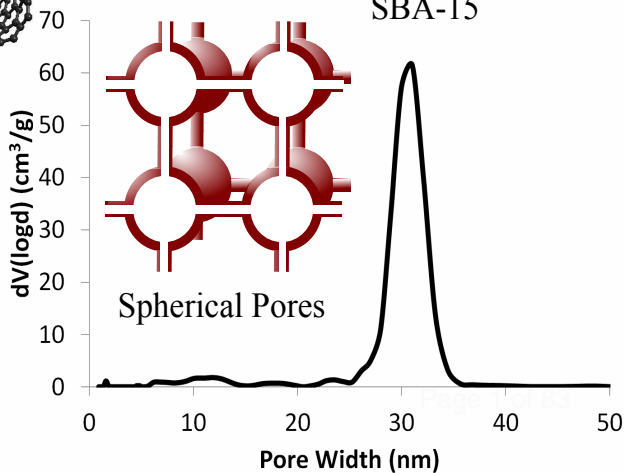
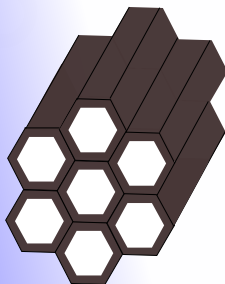
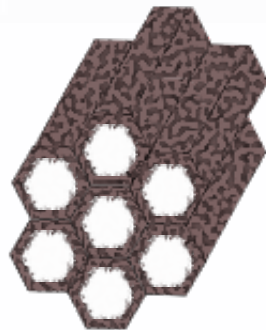
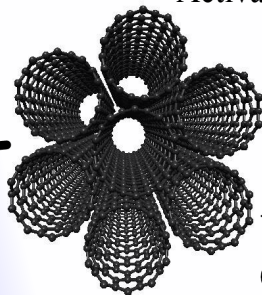
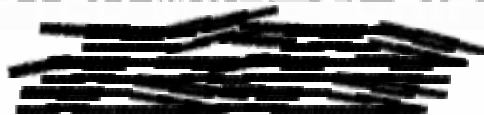
To appear in: *Colloids and Surfaces A: Physicochem. Eng. Aspects*

Received date: 19-11-2012
Revised date: 21-12-2012
Accepted date: 7-1-2013

Please cite this article as: J. Landers, G.Yu. Gor, A.V. Neimark, Density Functional Theory Methods for Characterization of Porous Materials, *Colloids and Surfaces A: Physicochemical and Engineering Aspects* (2010), doi:10.1016/j.colsurfa.2013.01.007

This is a PDF file of an unedited manuscript that has been accepted for publication. As a service to our customers we are providing this early version of the manuscript. The manuscript will undergo copyediting, typesetting, and review of the resulting proof before it is published in its final form. Please note that during the production process errors may be discovered which could affect the content, and all legal disclaimers that apply to the journal pertain.

Density Functional Theory



Density Functional Theory Methods for Characterization of Porous Materials

John Landers, Gennady Yu. Gor and Alexander V. Neimark¹

Rutgers University, Department of Chemical and Biochemical Engineering,

98 Brett Road, Piscataway, NJ 08854, USA

Abstract

This review presents the state-of-the-art of adsorption characterization of mesoporous and microporous materials by using the density functional theory (DFT) methods. The DFT methods have found numerous applications for calculating pore size distributions in traditional and newly discovered nanoporous solids. We discuss the foundations of the non-local (NLDFT) and quench solid (QSDFT) density functional theories applied for modeling adsorption and capillary condensation in pores of different geometry and surface chemistry. Special attention is paid to the limitations of the theoretical models and critical analysis of the obtained data. The methods are demonstrated on a wide variety of systems, including microporous and mesoporous carbons and silicas, zeolites, mesoporous crystals of MCM and SBA families, metal-organic frameworks, and other designer nanoporous materials. Illustrated with many typical examples and detailed discussions of the advantages and limitations of the NLDFT and QSDFT methods, this review provides guidance for the practitioners interested in getting a better understanding of the current capabilities and limitations of the adsorption methods for characterization of porous solids.

¹ Corresponding author, e-mail: aneimark@rutgers.edu

Outline:

1. Introduction
2. Description of density functional method (DFT)
 - 2.1. Non-local density functional theory (NLDFT)
 - 2.2. Drawbacks of NLDFT and paths to improvement
 - 2.3. Quenched solid density functional theory (QSDFT)
3. DFT methods for calculating the pore size distribution (PSD)
 - 3.1. General methodology
 - 3.2. Library of DFT kernels
 - 3.3. PSD analysis with different adsorbates
4. Applications of DFT kernels for carbonaceous and organic materials
 - 4.1. Microporous carbons: NLDFT model of slit-shaped pores
 - 4.1.1. Activated carbons
 - 4.1.2. Activated carbon fibers
 - 4.1.3. Carbon black, deposits and charcoal
 - 4.1.4. Carbon nanotubes
 - 4.1.5. Additional applications
 - 4.2. Improvement of pore structure characterization with QSDFT model
 - 4.3. Designer mesoporous carbons: hybrid QSDFT kernels
 - 4.3.1. Structures with mesopore channels: cylindrical pore model
 - 4.3.2. Structures with cage-like mesopores: spherical pore model
5. Applications of DFT kernels for silica and other inorganic materials
 - 5.1. MCM-41 as the reference material for pore structure characterization
 - 5.2. Gyroidal pore networks
 - 5.3. Accounting for microporosity
 - 5.3.1. SBA-15 as the case study system
 - 5.3.2. Zeolites
 - 5.3.3. Metal-organic frameworks and related structures
 - 5.4. Disordered structures
 - 5.5. Mesoporous crystals with cage-like pores: spherical pore model
 - 5.5.1. Cage-like structures with Pm3n and Im3m symmetry
 - 5.5.2. Cubic structures with Fd3m and Fm3m symmetry
 - 5.6. QSDFT model for silica materials
 - 5.7. Cavitation as a negative factor in pore size analysis
6. DFT models for interpretation of *in-situ* XRD data
7. Conclusions

1. Introduction

The breakthrough discovery in the early 1990's of highly ordered mesoporous materials [1, 2] stimulated rapid development of improved methods of pore structure characterization by gas adsorption. Indeed, the conventional methods, like BET [3] and BJH [4] models, failed to distinguish between different pore structure morphologies, to account for the effects of microporosity, and to predict the pore sizes, which could be independently determined from X-ray diffraction (XRD) and transmission electron microscopy (TEM) with the precision unavailable earlier. The new nanomaterials and new high-resolution experimental capabilities required new adequate theoretical methods for data analysis. This period coincided with the development of the density functional theory (DFT) for inhomogeneous and confined fluids [5-7], and, in particular with its application to the description of adsorption and capillary condensation in pores. In 1989, Seaton et al.[8] were the first to propose a DFT model for calculating the pore size distribution from adsorption isotherms, and it has been soon acknowledged that DFT provides a more reasoned and versatile approach to calculating the pore structure parameters compared to the conventional methods based on the Kelvin equation [9]. Initially developed for simple slit geometries for activated carbons, the so-called non-local density functional theory (NLDF) [10-12] soon evolved into a library of computational methods, which incorporates various pore structures representing characteristic pore morphologies and typical adsorbates. NLDF methods take into consideration the complexity associated with the hysteretic nature of adsorption isotherms that cloaks a number of physical phenomena relating to the geometrical specifics of a given pore structure. These phenomena include the inherent metastability of confined fluid, pore blocking and networking effects, as well as instability of adsorption films and cavitation in condensed fluid. But with the arrival of newer and more distinct DFT methods, as opposed to just one conventional BJH method, also

came a problem of choice. Which DFT model should be employed for this or that particular system? Which branch of the hysteretic isotherm should be used for analysis? The latter question is extremely important, since the choice of the isotherm branch may lead to considerably different pore size distribution results. The DFT approach solves, at least partially, this problem by offering different methods for treating adsorption and desorption isotherms, which produce consistent results.

The purpose of this review is to present the current state and capabilities of the DFT methods for pores structure characterization and to provide a practical guidance on the choice of the most suitable method from the currently available library of DFT kernels for particular applications. The rest of the paper is structured as follows. In section 2, a description is given of the essence of the NLDFT methodology and its evolution into a versatile tool applicable for various pore structures. This section also includes a description of the more advanced quenched solid density functional theory (QSDFT) method, which takes into account roughness and heterogeneity of the pore wall surfaces. Section 2 can be skipped by a reader interested only in practical applications of the DFT method for characterization. Section 3 shows how these methods are used to interpret the experimental isotherms and to produce the pore size distributions. Section 4 and section 5 presents numerous examples of DFT method applications for different materials of distinct pore structures for organic and inorganic materials, respectively. The DFT models are then correlated and interpreted with in situ x-ray diffraction data in section 6. Finally, section 7 contains concluding remarks and future outlook.

2. Description of density functional method (DFT)

In their seminal work, Seaton et al. [8] were the first to apply the density functional method for the determination of pore size distribution from adsorption isotherms. They

suggested a method for treating nitrogen adsorption measurements on porous carbons based on the local mean field approximation [5-7]. A further significant improvement was made by Lastoskie et al [10], who used a NLDFT model within Tarazona smooth density approximation [13] for modeling nitrogen adsorption on carbons. Both works treated the pores as infinite slits, which is a conventional model representation of pores between graphene fragments in carbons. Near the same time, Mobil scientists developed MCM-41 mesoporous silicas with ordered hexagonal structure of cylindrical channels, which for the first time provided the opportunity for verification of the theoretical methods of pore structure analysis against reliable experimental data [1, 2]. The NLDFT model for adsorption on MCM-41 suggested and verified by Neimark and Ravikovitch [12, 14, 15] became the starting point for further development of customized DFT methods applicable for mesoporous and hybrid materials of various morphologies. With this assembly of contributions, the NLDFT method soon became widely accepted to the extent that it has been recommended as the standard method by the International Standard Organization (ISO) [16].

2.1 Non-Local Density Functional Theory (NLDFT)

The adsorption experiment, which is performed by equilibrating the solid-fluid (adsorbent-adsorbate) system at a given temperature at a set of adsorbate gas pressures, corresponds to the conditions of the grand canonical ensemble for the system of fixed chemical potential, volume, and temperature. Therefore, the equilibrium distribution of the adsorbate in the pores corresponds to a minimum of the grand potential of the adsorption system presented as a functional of the density of adsorbed fluid. Within the conventional treatment of adsorption, the solid adsorbent is considered as inert and non-deformable, and the adsorption interactions are modeled with an effective solid-fluid spatially distributed potential $U_{ext}(\mathbf{r})$. With this

assumption, the equilibrium adsorption state at a given chemical potential of the fluid μ_f is determined in NLDFT [10, 12] from the minimization of the grand potential Ω_f of the fluid confined in the pore and subjected to the external potential U_{ext} ,

$$\Omega_f[\rho_f(\mathbf{r})] = F_f[\rho_f(\mathbf{r})] - \int d\mathbf{r} \rho_f(\mathbf{r}) [\mu_f - U_{ext}(\mathbf{r})]. \quad (1)$$

Here \mathbf{r} is a position vector inside the pore, $\rho_f(\mathbf{r})$ is the fluid density, and F_f is the Helmholtz free energy of the fluid. The latter is expressed as a sum of the ideal term $F_{id}[\rho_f(\mathbf{r})]$, excess hard sphere (HS) repulsion term $F_{ex}[\rho_f(\mathbf{r})]$ and the attractive term calculated in a mean-field fashion given by the equation:

$$F_f[\rho_f(\mathbf{r})] = F_{id}[\rho_f(\mathbf{r})] + F_{ex}[\rho_f(\mathbf{r})] + \frac{1}{2} \iint d\mathbf{r} d\mathbf{r}' \rho_f(\mathbf{r}) \rho_f(\mathbf{r}') u_{ff}(|\mathbf{r} - \mathbf{r}'|), \quad (2)$$

where $u_{ff}(r)$ is the attractive part of the pairwise fluid-fluid potential. The fluid density profile $\rho_f(\mathbf{r})$ is thus obtained from the minimization of the grand potential (1). Once the equilibrium distribution of the fluid density is determined at each value of the chemical potential μ_f , and its averaged values calculated, the adsorption isotherm can be obtained. Different models were suggested in the literature for the excess HS free energy $F_{ex}[\rho_f(\mathbf{r})]$ (see e.g. review [17]). The most popular are the smooth density approximation (SDA) of Tarazona [13], the fundamental measure theory (FMT) of Rosenfeld [18, 19], and their modifications based on either Percus-Yevick (PY) or Carnahan-Starling (CS) equations of state. Explicit expressions can be found elsewhere [12, 20]. It is worth noting, that different versions of DFT are not in conflict, as long as the fluid-fluid interaction parameters are adjusted to match the vapor-liquid equilibrium within the range of temperatures used in adsorption measurements. As such, different versions of hard sphere density functionals may employ different sets of input parameters. With such adjustment,

the quantitative results obtained with different functional may deviate beyond the accuracy required for the pore size distribution calculations.

The pore structure characterization is based on the physical adsorption of non-specific gases, like nitrogen and argon, which is governed mainly by dispersion interactions, that justifies the use of Lennard-Jones (LJ) intermolecular potentials for both fluid-fluid and solid-fluid interactions. The attractive part of the fluid-fluid potential $u_{ff}(r)$ for LJ model adsorbates is commonly treated with the Weeks–Chandler–Andersen (WCA) scheme [21],

$$u_{ff}^{\text{attr}}(r) = \begin{cases} -\varepsilon_{ff} & r \leq 2^{1/6} \sigma_{ff} \\ 4\varepsilon_{ff} \left[\left(\sigma_{ff}/r \right)^{12} - \left(\sigma_{ff}/r \right)^6 \right] & r > 2^{1/6} \sigma_{ff} \end{cases} \quad (3)$$

where ε_{ff} and σ_{ff} are the energy and size parameters of the LJ potential. In order to provide a correct equation of state for the adsorbate, the fluid-fluid parameters ε_{ff} and σ_{ff} should be fitted by correlating the experimental data on liquid-vapor equilibrium, gas densities, saturation pressure and surface tension with the predictions obtained with the particular functional for the bulk fluid for liquid as described by Ravikovitch et al [15].

The solid-fluid interactions in the DFT models used for pore structure characterization are commonly based on effective potentials obtained by integrating pair-wise solid-fluid LJ potential $u_{sf}(r)$ for a given pore geometry. The Steele equation[22], which assumes a graphite pore wall of infinite thickness, is conventionally employed for the slit shape carbon pores. The curvature effects in cylindrical and spherical pores are accounted for by integrating the solid-fluid LJ potential over the cylindrical and, respectively, spherical outer layer of solid atoms (carbons in case of carbonaceous materials and oxygen in case of oxides, like silica). Although the integrated potentials ignore the real molecular structure of the pore wall, they capture the main contribution from most attractive centers. It is worth noting, that the parameters of the

solid-fluid interaction in these potentials are fitted to the experimental data on reference non-porous surfaces, and this fitting compensates for the lack of structural details in the chosen mathematical expression for the integrated potential. The respective equations are given in [12] and [23]. Within this framework, the adsorption interactions are characterized by the solid-fluid LJ parameters ϵ_{sf} and σ_{sf} which should be fitted by correlating the experimental data on adsorption on a reference non-porous solid with the predictions obtained with the DFT model for the flat surface [15]. These parameters depend on the adsorbate-solid pair and are customized for the materials of different origin and the adsorbate employed for surface and pore size characterization. The fluid-fluid and solid-fluid parameters employed in the DFT models for carbons and silicas [24, 25] are presented in Table 1.

NLDFT interaction parameters					
NLDFT		fluid-fluid parameters		solid-fluid parameters	
adsorbent	adsorbate	ϵ_{ff}/k_B (K)	σ_{ff}, d_{hs} (Å)	ϵ_{sf}/k_B (K)	σ_{sf} (Å)
silica/zeolite	N ₂ at 77.4 K	94.45	3.575 (3.575)	147.25 (22.53)	3.17
	Ar at 87.3 K	118.05	3.305 (3.39)	171.24 (26.20)	3.00
	Kr at 153 K	162.6	3.627	109.6	3.45
	Xe at 180 K	227.6	3.901	128.2	3.586
carbon	N ₂ at 77.4 K	94.45	3.575 (3.575)	53.22	3.494
	Ar at 87.3 K	118.05	3.305 (3.39)	55.0	3.35

Table 1. Molecular interactions LJ parameters of nitrogen and argon[15, 24], krypton and xenon [25] adsorption on silica and carbon surface used in NLDFT method. Hard sphere diameters are given in brackets. Note that for the solid fluid integrated LJ potentials employed in the NLDFT kernels for silicas the magnitude of adsorption energy is accounted as the product of the center density times the pairwise interaction energy $\rho_s \epsilon_{sf}/k_B$ (given in brackets; for ϵ_{sf}/k_B the surface density was assumed equaled to $\rho_s = 15.3 \text{ nm}^{-2}$). For carbon, the reported solid-fluid parameters correspond to the parameters of the Steele equation [22].

Theoretical adsorption isotherms calculated using the NLDFT model have been validated against the experimental adsorption and desorption isotherms on mesoporous crystals of MCM 41 and SBA-15 types with well characterized cylindrical pores [14, 26]. A typical example of nitrogen adsorption on an MCM-41 sample with 4.8 nm pores is shown in Figure 1. Within the NLDFT models, the position of capillary condensation in cylindrical pores is associated with so-called mechanism of delayed, or spinodal condensation occurring at the limit of stability of adsorption films, or at the vapor-liquid spinodal. The position of desorption is associated with the equilibrium capillary-condensation-evaporation transition. Also, the NLDFT model calculations performed with periodic boundary conditions predicts the metastable states on the desorption isotherm at the pressures smaller than the equilibrium pressure down to the liquid-vapor spinodal, or the limit of stability of overstretched fluid. However, these metastable states can be observed experimentally only in the ink-bottled and corrugated pores [27, 28]. It was shown that the NLDFT model can precisely predict the capillary condensation and desorption pressures in cylindrical pores wider than ~5 nm, when desorption is associated with an apparent hysteresis: as the vapor pressure decreases, the desorption occurs at a pressure lower than the pressure of condensation. In smaller pores, the experimental hysteresis progressively diminishes and the adsorption isotherm merges with the desorption isotherm, which corresponds to the equilibrium capillary condensation-evaporation transition, for pores smaller than ~4 nm. In pores smaller than 5 nm, the NLDFT adsorption isotherms progressively deviate from the experimental isotherm since the NLDFT model does not account for the nucleation phenomenon. This feature of the NLDFT isotherms is illustrated in Figure 2 with examples of Ar adsorption on a series of MCM-41 samples [29]. The authors [29] suggested to distinguish three regimes of adsorption behavior: regime of developed hysteresis (pores of ~5 nm and wider), regime of reversible

condensation (pores smaller than so-called hysteresis critical pore size, which is ~ 4 nm); and regime of developing hysteresis in intermediate pores, where the capillary condensation occurs at experimental conditions somewhat in between theoretical spinodal and equilibrium.

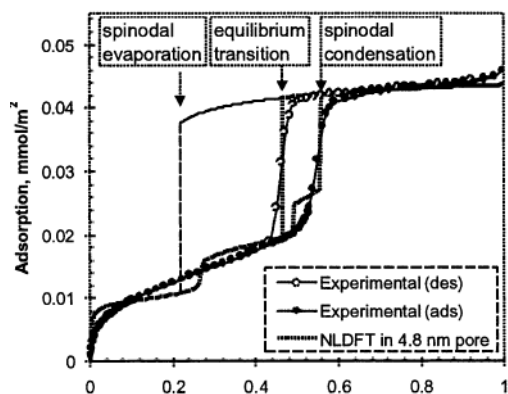


Figure 1. Experimental nitrogen (at 77.4 K) adsorption isotherm on MCM-41 silica and theoretical NLDFT isotherm in 4.8 nm cylindrical pore. (Adapted from [24].)

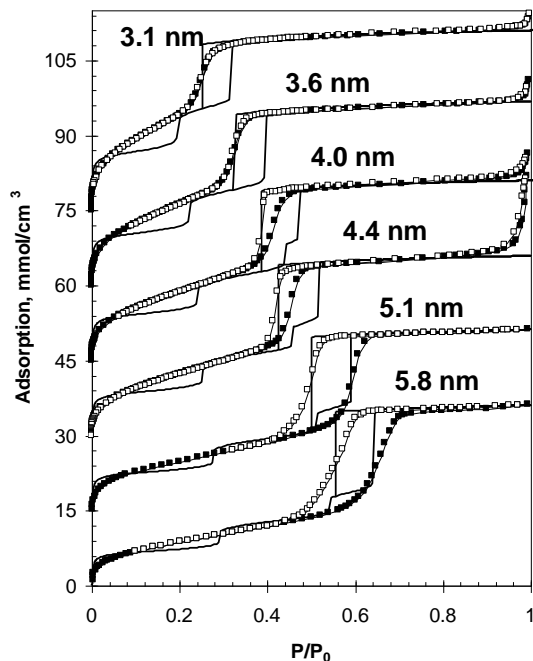


Figure 2. Experimental adsorption and desorption isotherms of Ar (at 87 K) on a series of mesoporous molecular sieves with cylindrical pores of characteristic diameter 3.1, 3.6, 4.0, and 4.4 nm [14], and 5.1 and 5.8 nm [30] (points) and theoretical isotherms calculated using NLDFT (solid lines). (Adapted from ref. [29])

As such, the NLDFT equilibrium isotherms in cylindrical pores can be used for calculations of the pore size distributions from the desorption branches of hysteretic adsorption

isotherms, as well as from the reversible isotherms. In the range of pores wider than ~5nm, the NLDFT adsorption isotherms can be used for calculations of the pore size distributions from the adsorption branches of H1 hysteresis loops. This conclusion is confirmed in Figure 3 by the compendium of independent experimental data of the pore sizes of MCM-41 and SBA-15 samples compared with the NLDFT predictions of the positions of capillary condensation and desorption. The agreement with experiments is excellent, in contrast to the predictions of the conventional Kelvin-Cohan equation [9] (the basis of the BJH method), which progressively underestimate the pore sizes at the nanoscale below 20 nm. This is one of the main advantages of the NLDFT method.

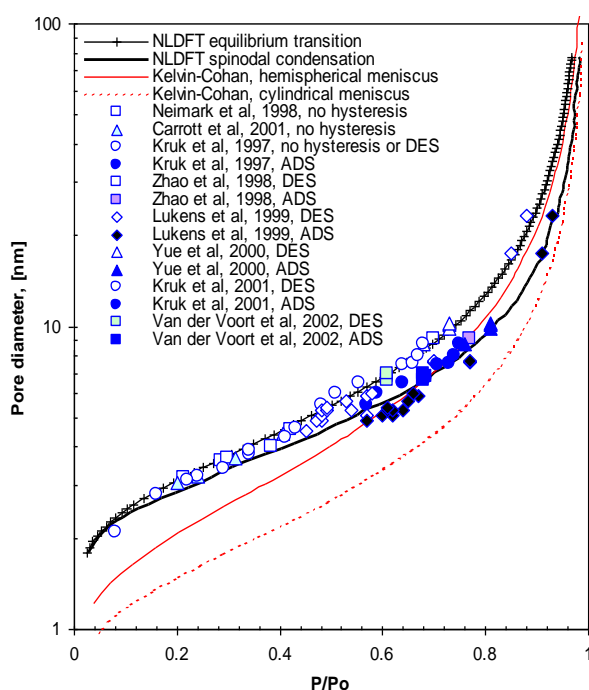


Figure 3. Relative pressures of the adsorption and desorption for N₂ (at 77 K) in open cylindrical pores in comparison with the experimental data [14, 27, 30-34] on ordered MCM-41 and SBA-15 nanoporous materials with cylindrical pores. Predictions of the macroscopic Kelvin-Cohan equation are also shown. (Adapted from ref. [29])

The mechanisms of capillary condensation hysteresis in cage-like pore networks are different from those in cylindrical pores due to the presence of the connecting channels (necks)

or openings. The NLDFT method was extended to the spherical shape pore geometry to model adsorption in cage-like mesoporous materials [23]. Experimental observations with specially designed ordered materials and respective theoretical analysis revealed three different mechanisms of evaporation from cage-like mesopores [35]: (i) pore blocking controlled desorption, (ii) spontaneous evaporation due to cavitation, and (iii) near-equilibrium desorption. A typical example of experimental and NLDFT isotherms for a material with cage-like pores is given in Figure 4. The prevalence of a given mechanism, and thus the pressure p_d at which desorption occurs, depends mainly on the relation between the size of the cavity and the size of the necks. Near-equilibrium desorption is possible from the cavities that have immediate access to the vapor phase through relatively wide openings, and thus are effectively unblocked. Once the vapor pressure reaches the vapor-liquid equilibrium (VLE) pressure p_e , desorption from the main cavity proceeds via a receding meniscus; therefore $p_d \approx p_e$. However, if wide cavities are connected with narrower necks, so that the fluid in the neck has a lower VLE pressure than that of the fluid in the cavity, the neck effectively “blocks” desorption from the cavity. Emptying of the pores occurs at the pressure of equilibrium desorption of the neck, and as such becomes a function of the neck size. Finally, if the connecting necks are even narrower, fluid in the cavity becomes substantially metastable, and the vapor pressure may reach the spinodal point of the confined liquid before the equilibrium meniscus can be formed in the neck. Thus, the fluid desorbs from the pore by the cavitation mechanism, which involves fluctuation-driven formation and growth of a bubble. In this scenario, $p_d \ll p_e$, and p_d has little or no dependence on the size of the necks. Due to these peculiarities of adsorption hysteresis in the cage-like pores, NLDFT methods should be applied carefully, taking into account the physical origin of the desorption branch of the experimental isotherm.

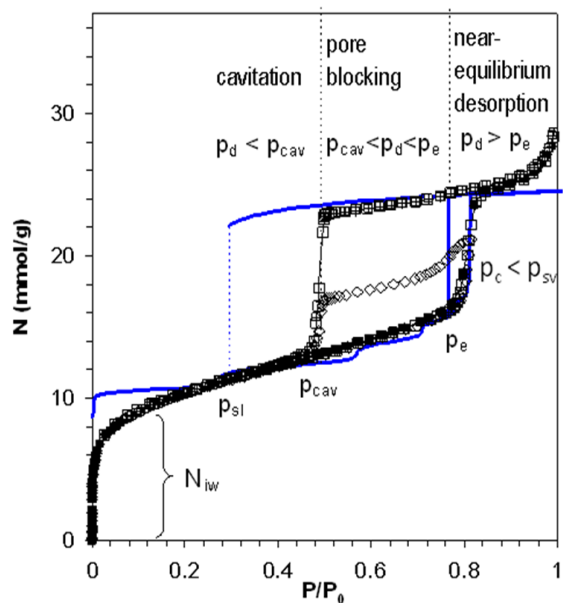


Figure 4. NLDFT N_2 adsorption-desorption isotherm (at 77 K) in 15.5 nm spherical cavity (thick solid line) and experimental data on a FDU-1 silica sample (points). The theoretical pressures of liquid like spinodal, equilibrium, and vapor like spinodal are denoted, respectively, as p_{sl} , p_e , and p_{sv} . Experimentally observed pressures of spontaneous capillary condensation and cavitation are denoted as p_c and p_{cav} , respectively ($p_c \approx p_{sv}$ and $p_{sl} < p_{cav} < p_e$). Three possible regimes of evaporation from the cavity are classified with respect to the pressure p_d of desorption from the neighboring pores or from the pore neck. Reproduced from ref. [35]

Lastly, the hybrid NLDFT methods, which combine the theoretical isotherms in pores of different shapes (slit, cylindrical, and spherical) in different diapasons of pore sizes have been developed for the characterization of a variety of ordered and hierarchically structured microporous materials [36]; the latter are discussed in section 4.3.

2.2 Drawbacks of NLDFT and paths to improvement

Most adsorbents have a molecularly rough microporous surface. A drawback to the standard NLDFT method is that it does not take into account chemical and geometrical heterogeneity of the pore walls, instead assuming a structureless, chemically and geometrically smooth surface model. The consequence of this mismatch between the theoretical assumption of smooth and homogeneous surfaces and the inherent molecular scale heterogeneity of real adsorbents is that the theoretical NLDFT adsorption isotherms exhibit multiple steps. These steps

are associated with a layering transition related to the formation of a monolayer, second adsorbed layer, and so on (see examples in Figures 1, 2, 4). The problem is enhanced in microporous carbon materials, which exhibit broad PSDs, where the artificial layering steps inherent to the theoretical isotherms cause artificial gaps on the calculated pore size distributions around 1 and 2 nm [15, 37] (see discussion in section 4.2). There were multiple attempts to improve the NLDFT method to avoid artificial layering on theoretical isotherms.

Olivier [38] introduced a modification to the mean field approximation, which allowed him to obtain good agreement with experimental isotherms for argon and nitrogen adsorption on non-porous surface and in slit pores. He further suggested to use a combination of modified DFT isotherms to mimic the real heterogeneous surface [37]. A different extension of NLDFT for carbons was suggested by Nguyen and Bhatia [39]. This approach was based on a model of carbon wall heterogeneity, assuming the varying thickness of the pore walls [40, 41]. While such an approach smoothened the NLDFT adsorption isotherms, making them closer to the experimental ones, it required, along with the unknown pore size distribution, the introduction of an unknown distribution of the pore wall thickness. The latter can be hardly verified against experimental data for disordered materials, and so to some extent is arbitrary. Another modification of the Tarazona's NLDFT capable of generating smooth isotherms in the region of mono- and polymolecular adsorption was further developed by Ustinov et al. [42-45]. The authors used the WCA scheme (Eq. 3) for solid-fluid attractive interactions and reduced the contribution from the HS repulsive interactions in the vicinity of the solid surface, which decreases the layered structure of the fluid. The parameters of the model were fitted to obtain good agreement with experimental nitrogen and argon adsorption data on MCM-41[44], nonporous amorphous silica[43], and carbon[45]. An alternative method was suggested by Jagiello and Olivier [46, 47], who reached a better agreement between NLDFT and experimental

isotherms for nitrogen adsorption on porous carbons by introducing the two-dimensional finite pore model instead of standard one dimensional model that assumes infinite graphite-like pores. It should be noted that this record of the literature is not comprehensive and is limited to the most prominent modifications.

Recently, the NLDFT method was advanced to take into account the molecular level surface roughness that is typical to most carbonaceous and siliceous materials as well as other materials including hybrid organic-inorganic hierarchical structures [48]. This technique, named the quenched solid density functional theory (QSDFT), was shown to be more practical than NLDFT for the analysis of microporous and mesoporous silicas [48, 49] and carbons [20, 50].

2.3 Quenched Solid Density Functional Theory (QSDFT)

Within the framework of QSDFT, the grand potential of both the solid and fluid are considered. Unlike the conventional NLDFT, QSDFT implies a two-component density functional, where the solid is modeled as a compound of hardcore spheres interacting with the fluid molecules via a pairwise attractive potential. From Eqs. (1) and (2), the grand potential of the solid-fluid system Ω_{sf} is written as

$$\begin{aligned}\Omega_{sf}[\rho_s(\mathbf{r}), \rho_f(\mathbf{r})] = & F_{id}[\rho_f(\mathbf{r})] + F_{id}[\rho_s(\mathbf{r})] + F_{ex}[\rho_s(\mathbf{r}), \rho_f(\mathbf{r})] \\ & + \frac{1}{2} \iint d\mathbf{r} d\mathbf{r}' \rho_f(\mathbf{r}) \rho_f(\mathbf{r}') u_{ff}(|\mathbf{r} - \mathbf{r}'|) + \frac{1}{2} \iint d\mathbf{r} d\mathbf{r}' \rho_s(\mathbf{r}) \rho_s(\mathbf{r}') u_{ss}(|\mathbf{r} - \mathbf{r}'|) \\ & + \iint d\mathbf{r} d\mathbf{r}' \rho_f(\mathbf{r}) \rho_s(\mathbf{r}') u_{sf}(|\mathbf{r} - \mathbf{r}'|) - \mu_f \int d\mathbf{r} \rho_f(\mathbf{r}) - \mu_s \int d\mathbf{r} \rho_s(\mathbf{r})\end{aligned}\quad (4)$$

where $\rho_s(\mathbf{r})$ is the density profile of the solid component, $F_{id}[\rho_s(\mathbf{r})]$ is the ideal contribution of hard-sphere free energy of the solid, $F_{ex}[\rho_s(\mathbf{r}), \rho_f(\mathbf{r})]$ is the excess HS free energy term for both the solid and fluid components, $u_{ss}(r)$ and $u_{sf}(r)$ are the attractive parts of the solid-solid and solid-fluid potentials respectively, and μ_s is the chemical potential of the solid. The key

component in the QSDFT approach displayed in Eq. (4) is the $F_{ex}[\rho_s(\mathbf{r}), \rho_f(\mathbf{r})]$ term, known as the excess free energy of the solid-fluid HS mixture. To calculate this term, Rosenfeld's fundamental measure theory, the so called RLST approximation [18, 19] was employed, which is consistent with the Percus-Yevick equation of state for bulk HS fluids (see details in [20]).

The essence of QSDFT model is related to the “quenched” state of the solid. While the authors take into account the density of the solid component, $\rho_s(\mathbf{r})$, they do not vary it while optimizing the grand potential Ω_{sf} . Thus only those terms that are related to the fluid in Eq. (4) are subject to minimization. The final density profile is found from the condition

$$\left. \frac{\delta \Omega[\rho_s(\mathbf{r}), \rho_f(\mathbf{r})]}{\delta \rho_f(\mathbf{r})} \right|_{\rho_s(\mathbf{r})} = 0, \quad (5)$$

which finally leads to the solution of the Euler-Lagrange equation

$$\rho_f(\mathbf{r}) = \Lambda_f^{-3} \exp \left\{ c^{(1)}(\mathbf{r}, [\rho_s, \rho_f]) - \beta \int d\mathbf{r}' \rho_f(\mathbf{r}') u_{ff}(|\mathbf{r} - \mathbf{r}'|) + \beta \mu_f - \beta \int d\mathbf{r}' \rho_s(\mathbf{r}') u_{sf}(|\mathbf{r} - \mathbf{r}'|) \right\} \quad (6)$$

where $c^{(1)}(\mathbf{r}, [\rho_s, \rho_f]) = -\beta \delta F_{ex}[\rho_s(\mathbf{r}), \rho_f(\mathbf{r})] / \delta \rho_f(\mathbf{r})$ is the one-particle direct correlation function expressed as the functional derivative of the excess Helmholtz free energy of the two-component HS fluid, which depends on both solid and fluid densities. Here $\beta = 1/k_B T$, k_B is the Boltzmann constant, T is the absolute temperature, $\Lambda_f = h / (2\pi m k_B T)^{1/2}$ is the thermal de Broigle wavelength, h is the Planck constant, and m is the molecular mass of the fluid molecule.

The solid density profile $\rho_s(\mathbf{r})$ takes into account the molecular level geometrical heterogeneity of pore walls, known as the “corona” in XRD studies of mesoporous crystals of SBA-15 type [51]. The solid density profile for mesoporous crystals can be calculated from the reconstruction of XRD patterns [52, 53] or from the molecular dynamics simulations of real surfaces of amorphous solids [54-56]. For the practical calculations the density profile for most

surfaces can be approximated by the simplest function with a linear gradient, varying from the density of solid to null. Thus, within the corona, the molecular level roughness is accounted by one main parameter δ equal to the half width of the corona. As such, the solid density profile is defined by

$$\rho_s(z) = \begin{cases} \rho_s^0 & 0 \leq z < h_0 \\ C\rho_s^0 \left(1 - \frac{z-h_0}{2\delta}\right) & h_0 \leq z < h_0 + 2\delta \\ 0 & h_0 + 2\delta \leq z \end{cases} \quad (7)$$

Here z is the distance from the pore wall, ρ_s^0 is the bulk density of the adsorbent, C is the constant (which is set to 1 for most of the surfaces, including silica), h_0 is the thickness of the solid wall, and δ is the roughness parameter, which represents the half-width of the region of variable solid density. The position of the edge of the solid, which is responsible for the pore size D is discussed in section 3 and is determined from the condition of zero solid excess. The values of these parameters for silica and carbon are given in Table 2. Note that for silica $C = 1$, i.e. the simple linear ramp is used; otherwise the roughness parameter is determined from XRD data [57]. For carbons, based on the properties of the reference material (Cabot BP-280 carbon black with a partial degree of graphitization) the solid density has a more complex profile [20]. Fluid-fluid and solid-fluid molecular interactions parameters for characteristic systems are summarized in Table 3. Note that the parameters of solid-fluid potentials are different from those used in NLDFT kernels because of the use of different approaches for accounting for intermolecular interactions. In QSDFT, the pairwise LJ potentials are used, instead of integrated LJ potentials in NLDFT silica kernels and Steele potential in NLDFT carbon kernels. In the latter case the difference is very significant. The fluid-fluid parameters in QSDFT and NLDFT are different because of the use of different hard sphere reference functionals.

In general, the solid-fluid parameters should be customized for given adsorbent-adsorbate pair. However, this is a tedious work, which can be done only when the reference isotherm is available. Alternatively, the existing kernels for carbons and silicas can be used for evaluating the pore structure of organic and inorganic materials, respectively.

An example of a QSDFT calculation for the adsorption-desorption cycle of Kr at 119 K on SBA-15 sample is given in Figure 5a. This sample shows excellent agreement with the experimental adsorption data without any adjustable parameters. The roughness parameter was defined from XRD data. Figure 5b shows solid and fluid density profiles at different pressure values.

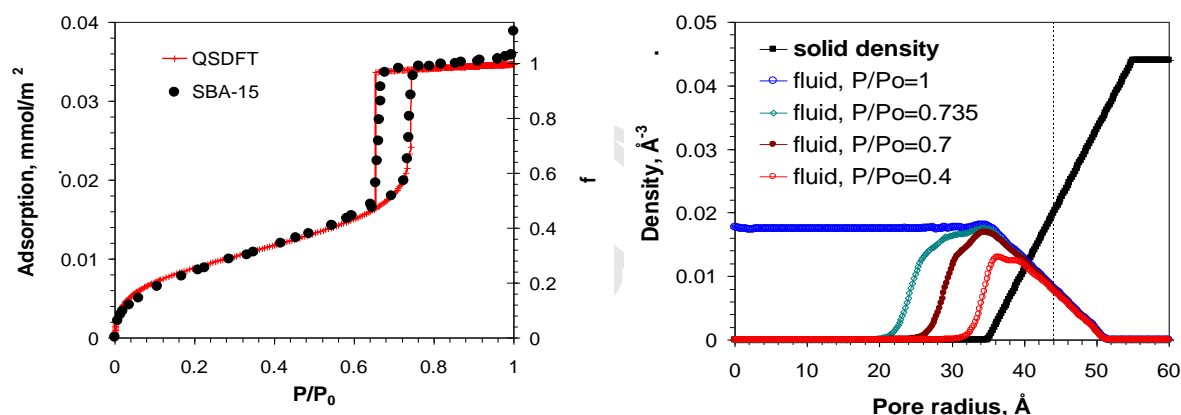


Figure 5. (a) Prediction of krypton adsorption on SBA-15 silica at 119 K. Experimental data are from ref. [57] (b) Density profiles of solid (squares) and fluid at different pressures along the adsorption branch. Thin vertical line at $r = 43.9\text{\AA}$ indicates the pore radius at which the excess fluid density is zero. The solid excess mass is zero at $r = 45\text{\AA}$. Reproduced from ref. [48]

QSDFT solid density distribution parameters					
adsorbent	$\rho_s^0 (\text{m}^{-3})$	C	$h_0 (\text{nm})$	$\delta (\text{nm})$	d_{HS}
silica	4.4×10^{28}	1.0	2×0.34	0.4	0.3
carbon	1.14×10^{29}	0.75	2×0.34	0.13	0.2217

Table 2. Parameters of the solid density distribution in QSDFT models.

QSDFT interaction parameters					
QSDFT		fluid-fluid parameters		solid-fluid parameters	
adsorbent	adsorbate	ϵ_{ff}/k_B (K)	$\sigma_{ff} = d_{hs}$ (Å)	ϵ_{sf}/k_B (K)	σ_{sf} (Å)
silica/zeolite	N ₂ at 77.4 K	95.77	3.549	148.45	3.17
	Ar at 87.3 K	111.95	3.358	160.5	3.104
	Kr at 119 K	155.9	3.589	189.4	3.22
carbon	N ₂ at 77.4 K	95.77	3.549	150	2.69
	Ar at 87.3 K	111.95	3.358	162.18	2.595

Table 3. Parameters of nitrogen [49], argon and krypton adsorption on silica [48], nitrogen and argon on carbon [20] surface used in QSDFT method. Usually the fluid-fluid interactions are truncated at $5\sigma_{ff}$.

3. DFT methods for calculating the pore size distribution (PSD)

3.1. General methodology

The PSD is calculated from the experimental adsorption isotherm $N_{\text{exp}}(P/P_0)$ by solving the integral adsorption equation [8]. The experimental isotherm is represented as the convolution of the DFT kernel (set of the theoretical isotherms $N_{\text{QSDFT}}(P/P_0, D)$ in a series of pores within a given range of pore sizes D) and the unknown PSD function $f(D)$,

$$N_{\text{exp}}(P/P_0) = \int_{D_{\min}}^{D_{\max}} N_{\text{QSDFT}}(P/P_0, D) f(D) dD. \quad (8)$$

Here D_{\min} and D_{\max} are the minimum and maximum pore sizes in the kernel, respectively. Two kernels of the selected DFT adsorption isotherms for the slit geometry are presented in Figure 6,

(a) NLDFT and (b) QSDFT. In contrast to the NLDFT kernels, the QSDFT isotherms are smooth prior to the capillary condensation step, which is characteristic of mesopores ($D > 2$ nm), and thus do not exhibit stepwise inflections caused by artificial layering transitions.

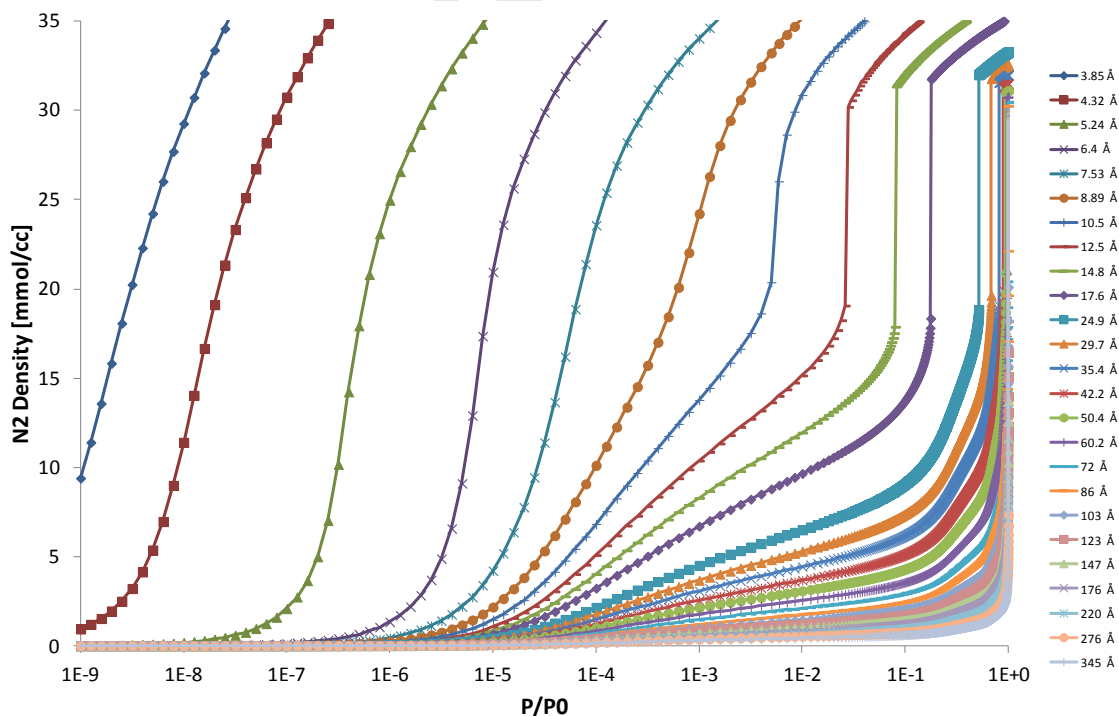
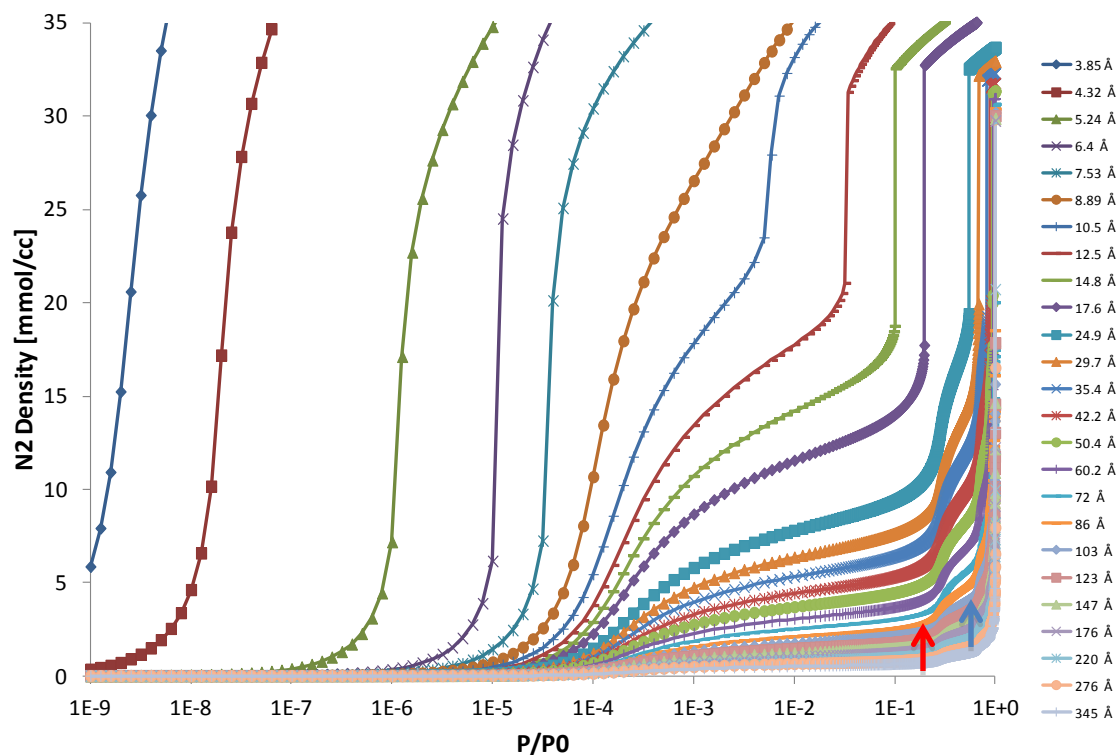


Figure 6. Kernels of selected equilibrium nitrogen at 77.4 K adsorption isotherms in slit-shaped carbon pores, calculated using (a) NLDFT (smooth pore walls) and (b) QSDFT (molecularly rough surface). Red and blue arrows show the positions of the NLDFT isotherm steps corresponding to the first and second layer formation, respectively. These steps are mistaken in the PSD calculations with the capillary condensation steps in pores of ~ 1 and ~ 2 nm, respectively.

Solution of Eq. (8) can be obtained using the quick non-negative least square method [58]. In this method Eq. (8) is represented as a matrix equation, which is solved using the discrete Tikhonov regularization method combined with the non-negative least square algorithm [59]. All examples of PSDs presented below were calculated by using this efficient scheme. At the same time, it is worth noting that in the literature one can find several alternative techniques for the solution of Eq. 8, and the results obtained with different regularization techniques may deviate (see e.g. [60] and references therein).

It should be noted that in NLDFT kernels, the pore width is defined as the center-to-center distance between the outer layers of adsorption centers on the opposite pore walls corrected for the solid-fluid LJ diameter. In QSDFT kernels, the pore width is defined from the condition of zero solid density excess. These definitions are apparently different, albeit insignificantly, but this difference should be taken into account in data analysis.

3.2 Library of DFT kernels

Over the years a library of NLDFT [14, 15, 23, 26, 36, 52] and more recently QSDFT [20, 48-50, 53, 61] kernels were developed for calculating pore size distributions in carbonaceous and silica micro- mesoporous materials of different origin from nitrogen and argon

adsorption isotherms, as well as for microporous carbons from carbon dioxide adsorption [15]. For a DFT kernel of a given adsorbate-adsorbent pair, the parameters should not only represent the specifics of adsorbent-adsorbate interactions, but also take into account the pore structure morphology. The latter is accounted by the choice of the characteristic pore geometry represented by cylindrical, spherical, and slit model pores. Hybrid kernels, which use different pore geometries within different ranges of pore sizes, were developed to characterize hierarchical structures that combine different type pores over a wide range of scales [23, 35]. The kernels were verified on the well-characterized materials like mesoporous crystals, zeolites, and active carbons with independently determined pore sizes. To treat hysteretic adsorption-desorption isotherms, two kernels were developed for adsorption and desorption branches. These kernels imply different physical mechanisms for capillary condensation and evaporation. Adsorption kernels are composed of theoretical adsorption isotherms accounting for the delayed condensation effect. Equilibrium kernels are composed of theoretical adsorption isotherms with the position of vapor-liquid phase transition determined from the condition of phase equilibrium. While the adsorption kernels should be applied only for adsorption branches of hysteretic isotherms, the equilibrium kernels can be used for both the desorption and adsorption branch depending on the system and the pore range. Some hybrid kernels combine equilibrium isotherms in the range of micropores and small mesopores ($< \sim 4$ nm), in which the hysteresis is not experimentally observed due to inherent thermal and mechanical fluctuations that disturb metastable states. The desire of the developers was to design the kernels, which would provide consistent results while calculating the pore size distributions using different adsorbates and, in the case of hysteresis, use different branches of the isotherm. It is worth noting that at this moment all DFT methods rely upon the models of independent pores and do not take into account cooperative adsorption and desorption mechanism, which may be important for pore

networks. At the same time, customization of characterization methods based on different adsorption-desorption mechanisms and different pore geometries is a big step forward compared to conventional BJH method. Moreover, since the DFT models provide important corrections for the Kelvin equation at the nanoscale, the results of PSD calculations are more reliable as confirmed by the broad experimental validation.

A brief overview of the available DFT kernels and basic recommendation for their applicability are given in Section 4 and Section 5 with typical examples of application of these kernels to different types of carbonaceous and silica materials, respectively.

3.3. PSD analysis with different adsorbates

DFT kernels were built for calculating PSD using different adsorbates: nitrogen at 77.4 K, argon for 77.4 and 87.3 K, and carbon dioxide at 273 K. It was shown, that the results obtained with different adsorbates are in reasonable agreement [15]. Nitrogen at 77.4 K is the conventional adsorbate for adsorption characterization. However, argon and carbon dioxide are more suitable in some cases, especially for microporous materials. In general, argon at 87.3 K is always a better molecular probe than nitrogen, since it does not give rise to specific interactions with a variety of surface functional groups, which can lead to enhanced adsorption/specific interactions caused by quadrupole moment characteristic to non-symmetric molecules. In addition, argon at 87.3 K fills micropores of dimensions 0.5-1 nm at higher relative pressures compared to nitrogen at 77.4 K, and due to faster diffusion, the equilibration times are shorter. As such, it is possible to test micropores as small as 0.5 nm with argon within the reliable range of relative pressures that is limited in modern automated instruments by $\sim 10^{-7}$. The advantages of using argon are very pronounced for zeolites [62] and metal-organic frameworks [63], see Sections 5.3.2 and 5.3.3.

When using either argon or nitrogen, pore filling of ultramicropores still occurs at very low pressures. Associated with the low pressures is the well-known problem of restricted diffusion, which prevents probe molecules from entering the narrowest micropores pores of width <0.45 nm. The use of CO_2 as the adsorbate at ambient temperatures has a greater advantage for testing ultramicropores. Despite the fact that the dimensions of N_2 , Ar, and CO_2 molecules are similar, CO_2 molecules are able to easily access the ultramicropores at ambient temperature. Because of these experimental advantages, CO_2 adsorption has become a standard tool for the assessment of microporous carbons [64]. Due to the complex interaction of CO_2 with SiO_2 , the carbon dioxide is not used for characterization of silica and other oxides.

Applications of DFT Kernels for carbonaceous and organic materials

4.1. Microporous carbons: NLDFT model of slit-shaped pores

Historically, the first DFT kernels were developed for carbon slit pores [8, 10]. Ravikovitch et al. [15] designed the consistent equilibrium NLDFT kernels for nitrogen, argon, carbon dioxide isotherms, which are applicable for disordered micro-mesoporous carbons of various origin, including activated carbons, and carbon fibers, charcoal, and carbon black. These kernels are composed of equilibrium isotherms and they should be applied to reversible isotherms and desorption branches of hysteretic isotherms. The exception is the case of hysteretic isotherms with a sharp desorption step at relative pressure $P/P_0 \sim 0.4-0.5$, which may indicate the cavitation mechanism of desorption. In this case the adsorption branch should be used and the adsorption kernels are recommended. This is a general recommendation applicable to all systems with the sharp desorption branch in the region of cavitation, which is discussed in details in section 5.6.

4.1.1. Activated carbons

Activated carbons (AC) are some of the first materials to be characterized by NLDFT. It is a fair assumption to model pores found in activated carbons and activated carbon fibers as graphitic slabs separated by slit like pores.

Due to the abundant micropore volume and high internal surface area, activated carbons have found wide usage in a range of applications which include separation, gas purification, removal of pollutants and odors, gas storage, catalysis and catalyst supports. Current routes to synthesize activated carbons is typically achieved through the use of natural materials as a precursor and include coal petroleum, vegetable and polymeric precursors [65]. The nature of which, along with the activation procedure and means of carbonization, affect the pore structure and surface chemistry, which determines the adsorption capabilities and thus applicability of the adsorbents. However, there is an ever growing need to find new and cheaper precursors in the form of industrial and agricultural residues which can exhibit great valorization potential.

The following studies applied the NLDFT method as a tool for AC characterization. Nabais et al. synthesized activated carbons by using vine shoot as a biomass precursor as seen in Figure 7[66]. They evaluated that a greater amount of porosity was achieved at higher activation temperatures when the burn-off is kept constant. Rios et al. prepared samples of activated carbon using coconut shells as a precursor [67]. They were able to show that their synthesis procedure produced pores within the range of 8-15 Å regardless of the activation protocol chosen. Meanwhile Zhang et al. increased the microporosity of already made AC by depositing fine carbon particles onto the AC from pyrolyzing methanol and by heating the AC in an inert atmosphere [68]. Although neither approach changed the trend of the PSD, it did significantly increase the pores within the range of 4-20 Å. Almarri et al. evaluated the performance of 7 commercial AC for the removal of nitrogen compounds [69]. By invoking the NLDFT method Rios et al. were capable of identifying the optimal AC structures for the removal of propanethiol

from the liquid phase[70]. Burrell et al. [71] used NLDFT as one of the tools to compare the structure of different activated carbon derived from corncob for the hydrogen storage. Their samples were shown to have storage capacities of up to 100 g H₂/kg (90 bar, 83 K) and 20 g H₂/kg (90 bar, 303K)

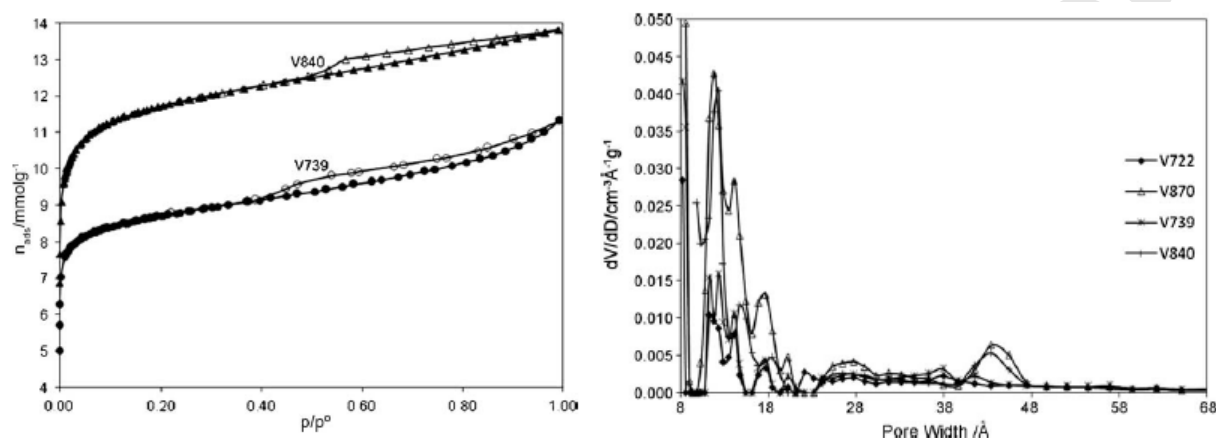


Figure 7: (a) Nitrogen adsorption isotherms at 77 K obtained for activated carbons derived from vine shoot designated as V739 and V840. (b) Pore size distribution obtained by NLDFT for samples designated as V722, V870, V739 and V860. Example of the labeling scheme is V840, where V stands for vine, 8 stands for an activation temperature of 800 °C, and 60 implies the percentage that is burned off. (Adapted from ref [66]) Note that the peaks of PSDs around 4 nm are artificial. They result from the cavitation step on the desorption isotherms at $P/P_0 \sim 0.42\text{--}0.5$. This artifact is discussed in Section 5.7.

4.1.2. Activated carbon fibers

Activated carbon fibers (ACF) exhibit a type I isotherm and possess a very high adsorption capacity with BET surface areas up to 3000 m²/g [72]. This results in rapid adsorption and desorption rates with over 90% of the total surface area belonging to micropores of 2 nm or less [73]. And like their granular counterparts, ACF are finding a foot hole in a broad range of applications including gas and liquid phase adsorption, carbon molecular sieves, catalysis, gas storage, and supercapacitors [73]. The advantages of ACF are multi-fold and are primarily due to its ability to be drawn into lightweight fibers or cloth with a fiber diameter ranging between 10 and 40 microns. Their fibrous design is advantageous in applications where settling and

channeling becomes an issue [74] or when higher packing density is required [75]. In addition, ACF tend to possess a narrow pore distribution, thus eliminating mass transfer limitations. Nevertheless, the implementation of ACF are inhibited by the relatively high unit cost [76-78] and thus requires a detailed elucidation of the synthesis conditions that can comply to different applications [79].

The factors that greatly affect the ACF properties (precursor source, temperature, time, gas flow activating agents and the use of catalysts) are the ones that most influence the pore structure. ACF prepared by a physical activation process will be dependent on a controlled gasification process at temperature ranging from 800 to 1000° C. In their activation procedure Shiratori et al. [79] applied the NLDFT method and showed that a greater degree of activation led to a widening of the pore size distribution from 2.8 to 7.0 nm. They contribute this broadening to a decrease in the number of microdomains. This phenomena was coupled with an increase in the peak pore size (from 0.44 nm to 1.86). The adsorption data and subsequential pore size analysis was confirmed by ^{129}Xe NMR [79]. The chemical activation process on the other hand involves the mixing of a carbon precursor with a chemical activating agent typically KOH, NaOH, H_3PO_4 or ZnCl_2 [73].

Additional species can be added in order to steer the activation process, the effect of which can be identified by using NLDFT. Mushrif et al. studied the effect of adding an organometallic salt to the fiber precursor [80]. They synthesized ACF prepared from isotropic petroleum pitch, with and without palladium acetylacetonate. They conclude that the presence of the palladium led to an increase in micropores that widened at very high activation values, a trend not observed with the BJH method. In contrast, Wu et al. concluded that activation at high levels of burn off did contribute to the overall increase of the BET surface area, although it did not contribute much to the increase of micropores which they defined being less than 7 Å [81].

Donnaperna et al. used the NLDFT CO₂ kernel [15] to study the extent of adsorption of the two dyes Remazol Black B and Acidol Red on ACF [72]. Since ACF possesses a microporosity defined almost entirely by ultramicropores (< 1 nm) the uptake in adsorption of the dyes were defined by interparticle diffusion.

Figure 8 gives differential and cumulative pore volume distributions of CFCMS carbon fiber calculated from N₂ and Ar adsorption isotherms at 77 K using NLDFT model, and from sub atmospheric CO₂ adsorption isotherm at 273 K using NLDFT and three-center GCMC models [15]. Since the considered sample possessed ultra-microporosity, the PSD obtained using CO₂ provides more complete information on the structure (see section 3.3).

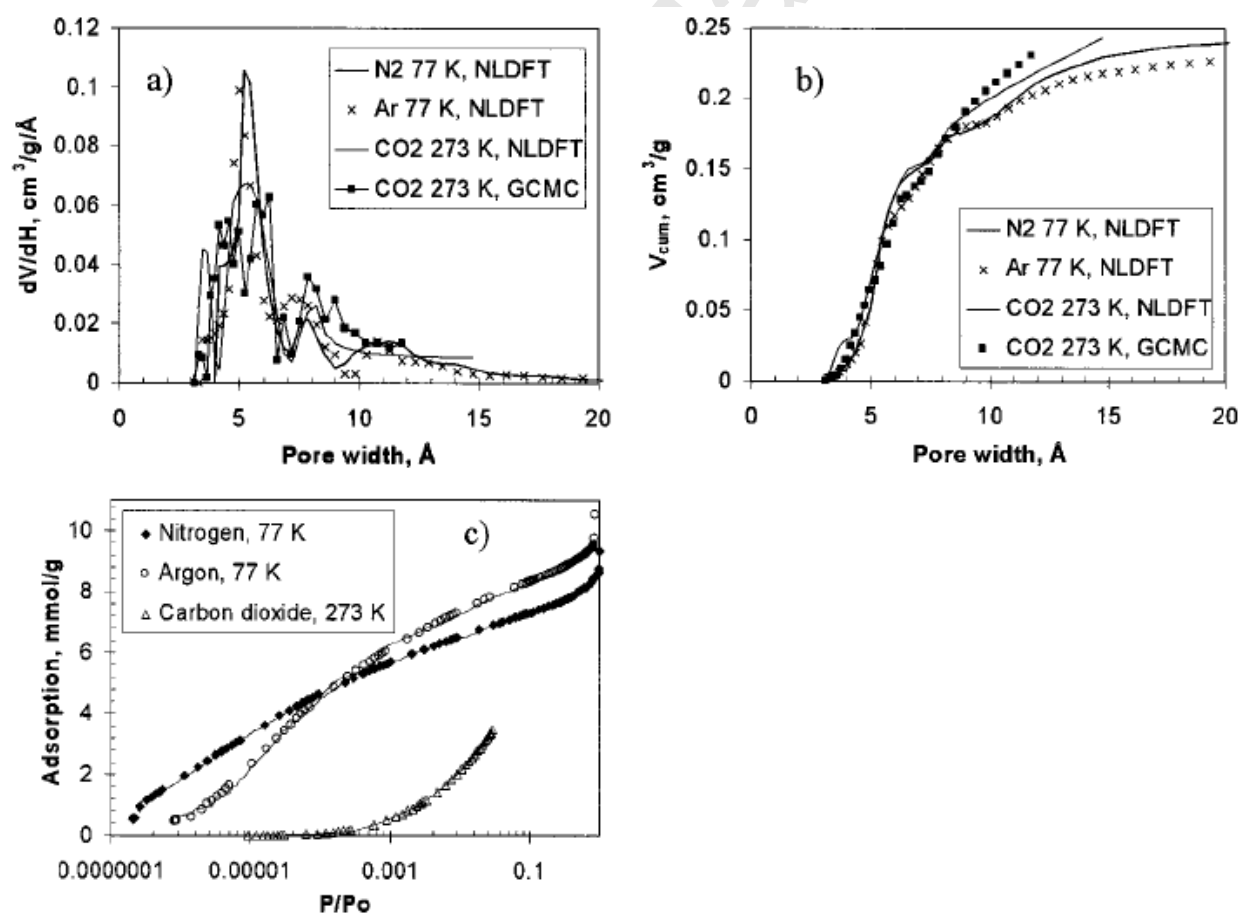


Figure 8: (a) Differential and (b) cumulative pore volume distributions of carbon fiber calculated from N₂ and Ar adsorption isotherms at 77 K using NLDFT model, and from sub atmospheric CO₂ adsorption isotherm at 273 K using NLDFT and three-center GCMC models. (c) N₂ and Ar

adsorption isotherms at 77 K, and CO₂ isotherm at 273 K on carbon fiber. Experimental isotherms (points). Theoretical fits (lines) (Adapted from ref [15]).

4.1.3. Carbon black, deposits and charcoal

Carbon black is the result of an incomplete combustion of fossil fuel derived from petroleum in the fluid catalytic cracking process and includes coal, tar and some biomass materials. Carbon black possess a surface area up to $\sim 100\text{m}^2/\text{g}$ [82] and its porosity can be effectively characterized by the NLDFT method. Fifteen commercial grades of carbon black were utilized to study its capability as a carbon support in the preparation of Fe/N/C electrocatalysts in polymer electrolyte membrane (PEM) fuel cells [83]. It is well known that the presence of micropores in carbon black serve as catalytic sites that are essential to catalytic activity[84] and therefore an accurate depiction of the pore structure is required. The authors reaffirm this by studying the development of the pore structure as a function of pyrolysis and with the further development of microporosity ($< 22\text{ \AA}$) leading to an increase in catalytic activity. These results were concluded with the NLDFT N₂ 77 K kernel and correlated with XRD results. Another class of carbon black, commonly known as charcoal, typically has a heterogeneous micropore structure which includes pores less than 4 \AA . Braida et al. investigated the sorption hysteresis of benzene in charcoal particles and proposed the occurrence of irreversible pore deformation [85]. NLDFT analysis of pore-size distribution from both N₂ and Ar at 77 K allowed them to conclude that swelling occurs within the charcoal by the solute which in turn opens up previously inaccessible pores. These results are shown in Figure 9.

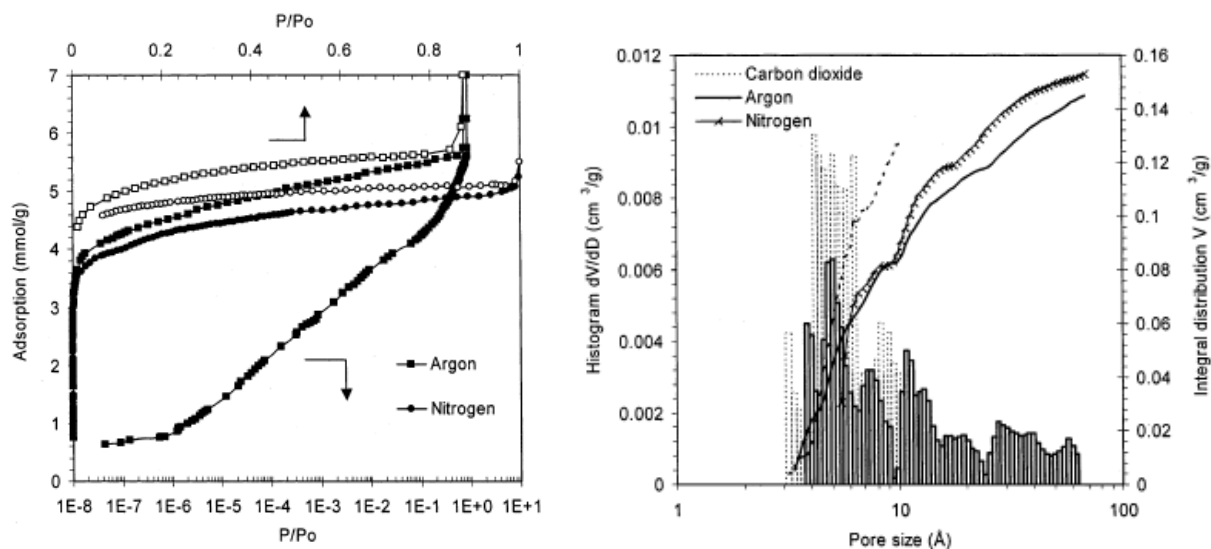


Figure 9: (Left) Nitrogen (circles) and argon (squares) isotherms at 77.4 K on charcoal outgassed at 573 K. Adsorption and desorption points are depicted by closed and open symbols respectively. Both linear and logarithmic pressure scales are shown for argon. The isotherm for N_2 contains 150 points collected over 50 h, whereas the Ar isotherm was performed over a combination of 60 then 70 h with 3 and 132 data points respectively. (Right) Pore size distributions calculated from the N_2 , Ar and CO_2 adsorption branch of the isotherm. The NLDFT method was applied for Ar and N_2 whereas Monte Carlo models were applied for CO_2 [85].

An interesting field where the structure of porous carbons play an important role is in the area of the nuclear reactors. Richou et al. [86] studied the carbon deposits collected on the neutralizers of a Tore Supra tokamak by N_2 and CO_2 at 77 K and 303 K respectively. Using NLDFT analysis they found that the adsorption capacity reversibly increases up to 40% for outgassed samples. The authors surmised that the latter is most likely the consequence of re-opening of ultramicropores at high temperatures. It should be noted that porosity is the most critical aspect in modeling and estimating the degree of hydrogen diffusion into tokamak walls [87].

4.1.4. Carbon nanotubes

With a high aspect ratio, tensile strength, electrical and thermal conductivity, carbon nanotubes (CNT) represents a class of nanomaterials that is being employed extensively in a

wide array of fields. In particular, there has been growing interest in the adsorption capabilities of CNT for various applications[88, 89] where the aid of NLDFT in order to characterize the porosity can be of use. CNT typically display a type II isotherm [90, 91] with no hysteresis due to the smooth inner walls of the CNT. While individual CNT have apparently a cylindrical shape, CNT materials are composed of CNT bundles and the porosity is mainly associated with the interstitial spaces within and between the bundles, which do not possess cylindrical geometry. As such, the NLDFT kernel for slit pores [15] is commonly used for characterization of CNT materials, and the PSD results can be used for comparative estimates rather than as absolute quantitative data.

The NLDFT method was employed to analyze the increase of CNT bundle porosity in the process of etching with acid or ozone [92, 93]. For example, Byl et al. [92, 93] utilized ozone as an oxidating agent in order to expose more pore volume. They concluded that extensive O_3 induced etching resulted in pore wall destruction of the nanotubes with diameters less than 20 Å. Their results are displayed in Figure 10. The Kaneko group studied the effect of oxidation after treatment with HCl [93]. They showed an increase from 524 m^2/g for pristine HiPco nanotubes to 861 m^2/g for the HCl treated and air oxidized nanotubes.

Porosity is a significant factor in the field of hydrogen storage, where thus far the optimal storage conditions are still ill-defined. Anson et al. deduced from NLDFT pore size distributions done at both CO_2 at 273 K and N_2 at 77 K[15], that CNT pores with a maximum width between 0.5 and 0.7 nm was optimal for hydrogen to be adsorbed at room temperature[94]. Byl et al. investigated the porosity as a function of already adsorbed n-nonane to determine the existence of blocking effects within the CNT [95]. In relation to polymer composites fabricated with CNT, Neimark et al. showed that single-wall CNT fibers produced by a particle-coagulation spinning process possessed a well-developed hierarchical pore structure [96].

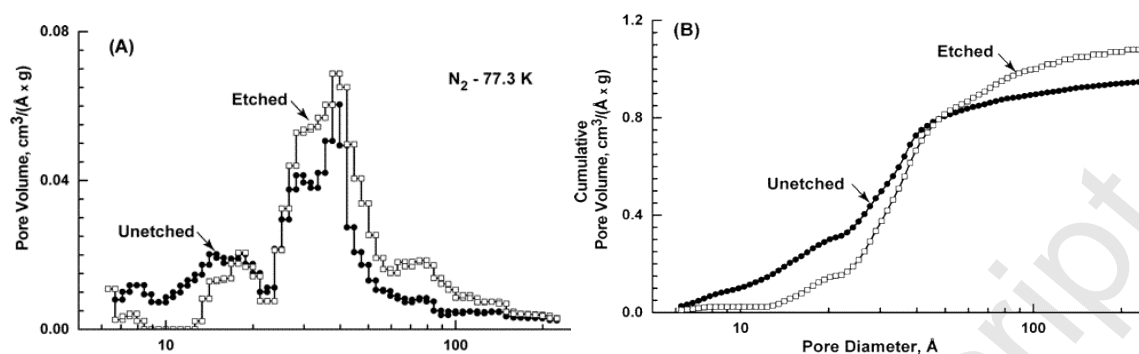


Figure 10: (a) Pore size distribution calculated using the NLDFT slit pore model for etched and unetched CNT samples; (b) Comparison of the cumulative pore volume increase versus pore size. (Adapted from ref [92])

4.1.5 Additional Applications

The NLDFT method for carbon has been applied to molecular sieves and membranes resulting in their detailed characterization, critical for applications in gas separation, chromatography and storage. Katsaros et al. produced membranes through a carbonization and subsequent activation of phenolic resins. When they applied the NLDFT method they deduced that the majority of the pore volume lies below 7.5 Å [97]. Jagiello et al. applied the NLDFT method to Ar and H₂ adsorption data, demonstrating it as an effective and sensitive tool to characterize carbon molecular sieves [98]. NLDFT was also utilized by Drozdov et al. who modified a mesoporous carbon substrate with activated carbon capable of adsorbing CO₂ and CH₄ [99].

4.2. Improvement of pore structure characterization with QSDFT model

QSDFT method significantly improves the pore size characterization of carbons. Due to the mismatch between the theoretical assumption of a smooth and homogeneous surface and the real molecularly heterogeneous surfaces of porous carbons the theoretical NLDFT adsorption isotherms exhibit multiple steps associated with layering transitions related to the formation of a

monolayer, second adsorbed layer, and so on (see Figure 6). The problem is enhanced in many porous carbon materials, which exhibit broad PSDs, where artificial layering steps inherent to the theoretical isotherms cause artificial gaps on the calculated pore size distributions [20]. Figure 11A gives the experimental adsorption isotherm of N_2 on ACF along with the fitting from NLDFT and QSDFT methods. Figure 11B gives the PSDs obtain using these methods. The gap in the NLDFT PSD corresponds precisely to the pressure at which the first layer of adsorbed fluid forms.

Further examples of QSDFT kernel applications include activated carbons derived from pecan shells [100], biochars [101] and activated chars derived from poultry manure [102, 103]. Polymer systems have included carbon aerogels [104] and various polymer networks [105]. Commercial versions of granular activated carbons commonly used in water treatment applications were studied in accordance with water sorption measurements [106]. In the case of activated carbon produced by KOH, Romanos et al. showed the capability of tailoring the pore size and distribution by precise control of the carbon consumption and amount of potassium intercalated between the graphitic layers [107]. Likewise, Hu et al. examined the effect of activation temperature and the KOH treatment ratio on the outcomes of the pore size distribution and mean sizes [108]. Yang et al. used the QSDFT model to study CO_2 adsorption on coal under geological conditions [109]. Nanostructured carbons templated with zeolite NaY and two commercial silica gels (SG60, Fluka and ZK, POCh) were investigated with the QSDFT method to yield a mean pore size of 1.1 nm in the micropore range [110]. Another material whose microporosity plays a critical role in its applications is carbon derived carbide (CDC). In the work of Yeon et al. the authors transformed TiC by a chlorination technique to that of CDC [111]. The resultant material possessed a significant amount of carbon microporosity characterized by the QSDFT method [20]. The authors show that this material has little

macroporosity and demonstrates a significantly enhanced gas storage capacity compared to their powder counterparts. Another paper by the same group shows that the method accurately portrays pores comprised of a slit geometry at higher chlorination temperatures where the pores becomes more elongated [112]. In the field of supercapacitors the interplay between the porosity and the underlying carbon substrate contributes to the overall capacitance. The Ruoff group demonstrated an activation procedure to produced mesoporous single layer graphene comprised primarily of sp^2 carbon with low overall oxygen content [113]. Their material, which possesses a surface area of $3100 \text{ m}^2/\text{g}$ and a high electrical conductivity, was characterized by both NLDFT[15] and QSDFT[20] assuming a hybrid slit and cylindrical model. Jaramillo et al. employed QSDFT analysis to determine textural properties of various activated carbons used as electrodes for supercapacitors [114]. The QSDFT method has also been shown to be suitable for the characterization of flexible supercapacitors fabricated with activated carbon impregnated into woven cotton and polyester fabrics [115].

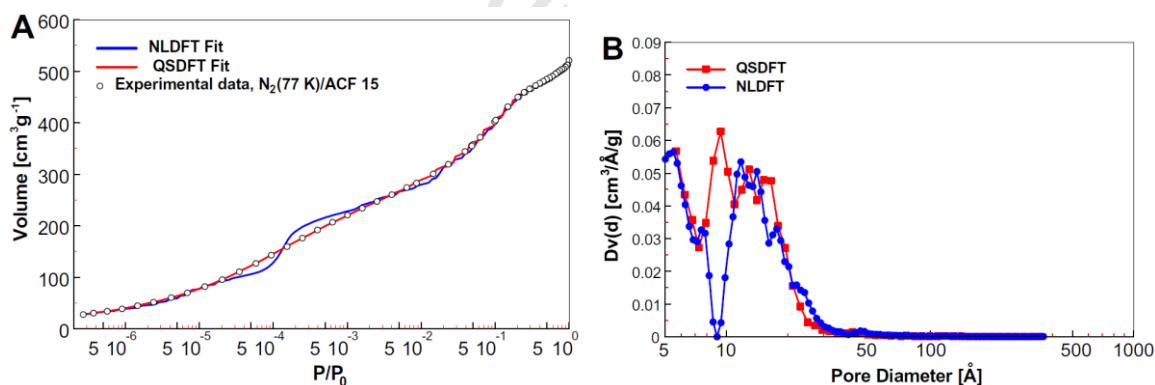


Figure 11: Comparison of the QSDFT and NLDFT methods for nitrogen adsorption for activated carbons. (a) Experimental isotherms with the NLDFT and QSDFT theoretical isotherms on a semi-logarithmic scale. (b) Differential pore size distributions obtained from the NLDFT and QSDFT methods. (Adapted from ref [20])

4.3. Designer mesoporous carbons: hybrid QSDFT kernels

For ordered/templated carbons where the morphology is a system of cylindrical rods or cylindrical channels (CMK-1, CMK-3, CMK-5, MWCMK-3, FDU-14, FDU-15, FDU-16) the

cylindrical kernel is recommended [50]. If such materials have a high degree of activation, leading to significant microporosity, then the hybrid slit-cylindrical kernel is more suitable. Equilibrium NLDFT or QSDFT kernels can be recommended for pore size analysis from either the reversible experimental isotherm, or from the desorption branch of the hysteric isotherm of type H1. Adsorption QSDFT kernels are recommended for treating the adsorption branch of the hysteric isotherm of H2 type. It should be noted that the criterion for choosing a particular DFT kernel is the fitting of the PSD to the experimental isotherm. Choosing the wrong pore geometry will lead to poor fitting results.

4.3.1. Structures with mesopore channels: cylindrical pore model

One class of carbons whose mesoporosity consists of a network of aligned cylindrical rods connected by crossbars is known as CMK-3 [116]. These materials are synthesized by the inverse replication of mesoporous silica SBA-15, and therefore they possess a 2-D hexagonal symmetry (p6mm). Endowed with a number of unique properties, these materials have attracted much attention for energy and biological applications. As such Zhou et al. showed that CMK-3, possessing a high negative redox potential and high electrical double-layer capacitance, can serve as a material for the negative electrode for rechargeable lithium batteries [117]. Vinu et al. [118] showed that CMK-3 is an excellent adsorbent for biomaterials, because it is thermally and mechanically stable, and, unlike silica, it is stable in the presence of water. Since CMK-3 is microporous, as opposed to many other carbon materials, it is capable of adsorbing large molecules, like enzymes and vitamins. Despite the addition of the crossbar pores which possess a complex shape, the cylindrical model is typically assumed for characterization [119].

CMK-3 usually shows the type IV adsorption isotherms with a pronounced hysteresis loop. If the hysteresis is of H1 type, the PSD can be obtained both from adsorption and desorption branches using adsorption and equilibrium kernels correspondingly; the resulting PSD

gives good agreement [50]. However, if the hysteresis has features of H2, evidence of the pore-blocking effects upon desorption, only the adsorption branch of an isotherm should be used for analysis. This is the case for the example shown in Figure 12. For this sample the pore size distribution obtained from the desorption branch of the isotherm (using the equilibrium kernel) noticeably deviates from that of the adsorption branch and gives an incorrect pore size distribution because this kernel assumes that desorption occurs via equilibrium evaporation from the pore, which is not the case for this sample. The fit for the adsorption kernel is shown in Figure 12a and the corresponding pore size distribution is shown in Figure 12.

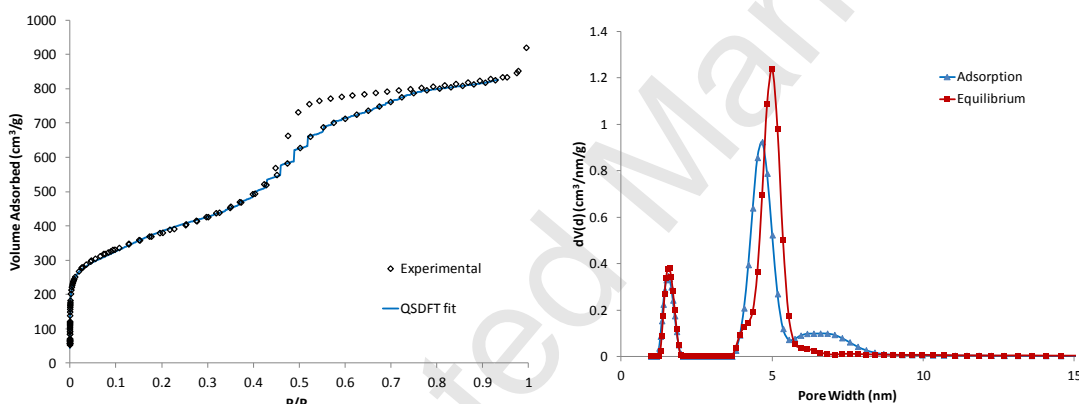


Fig 12: Isotherm (left) and corresponding pore size distribution (right) for CMK-3 materials of varying pore sizes. (Adapted from ref [50])

4.3.2. Structures with cage-like mesopores: spherical pore mode

For materials in which the mesopore system is comprised of large cage-like pores connected by smaller mesopores and/or embedded in microporous matrix, such as carbons prepared from 3D colloidal templates (3DOm), the cylindrical-spherical adsorption kernel is recommended [61]. Use of cylindrical or slit model for micropores and mesopores, smaller than ca. 5 nm is reasonable, since such pores (if present) are not affected by templating.

Materials with cage-like mesopores typically have H2 hysteresis type due to the pore-blocking effects (see section 4.3.2.). However, both N₂ [120] and Ar [61] adsorption isotherms show H1 type of hysteresis. This is due to the unconventional mechanism of pore-blocking, specific for 3DOm carbons, where upon desorption the fluid in the cage-like pores is blocked not by channels [121] but by the openings between the pores [122]. Irrespective of the pore-blocking mechanism, the desorption branch of an isotherm for a 3DOm carbon sample is not suitable for calculating the PSD.

In general there are two approaches to synthesizing 3DOm's, both of which includes a templating procedure. These two routes include the filling of either a mesoporous matrix or the filling of voids, typically between silica spheres in the latter, with a carbon precursor that is polymerized then carbonized [123]. The final step involves the removal of the original templating matrix commonly by etching. These two approaches have become commonplace especially with the abundance of mesoporous silicas, where there is a large variety, owing to their high structural order, large diversity in structure, controlled tunability of the wall thickness [124], and cost efficiency [125, 126]. With such control and variability, it is imperative that the pore properties are well correlated with changes in the synthesis conditions.

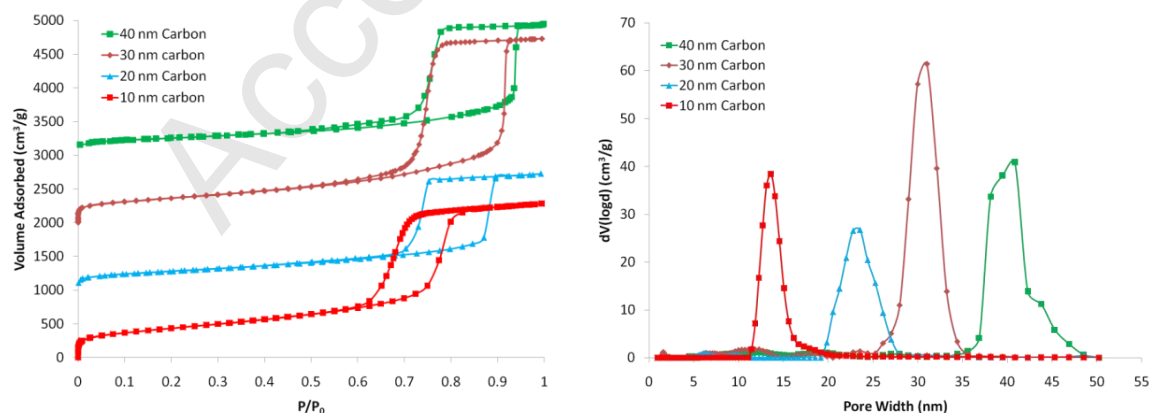


Fig 13: Isotherm (left) and corresponding pore size distribution (right) for 3DOm materials of varying pore sizes.

Wilke et al. applied the QSDFT model for spherical carbons in their replication of the commercially available LudoxTM-50 glass yielding poly(divinyl benzene)-TM50 (PDVB-TM50) as seen in Figure 14[127]. Pore size analysis obtained from the adsorption branch shows three pore sizes. Within the micropore range, they attributed the presence of 5% of the pore volume due to a polymerization induced phase separation. They support this argument with SAXS data. This pore fraction was followed by mesopores constituting a 10% pore volume fraction likely due to partially collapsed larger pores or voids. Lastly the third and largest fraction, of which 85% of the total porosity is represented, contains diameters of about 28 nm corresponding to the original silica particles. Like the 3DOm carbons explained before, this example exhibits a Type H1 hysteresis that originates from pore-blocking effects. This is substantiated by the fact that the desorption branch occurs at a relative pressure of about ~0.6.

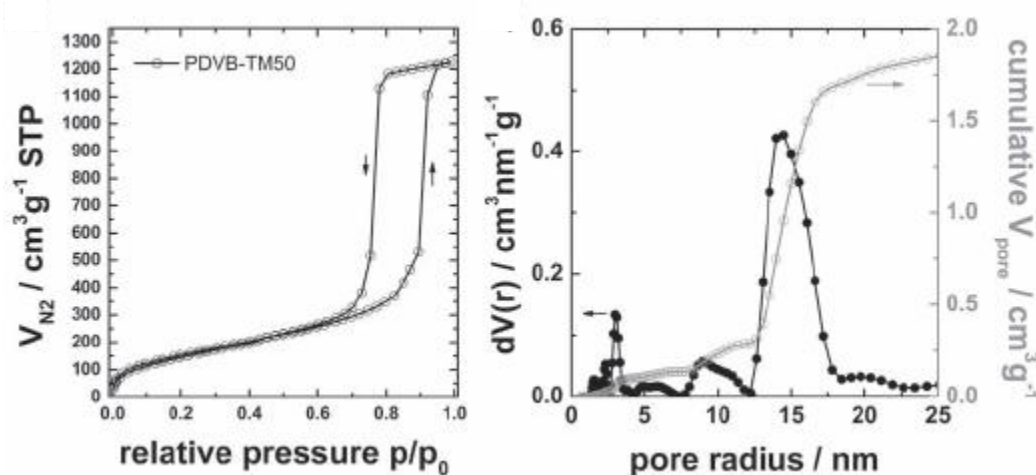


Figure 14: Hard templating from silica spheres to produce mesoporous carbons. (Right) N_2 at 77.3 K adsorption/desorption isotherm of PDVB-TM50; (Left) pore size distribution (black) and cumulative pore volume (grey) as obtained by QSDFT analysis (carbon, spherical pores, adsorption branch) from the adsorption isotherm. (Adapted from ref [127])

5. Applications of DFT Kernels for silica and other inorganic materials

For silica materials with assumed channel-like pores resulting in a H1 type hysteresis on the adsorption-desorption isotherm (MCM-41, SBA-15), a cylindrical kernel is recommended.

Pore size distributions can be obtained from the adsorption branch by means of the adsorption kernel and from the desorption branch using the equilibrium kernel. The agreement between the two PSDs obtained testifies to the absence of any pore blocking or cavitation effects.

For silica with cage-like pores connected by channels (i.e. SBA-16) spherical-cylindrical adsorption kernel should be used. Such systems tend to reveal a wide H2 hysteresis loop with the desorption branch, which is governed by cavitation [128]. As such, only the adsorption branch can be employed for PSD calculations.

5.1. MCM-41 as the reference materials for pore structure characterization

The appearance of MCM-41 on the scientific landscape provided investigators for the first time a well ordered mesoporous material for which they could test their theoretical models for capillary condensation in pores in order to obtain accurate pore size distributions. Prior to the introduction of MCM-41, meso and microporous substances consisted of disordered entities where the correlation between different characterization techniques were poorly understood. However with the development of MCM-41, NLDFT methods were developed and verified against other experimental techniques such as XRD and TEM [14, 24]. The range of samples that were first tested were within 3.2 to 4.5 nm, with an example given in Figures 15 and 16. XRD results confirmed regular hexagonal arrays of pores that were correlated to NDLFT by accounting for the pore wall thickness and thereby the pore sizes themselves (Figure 17). This was validated against independent means to calculate the pore wall thickness by XRD [129-132] as well as TEM [130, 132]. Furthermore, both Ar and N₂ adsorbates were tested for MCM-41 accounting for the consistent nature of the NLDFT approach.

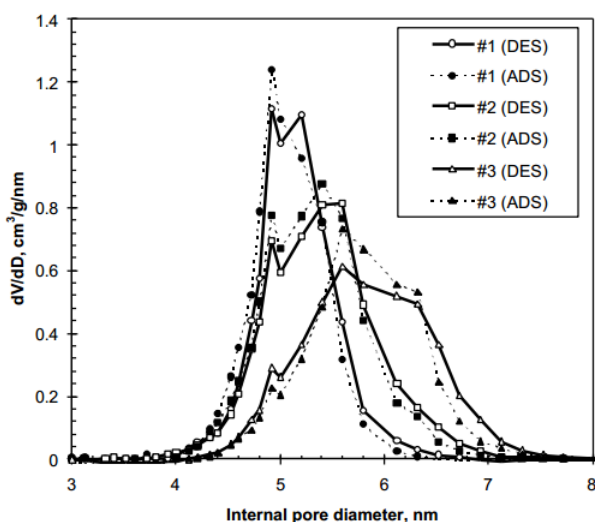


Figure 15. The pore size distributions of three MCM-41 samples calculated from adsorption (dotted lines) and desorption (solid lines) branches of nitrogen isotherms by the NLDFT method. (Adapted from ref [133])

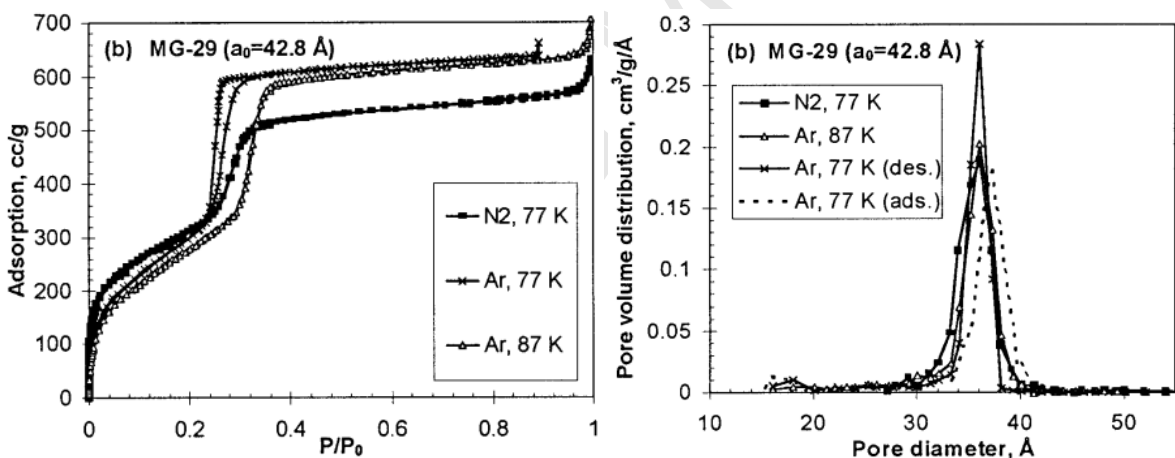


Figure 16: (Left) Isotherms for MCM-41 at N₂ (77 K) and Ar at both 77 K and 87 K. (Right) Corresponding pore size distributions calculated using the NLDFT method. (Adapted from Ref [14])

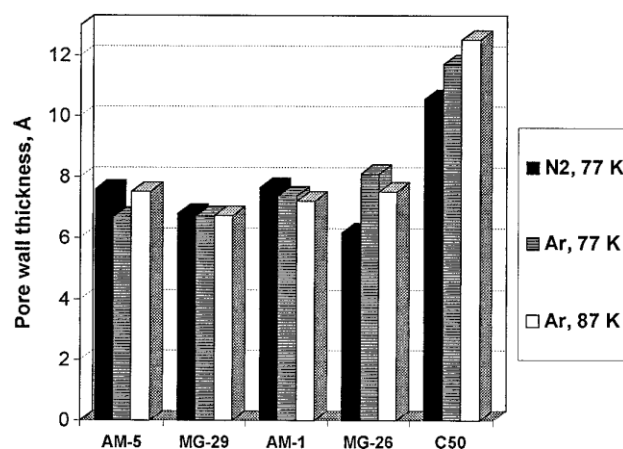


Figure 17. Pore wall thickness of MCM-41 samples calculated by the NLDFT method from different isotherms. (Adapted from Ref [14])

5.2. Gyroidal pore networks

The application of NLDFT is not limited to pore structures that are defined by an array of pores. For the silica structure MCM-48, where the structure possesses a gyroidal geometry, the pores are defined as a bicontinuous structure with two non-intersecting subvolumes [129, 134, 135]. The NLDFT based approach was found to be a rigorous method for the calculation of the pore structure, and distributions calculated from nitrogen and argon isotherms were in good agreement. The results of NLDFT were combined with XRD in order to interpret the pore wall thickness.

Like MCM-48, KIT-6 is defined by two intertwining mesopores, forming a gyroidal structure with a Ia3d symmetry. The interconnected pores can give rise to a hysteresis relating to pore blocking effects. Kleitz et al investigated the hysteresis mechanism within KIT-6 materials aged at different temperatures as seen in Figure 18 using both NLDFT for N₂ at 77 K and Ar at 87 K [136]. They observed a narrower hysteresis loop for KIT-6 when compared to SBA-15 of the same pore size, thus indicating a characteristic feature of the hysteresis when going from a pseudo-one-dimensional material such as SBA-15 to that of a 3-D structure such as KIT-6. The authors validate their NLDFT finding with the use of TEM and XRD modeling. In a related paper Guo et al. probed phenylene-bridged periodic mesoporous organosilicas produced via

synthesis materials containing Pluronic P123 triblock copolymer, butanol and water [137]. This led to a bicontinuous cubic KIT-6 structure produced in high yields and purity. In this case 1,4-bis(triethoxysilyl)benzene was used as the organosilica source where the ageing temperature allowed for precise control over the pore characteristics such as mesopore size, volume and specific surface area. The authors suggested that the resultant 3-D structure would be beneficial for applications of host-guest chemistry, where concerns of pore blocking may arise. Post synthesis grafting techniques [138-143] for mesoporous silicas have gained traction in recent years for the development and application of highly selective sorbents, solid catalysts or drug delivery systems[144-148]. One such approach is the pore surface-confined polymerization technique developed by Choi et al.[149]. In a two-step process Guillet-Nicolas et al. modified the walls of KIT-6 with the polymer polychloromethylstyrene (PCMS) followed by the attachment of amine groups to the polymer[150].

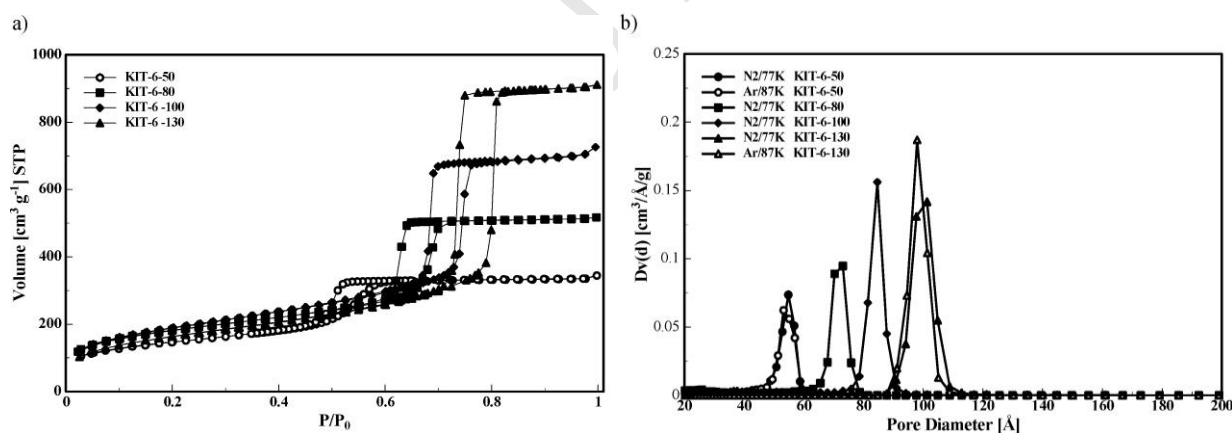


Figure 18: (a) Nitrogen isotherms (at 77.4 K) in KIT-6 samples aged at temperatures varying from 50 to 130 °C. The desorption branch is used for the NLDFT pore size distributions for nitrogen at 77.4 K and argon at 87.3 K respectively. (b) Selected KIT-6 samples aged at different temperatures are displayed. The NLDFT pore sizes (equilibrium) are 5.5, 7.3, 8.4, and 10.1 nm, for 50, 80, 100, and 130 °C, respectively. (Adapted from ref [136])

5.3. Accounting for microporosity

Two critical problems can arise when properly taking into account the surface roughness and microporosity inherent to many polymer-templated silicas such as SBA-15, as well as many

other organosilica materials. Past efforts to correctly account for the microporosity involved the standard comparison or t-plot methods [151]. However, the volume of micropores obtained by this method cannot reliably decipher between the two mechanisms of micropore filling and multilayer adsorption on a rough surface of a low-density “corona” [48]. As will be shown in the following section, using SBA-15 as a case example, the comparison method greatly underestimates the total amount of micropores residing in the intrawall pores and the NLDFT method is revealed to be an exceedingly better approach.

5.3.1 SBA-15 as the case study system

In 1994 a seminal class of silica compounds were created from the Stucky group in Santa Barbara denoted as SBA-n [152-154]. The most prevalent of these materials is SBA-15. Templated from triblock copolymers, this material possesses cylindrical mesoporous channels much like MCM-41. However SBA-15 differs from MCM-41 in the sense that due to the templating procedure it contains an appreciable amount of intrawall pores, amounting up to 30% of the total porosity. Previous methods to accurately describe the microporosity, such as the comparison plot, erroneously assumed that the micropore and mesopore range did not overlap. Doing so results in a significantly lower micropore volume. This was resolved with the application of the NLDFT method [26] which showed that pore diameters were in accord with the pore diameters obtained from quantitative modeling of XRD patterns [155]. The cumulative pore size distribution curves are displayed in Figure 19 where a prominent step corresponds to the primary mesoporous channel between 6-7 nm. In addition a tail in the curve appears that represents the intrawall pores. It should be noted that calculating the micropore distribution is impeded by the typically smooth nature of the isotherm at low pressures [26].

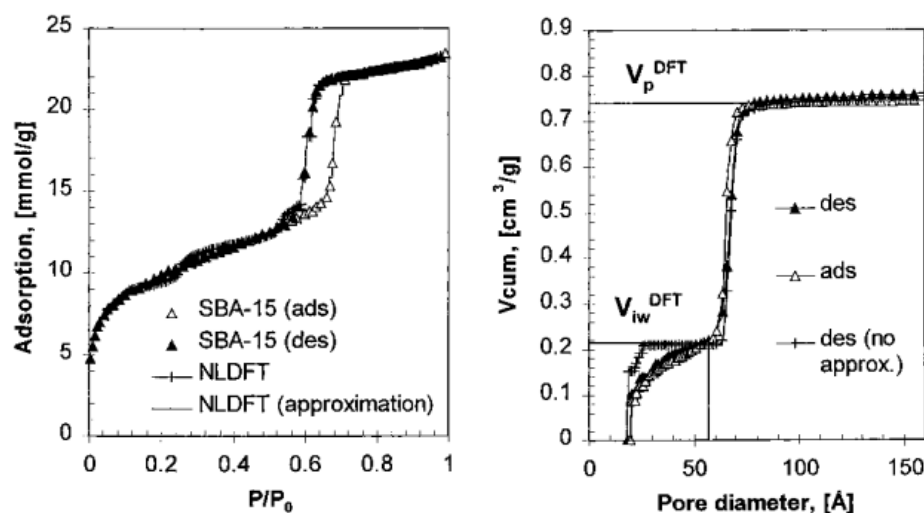


Figure 19: (Left) Nitrogen isotherms for SBA-15 material (triangles) with the fitted NLDFT isotherms obtained without approximation (crosses) and with approximation for the multilayer adsorption (lines). (Right) Cumulative pore volume distributions calculated from adsorption (open triangles) and desorption (closed triangles) branches. NLDFT pore volume distribution obtained from the desorption branch without approximation for the multilayer adsorption (crosses). V_p DFT and V_{iw} DFT are the total and intrawall pore volumes, respectively. (Adapted from ref [26])

A number of groups have chosen the NLDFT kernel for validation of their synthesis procedure of SBA-15. Bao et al. used the nonionic surfactant P123 as a template under acidic conditions to produce ethylene-bridged SBA-15[156]. They demonstrated that as the SiO₂/P123 ratio is increased so does the microporosity. As a result, the pore structure slowly transforms from open channels to a cage like structure. Hsu et al. synthesized SBA-15 using the carboxylate-terminated triblock copolymer Pluronic P123[157]. They concluded that the use of a carboxyl terminated polymer leads to a larger pore diameter and thicker walls compared to a polymer terminated with a hydroxyl group.

Recently Pollock et al. [158] used NLDFT together with diffraction intensity analysis of small-angle neutron scattering measurements of dry SBA-15 samples to characterize the micropore, secondary mesopore, and primary mesopore structure. Based on the agreement between the minimum pore size with the onset of the micropore size distribution, the authors

concluded that the shape of the smallest micropores is cylinder-like, which is consistent with the unraveling of the polymer template. NLDFT was also employed for studying the degradation of SBA-15 pores on hydrothermal treatment [159].

Control of the pore structure alteration is important during the development of post synthesis grafting techniques that enables enhanced catalytic behavior. Despite the introduction of species into the silica that do not share the same fluid-solid interactions of the designed kernel, this does not adversely affect the application of the NLDFT methods. Yue et al demonstrated this by synthesizing Al grafted SBA-15 (Figure 20) where the resulting materials retain the hexagonal order and physical properties of purely siliceous SBA-15 [33]. Their material displays the same hysteretic isotherm behavior typical of capillary condensation in mesopores before and after grafting. Another popular species for grafting is the use of Ti. This is owed to its better activities compared to microporous zeolites, in particular when bulky molecules are involved[160]. Berube et al. utilized a chelated titanium alkoxide precursor for the grafting of Ti to SBA-15[161]. Characterization by NLDFT method allowed them to reveal that the hydrothermal treatment and calcination temperatures greatly influence the extent of epoxidation of the grafted Ti-SBA-15 structures. With contribution from their NLDFT analysis they concluded that the best supports for epoxidation were those SBA-15 materials that were aged at elevated temperatures of 140 C°. The same group also demonstrated a one-step synthesis of Ti substituted silica SBA-15 by a co-condensation and demonstrated the influence of synthesis conditions (acid concentration, silicon concentration, hydrothermal treatment temperature, time) on the incorporation ratio of Ti and its subsequential chemical reactivity[162]. Along similar lines, Berube et al. grafted a titaniumalkoxide precursor onto the surface of a P123/SBA-15 composite by first modifying the precursor with a chelating agent, in this case acetyl acetone (acac) [163].

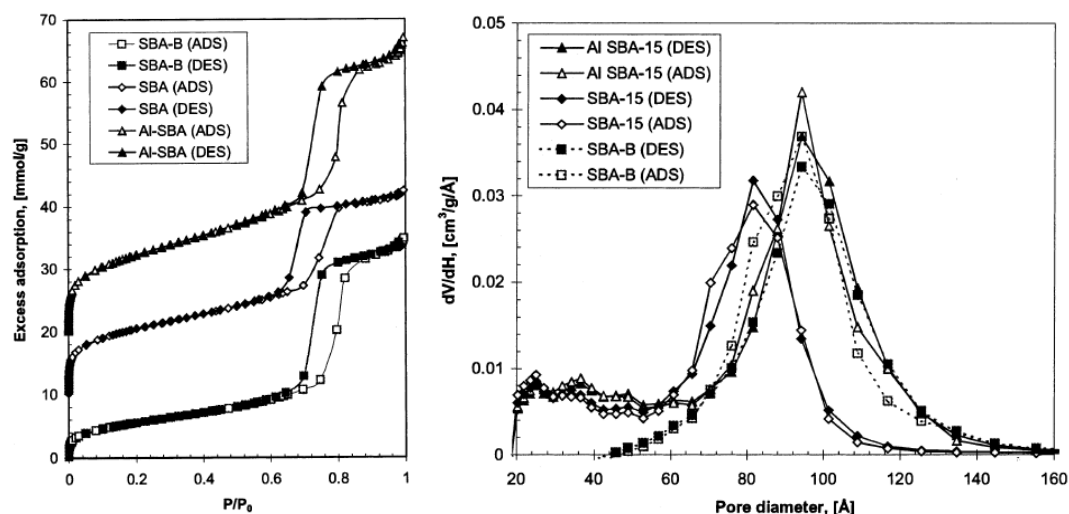
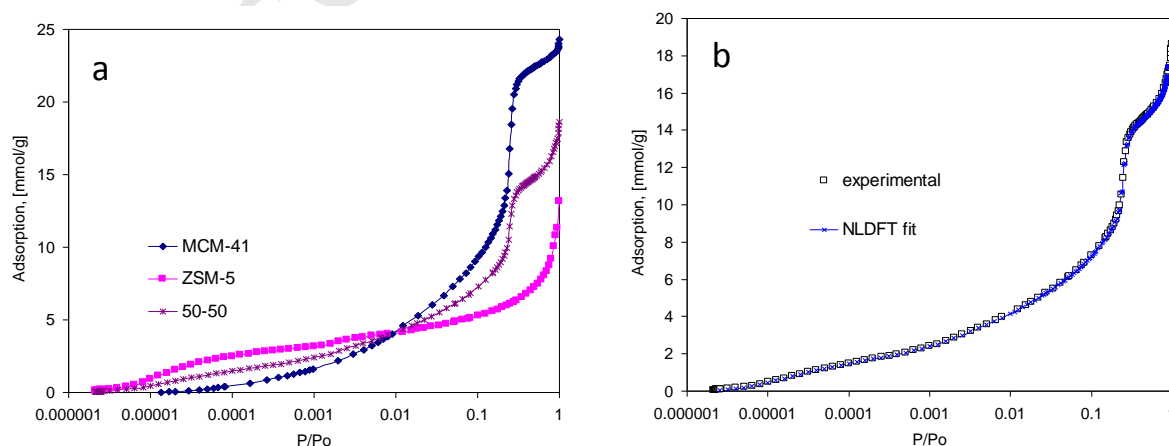


Figure 20: (Left) Nitrogen adsorption at 77.4 K on SBA-15 materials [33] displaying the corresponding Al grafted SBA-15 isotherms. The scale is shifted by 10 and 20 mmol g⁻¹. (Right) The pore size distributions of SBA-15 and Al-SBA-15 materials [33] calculated from the adsorption (open symbols) and desorption (filled symbols) branches of nitrogen isotherms by the NLDFT method. (Adapted from [164])

Additional examples other than Ti where NLDFT has been utilized to study the grafting of various species to SBA-15 have included transition metals and some polymers. Szegedi et al. grafted Co to SBA-15 for the oxidation of toluene [165]. Tsoncheva et al. administered a post solid state reduction technique with V₂O₅ verified by the oxidation of ethyl acetate [166]. It was concluded that the distribution of vanadium was dependent on the peculiarities of the pores structure. The result is a consistent pore diameter after modification, albeit the surface area and pore volume are slightly diminished. In a separate study a metalorgano complex ferrocenyl Fischer chromium carbene complex was grafted onto the surface of SBA-15 for improved catalysis [167]. Using N₂ sorption NLDFT analysis the authors elucidated a diminishing effect of the pore properties after functionalization, which in turn was used to interpret the thickness of the grafted molecule layer. Likewise, the same group grafted tungsten carbene molecules onto the walls of the silica with the surprising result that a decrease of 0.30 nm in the pore size occurs when the ethoxysilane bridging units are anchored onto the SiO₂ surface, a result that was independent of the pore size [168].

5.3.2. Zeolites

The NLDFT model for cylindrical pores that was verified on mesoporous MCM-41 materials[14] was extended by Ravikovitch and Neimark to the micropore region for application to zeolites and zeolite containing materials [62]. The NLDFT method was tested using different standard zeolites, including ZSM-5, AlPO₄-5, and VPI-5. Figure 21 presents the results of the test of the NLDFT model on high-resolution Ar adsorption isotherms at 87K (Figure 21, a) on three reference samples: mesoporous MCM-41 material, zeolite catalyst ZSM-5, and model adsorbent, containing 50% of ZSM-5 and 50% of MCM-41 [62]. NLDFT provided an excellent fit to all samples as shown in Figure 21 b for the isotherm on the combined adsorbent. Figures 21 c-e present the pore size distributions. The reported average pore diameter of ZSM-5 zeolites obtained from structural considerations is 0.51-0.55 nm that agrees well with the pore size distribution obtained from Ar adsorption by the NLDFT method. It is seen that this particular sample of ZSM-5 material contained not only micropores, but also mesopores. The reference MCM-41 material is non-microporous and its pore size obtained by independent methods is 3.2 nm, in excellent agreement with the NLDFT method. The pore size distribution of the combined adsorbent exhibits two distinct groups of pores: micropores of the same size as in ZSM-5 and mesopores of the size as in MCM-41.



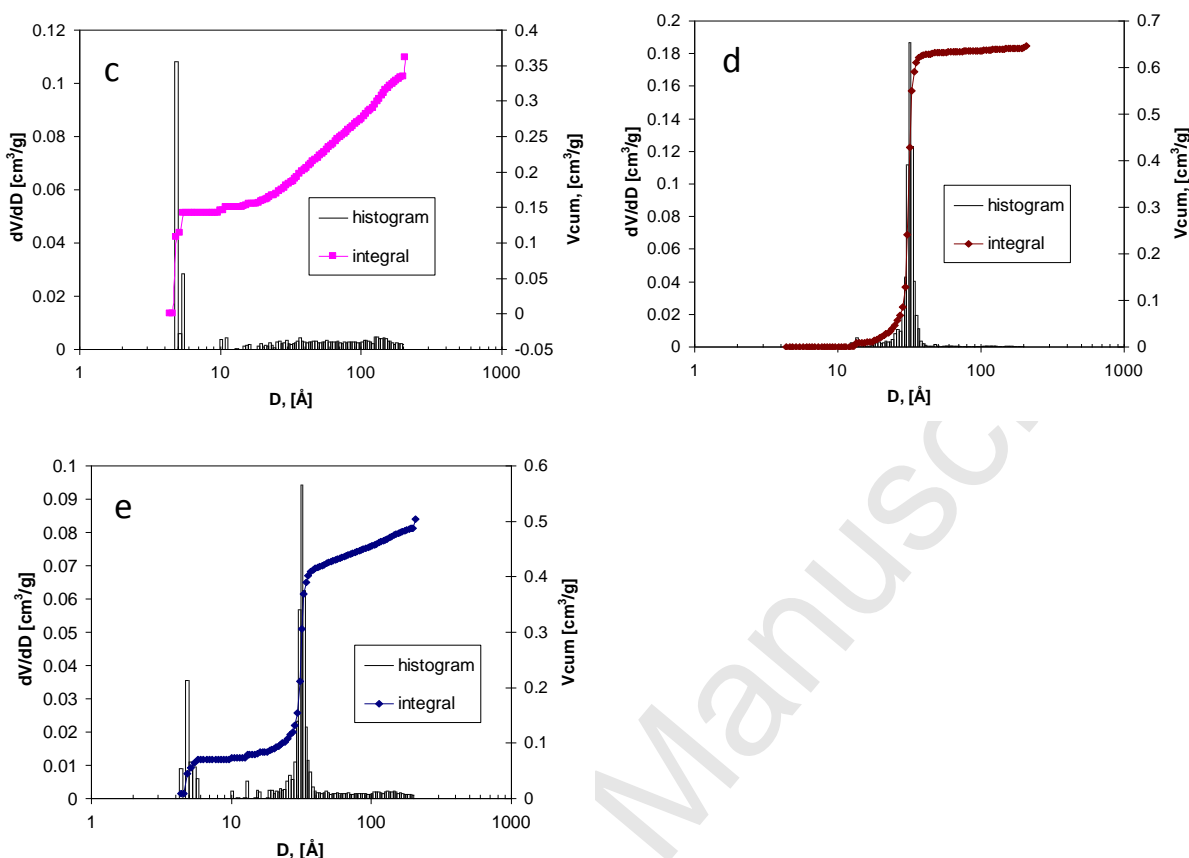


Figure 21. Test of the NLDFT model for zeolite-containing materials. (a) Argon adsorption isotherms at 87 K on MCM-41, ZSM-5 and their 50-50 mixture. (b) NLDFT fit of the isotherm on combined sample. (c-e) NLDFT pore size distributions for ZSM-5, MCM-41, and combined sample. The pore size distribution of the combined sample perfectly agrees with the sum of the pore size distributions of its constitutive parts. (Adapted from ref [62])

Another example of the NLDFT analysis of ZSM-5 zeolite materials of hierarchical structure was performed by Serrano et al. and is displayed in Figure 22 [169]. It is worth noting that the range of pore sizes that can be captured by the NLDFT method in these samples extends from 0.5 to 50 nm.

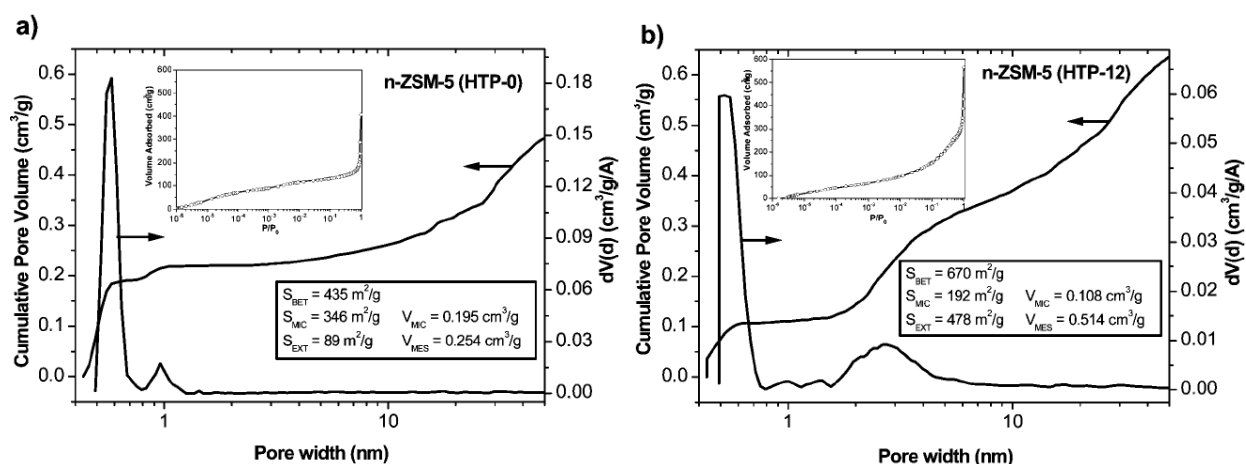


Figure 22. Pore size distributions and cumulative pore volumes for calcined nanocrystalline *n*-ZSM-5 materials prepared under high-temperature precrystallization (HTP) at 90 °C. Conditions include both (a) 0% and (b) 12% PHAPTMS surface-silanization agent. The NLDFT method was applied to obtain the pore size distributions assuming a cylindrical pore model and using the adsorption branch of the Ar isotherm at 87 K plotted on logarithmic scales (insets). Nomenclature corresponds to the following: BET surface area (S_{BET}); micropore surface area (S_{MIC}); external surface area (S_{EXT}) estimated as the difference $S_{\text{BET}} - S_{\text{MIC}}$; micropore volume (V_{MIC}) determined for pore sizes below 1.6 nm; and mesopore volume (V_{MES}) determined for pore sizes ranging from 1.6 to 50 nm. (Adapted from ref [169])

The above examples show that NLDFT method is applicable to various micro-mesoporous materials, including adsorbents, catalysts, separation membranes, sensors, and other zeolite-based systems [170, 171].

5.3.3. Metal-organic frameworks and related structures

The metal-organic frameworks (MOFs) porous coordination polymers represent a wide class of microporous crystals with well defined and orderly spaced pore channels and cages. Although, the surface chemistry of microporous crystals is by no means different from silica or carbon, the NLDFT and QSDFT methods originally developed for siliceous and carbonaceous materials have been effectively applied for structural characterization of MOFs. In particular, the NLDFT method for cylindrical pores was used for analysis of Ar isotherms on indium base metal-organic frameworks of soc topology (soc MOF) with channel pore structures[172]. This example is presented in Figure 23. Since the parameters for Ar-socMOF interactions are not

developed, the authors used two existing kernels with Ar-silica and Ar-carbon interaction parameters, and found that the pore size determined from the Ar-silica kernel produced the pore size in agreement with the crystallographic data.

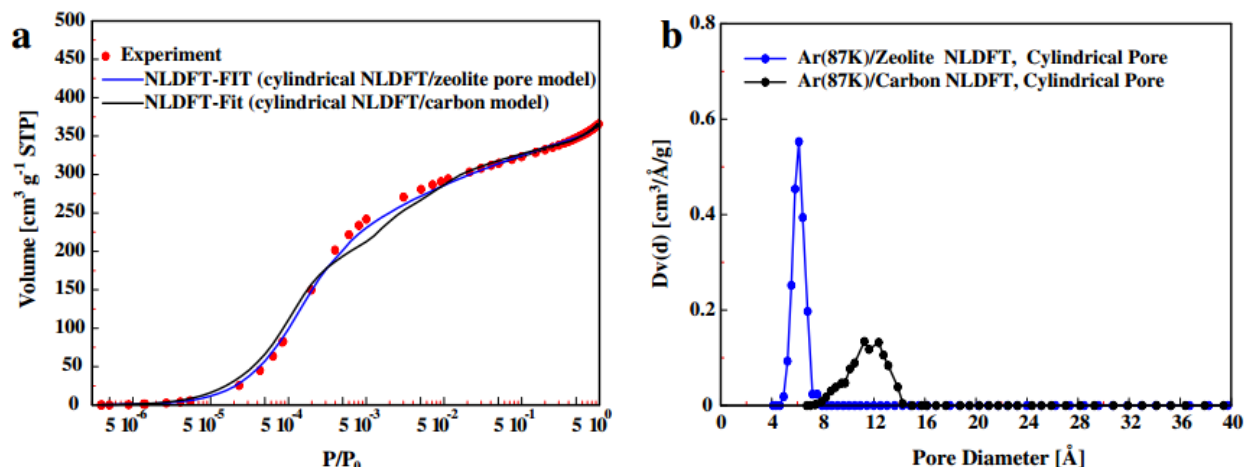


Figure 23. a) Experimental Argon (87.3 K) isotherm on socMOF and NLDFT fit for Argon adsorption at 87.3 K in cylindrical pores with either Ar-silica/zeolite or Ar-carbon interaction parameters. (b) Differential NLDFT pore size distribution curves. Pore size of 6.1 Å obtained from the NLDFT kernel with Ar-silica/zeolite parameters agrees well with the expected accessible pore diameter of the cylindrical-like main channels in soc-MOF. (Adapted from ref [172])

Covalent organic frameworks (COFs) are microporous crystals, similar in structure to MOFs. They differ from their inorganic/organic predecessors by the fact that they are held together solely by strong covalent bonds made from light elements (H,B,C,N,O). In 2005, Cote et al. employed the NLDFT method for characterization of COFs [173]. Ar, CO₂ and N₂ gas adsorption studies were used to validate the architectural stability of these compounds and the NLDFT method was applied to validate the existence of a hexagonal array of 1 dimensional mesopores. Like MCM-41, these structures reveal a reversible isotherm, with a sharp step between 0.11 and 0.15 P/P_0 for COF-5. This last feature is indicative of a narrow pore size distribution. The isotherms and the corresponding pore size distribution for N₂ gas adsorption measurements are shown in Figure 24 for both structures. For the two structures presented, COF-1 and COF-5, NLDFT results were corroborated with powder x-ray diffraction measurements to

confirm the presence of primary pores between 6 to 12 Å, and 27 Å, respectively. These structures were shown to be viable candidates for the storage of hydrogen, methane and carbon dioxide gas for clean energy applications [174].

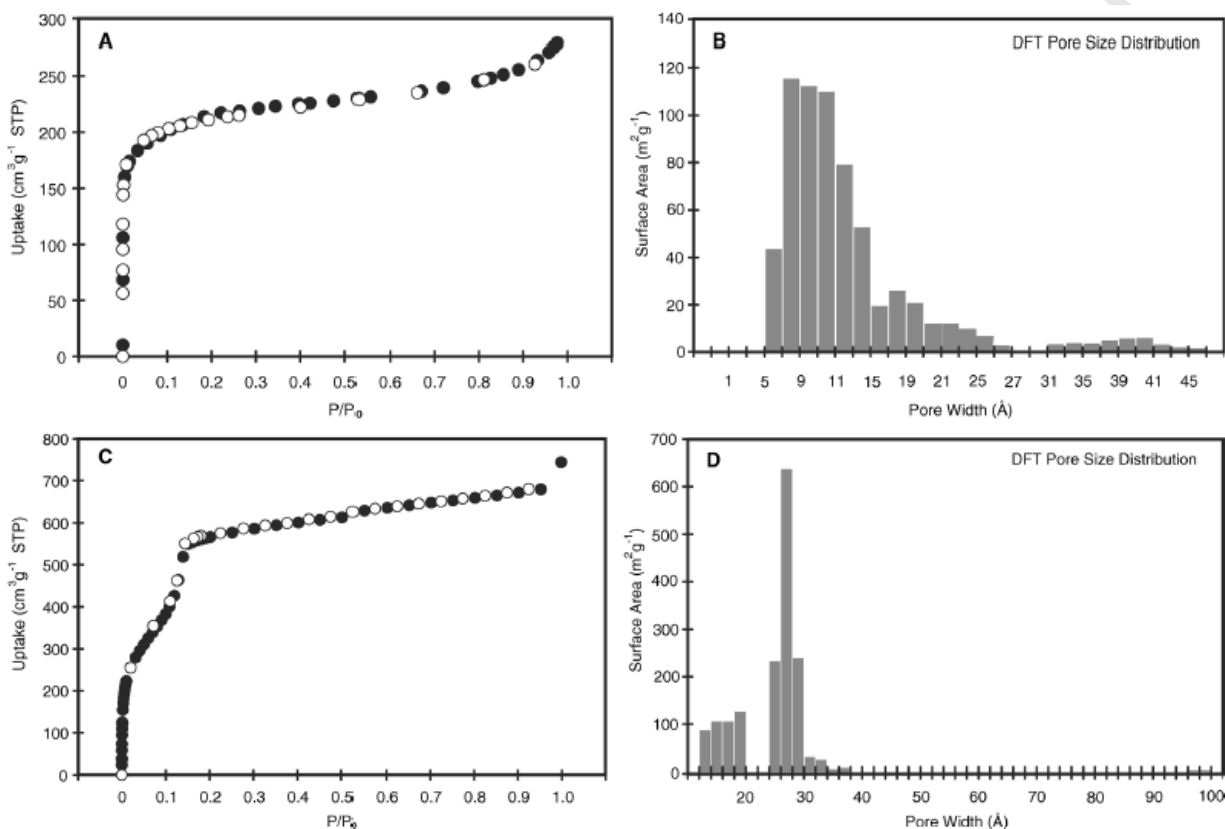


Figure 24. Nitrogen adsorption isotherms for COF-1 (a) and COF-5 (c) and the corresponding pore size distributions (b) and (d), respectively. (Adapted from Ref[173])

5.4. Disordered structures

Although originally developed for ordered silicas, the NLDFT cylindrical kernel can be employed for disordered systems and other inorganic porous materials for practical estimates. This should be done with an understanding that the reported values of pores sizes correspond to the effective cylindrical channels, in which the condensation/evaporation transitions occur at the same vapor pressure as in the real pores of a given material. In the case of disordered materials such as porous glass, the adsorbate-wall interaction remains the same. Kullmann et al. studied

nanoporous glass monoliths with pore sizes under 5 nm and compared the characterization results of NDLFT and positron annihilation lifetime spectroscopy (PALS), the latter being a technique to study voids and defects [175]. The authors obtained a type I isotherm, typical of microporous materials and applied the NDLFT equilibrium model for silicas. It can be seen from Figure 25 that the authors produced a porous glass with a bimodal distribution consisting primarily of micropores confirmed by the two independent methods.

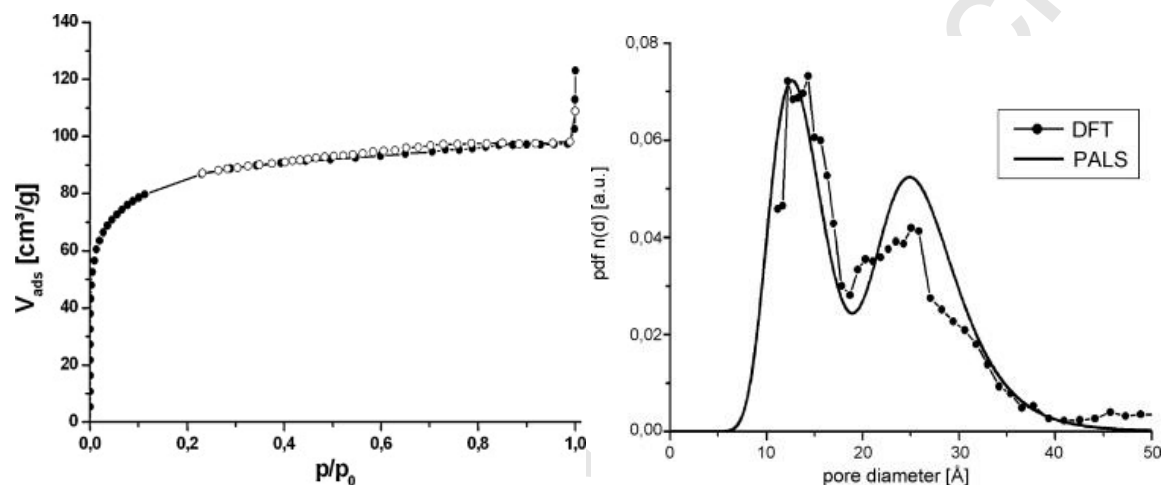


Figure 25. (Left) N₂ isotherm at 77 K for nanoporous glass monoliths. (Right) Overlay of NDLFT equilibrium model for cylindrical pores and PALS pore size distributions (distribution curves were normalized for the same maximum) (Adapted from ref [175])

The application of the NDLFT silica model can also hold true for a variety of oxides. Chavez et al. applied the NDLFT technique to characterize the synthesis of tungsten oxide (WO₃) films that displayed pore size distributions in both the meso and microporous ranges [176]. Likewise Zhou et al. developed a hard templating technique using mesoporous silica to fabricate mesoporous WO₃ [177]. The application of the NDLFT adsorption kernel for cylindrical silica pores indicated highly ordered pores with crystalline walls. Their results were validated against both TEM and XRD. Chandra et al synthesized zinc oxide (ZnO) by a templated method and the corresponding NDLFT characterization proved to be in good agreement with TEM results[178]. In the case of alumina, Landers et al. utilized the NDLFT kernel to show the evolution of a

bimodal distribution as a function of mixing time of alumina pastes, a change reflected in both the desorption isotherms and pore size distribution (Figure 26) [179].

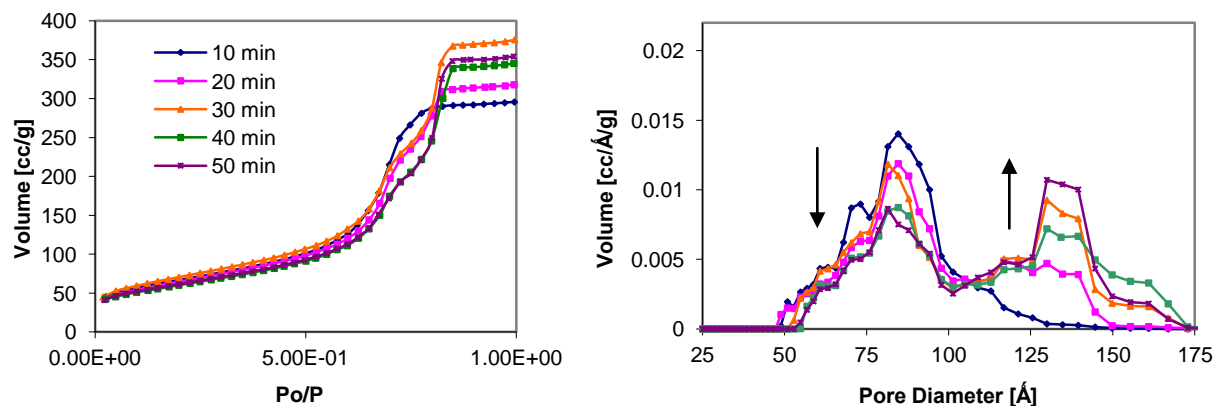


Figure 26. (Left) N_2 Desorption isotherms 77.4 K on extruded and calcined alumina pastes mixed with 1% acid displayed as function of mixing time. (Right) Pore size distribution calculated using NLDFT as a function of mixing time for 1% acid. (Adapted from ref [179])

5.5. Mesoporous crystals with cage-like pores: spherical pore model

The characterization of cage like silica structures (SBA-1, SBA-6, SBA-16, FDU-1, KIT-5, and FDU-12) has been impeded by the use of traditional kernels. First the accurate description of the transport pores via N_2 adsorption-desorption becomes invalid as they go past the lower limit of 5 nm. Matters are further complicated by mechanisms previously mentioned involving pore blocking and cavitation. These issues were resolved with the advent of a NLDFT kernel tailored for silica pores constituting of both spherical and cylindrical geometries [23, 35]. Tailored for hierarchical ordered porous materials, this kernel should be applied for systems containing cylindrical pores less than 5 nm and spherical pores greater than 5 nm. These materials typically exhibit a H2 hysteresis type loop resulting from pore blocking. It is thus recommended that the pore size analysis be based solely on the adsorption branch.

5.5.1 Cage-like structures with $Pm3n$ and $Im3m$ symmetry

SBA-1 represents the first class of materials resulting from the templating of supramolecular surfactant aggregates to form uniform spherical pores connected by smaller

transport pores [152]. Moreover, these pores had the ability to be tailored to different sizes and specifications by merely altering the synthesis conditions (pH, temperature, concentration). Of the new materials that emerged SBA-1 ($Pm3n$) and SBA-16 ($Im3m$) were notable in terms of their uniform and large cage like cavities with cubic symmetry. The NLDFT kernels capable of addressing hybrid pore structures led to the better characterization of materials relating to these symmetries as exemplified in Figure 27. The delayed drop on the desorption branch and the corresponding wide hysteresis loop that are displayed in Figure 27a is a manifestation of the process known as cavitation. The kernel developed for the latter was recently validated with XRD results stemming from the work of Miyasaka et al. [180] Several groups have employed the use of the NLDFT kernel in order to confirm their pore size distribution resulting from various synthesis conditions. Vinu et al. investigated the influence of acid to surfactant concentration as well as synthesis time on the pore size and stability of SBA-1 structures. They concluded that SBA-1 is mechanically more stable compared to mesoporous silica materials such as MCM-41 and SBA-15, but is mechanically comparable to the cubic structure of MCM-48 [181] (see section 5.5.4). Ting et al. were capable of synthesizing SBA-1 across a wide temperature range and composition range by using the template dodecyl trimethyl ammonium chloride ($C_{12}TMACl$) under strongly acidic conditions as opposed to the more conventional $C_{16}TMABr$ [182]. Kao was able to synthesize SBA-1 with the aid of D-fructose as an auxiliary agent[183]. Likewise, the same group was able to functionalize SBA-1 through several means. First with vinyl groups via a room temperature condensation reaction with tetraethoxysilane (TEOS) and trimethoxyvinylsilane (TMVS) templated by cetyltriethylammonium bromide (CTEABr) under acidic conditions[184]. In a proceeding paper the same group functionalized SBA-1 with phenyl groups via co-condensation of tetraethoxysilane (TEOS) and phenyltriethoxysilane

(PhTES)[185]. In both cases the presence of the functional groups was confirmed with the aid of NMR and the pore size distribution were confirmed with the aid of the hybrid NLDFT kernel.

Materials that exemplify a Im3m symmetry include both SBA-16 and FDU-1. SBA-16 was first synthesized in a low acidic medium (0.5 M HCl) using a silica source of either TEOS or TMOS [186]. Like SBA-15, SBA-16 can be synthesized by using triblock copolymers to produce large 3-dimensional mesoporous silicas. Typically these triblock polymers are relatively large PEO chains, the most common being F127, F108, and F98. The first example of the NLDFT applied to SBA-16 showed it to have a spherical cage size of 8.5 nm and a minimum wall thickness of 5.9 nm[23]. Likewise, the NLDFT kernel for spherical silica pores can be applied to FDU-1, first demonstrated by the Zhao group [187]. They studied the pore variations that arise during the synthesis of FDU-12 structures, most notably the effect of temperature on the cage like spherical pores and the cage entrances[188].

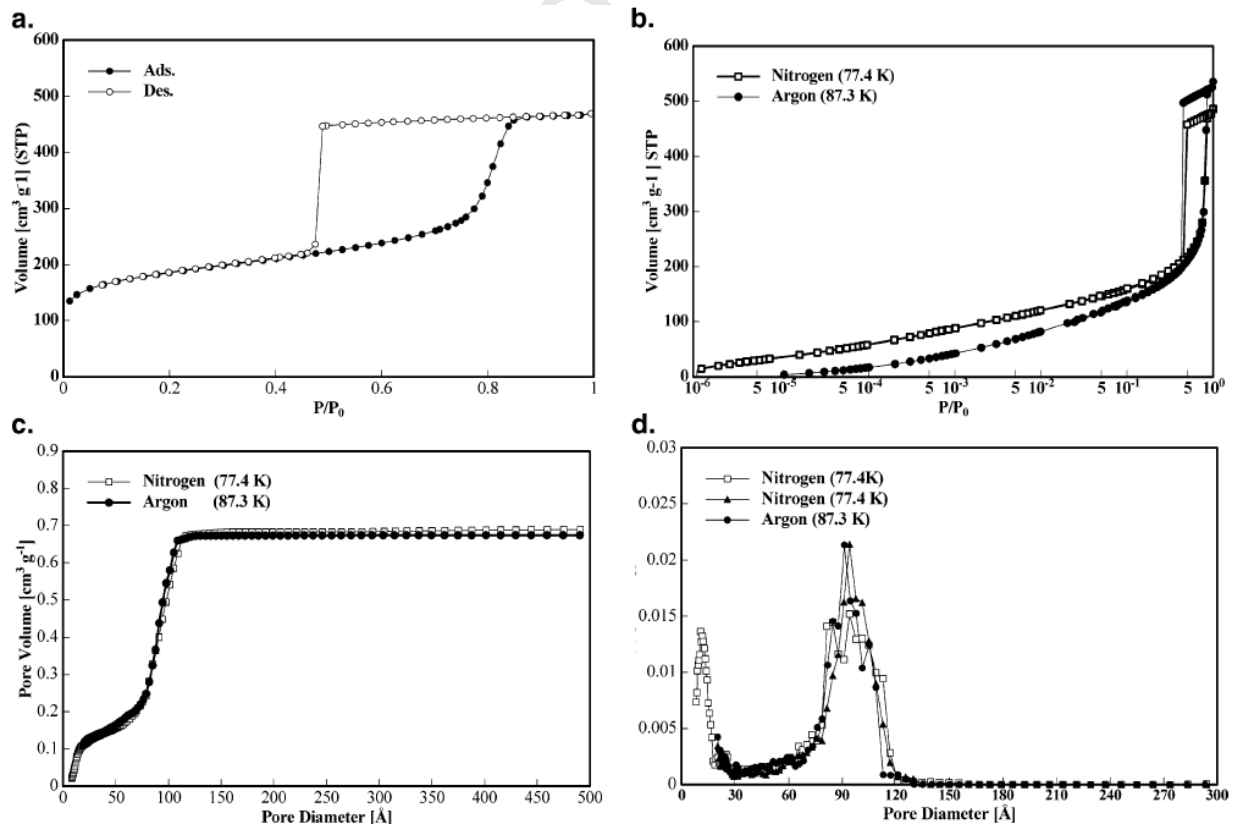


Figure 27. (a) High-resolution nitrogen (77.4 K) adsorption/desorption isotherm on SE3030 silica. (b) Comparison of nitrogen (77.4 K) and argon (87.3K) adsorption/desorption on SE3030 silica plotted on a semi logarithmic scale. (c) NLDFT cumulative pore volume plots calculated from the adsorption branch by applying the kernel of metastable adsorption isotherms based on a cylindrical pore model for silica. Both nitrogen at 77.4 K and argon at 87.3 K are displayed. (d) NLDFT pore size distributions from nitrogen at 77.4 K and argon at 87.3 K respectively. Distributions were calculated from the adsorption branch of the isotherm (see b and c) (Adapted from ref [36])

Esparza et al. synthesized a variety of SBA-16 through a common micelle templating technique ranging in pore sizes from 7.59-7.90 nm verified by the NLDFT technique[189]. Kleitz et al. were capable of producing SBA-16 materials synthesized in a EO106PO70EO106 (F127)-butanol-H₂O system under mildly acidic conditions[190]. They could fine tune the pore diameter by altering the hydrothermal treatment temperature producing cage dimensions varying between 6 to 12 nm. From these results they concluded that the NLDFT kernel was in excellent agreement with XRD modeling results. In a similar system, the authors demonstrated that they could tune the pore size between 4 and 7 nm by varying the initial mixture composition [191].

5.5.2 Cubic structures with $Fd3m$ and $Fm3m$ symmetry.

FDU materials derive its name from Fudan University in Shanghai [192, 193]. Like SBA-16, the unique pore structures of these FDU materials elicited the need for methods to accurately take into account their hybrid structure[35]. The pores in these materials consist of geometries similar to ink bottles, and gives rise to the challenges outlined in section 2.1 relating to the phenomena of pore blocking and cavitation. The synthesis involves three components, namely block copolymers, an organic solvent, and inorganic salts, which when combined properly and polymerized forms a template. Two routes can then be employed to attain either mesoporous silica or carbon. In the former a source of silica can be introduced in order to fill the voids of the mesoporous material with the polymer template being removed later in the process. In the latter,

no further carbon source is required, as the material can be merely carbonized under nitrogen gas to form a sturdy carbon framework. Several groups have validated the existence of spherical pores using the NLDFT kernels. Figure 28 shows the isotherms and corresponding pore size distribution for the Fm3m structure denoted in the literature as FDU-12 and the affect of hydrothermal treatment at different temperatures and salt concentrations.

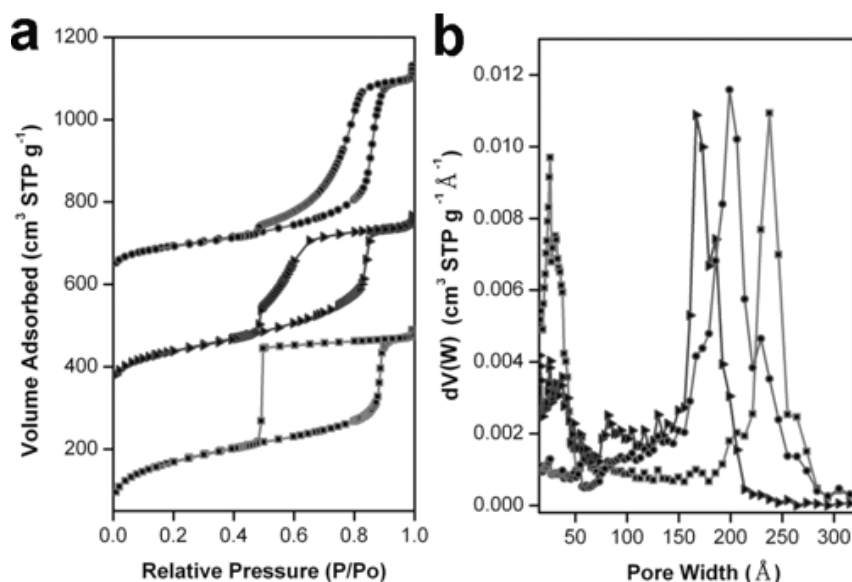


Figure 28. (a) Nitrogen sorption isotherms and (b) pore size distribution of calcined mesoporous silica FDU-12 samples. The plotted lines of L-FDU-12 and R-FDU-12 hydrothermally treated at 100 °C, and R-FDU-12 treated at 120 °C are denoted as solid squares, triangles, and circles, respectively. L and R refer to different amounts of salt in the synthesis procedure. The scale of adsorption volume in panel is shifted by 300 cm³/g for R-FDU-12 at 100 °C and 600 cm³/g for R-FDU-12 at 120 °C. (Adapted from ref [188])

First reported by Kleitz et al., KIT-5 is defined by a Fm3m symmetry with a spherical pore geometry interconnected by smaller pores [194]. The adsorption isotherm features a type IV classification with a sharp capillary condensation step at high relative pressures. KIT-5 is further defined by a H2 hysteresis loop, indicative of uniform spherical pores. Several investigators have applied the NLDFT method in determining the effect of synthesis modulation on these 3D spherical structures. Yang et al. attempted a post synthesis technique on KIT-5 samples treated

with H_2SO_4 [195]. They used Ar at 87 K in order to reduce any interaction which may arise with the different surface chemistry related to either the calcined or acid treated samples. From NLDFT analysis it was demonstrated that the acid treated KIT-5 samples exhibited a much larger pore volume compared to their calcined counterparts. However, the largest surface areas were obtained from the calcined samples due mostly in part to the contribution of intrawall microporosity from the block copolymer templates. These results were confirmed by Wu et al. who studied the post-synthesis structural modulation of KIT-5 as shown in Figure 29 [196]. On one hand, they were able to show that treatment with NH_4OH in general gave smaller mesopore cage sizes and lower micropore volume. On the other hand, treatment with H_2SO_4 produced mesopores with larger cage-like structures containing larger pore entrances but a decrease in the ultramicro pore volume. Their acid treated KIT-5 samples are displayed in Figure 29 where the as synthesized samples of KIT-5 are treated with a fixed concentration of acid at various times. The evolution of the hysteresis loop corresponds to a change from a H2 to a H1 hysteresis loop. This in turn implies a change in the pore morphology. This is displayed in the NLDFT calculated PSD results which show a decrease in microporosity with increased acid treatment duration.

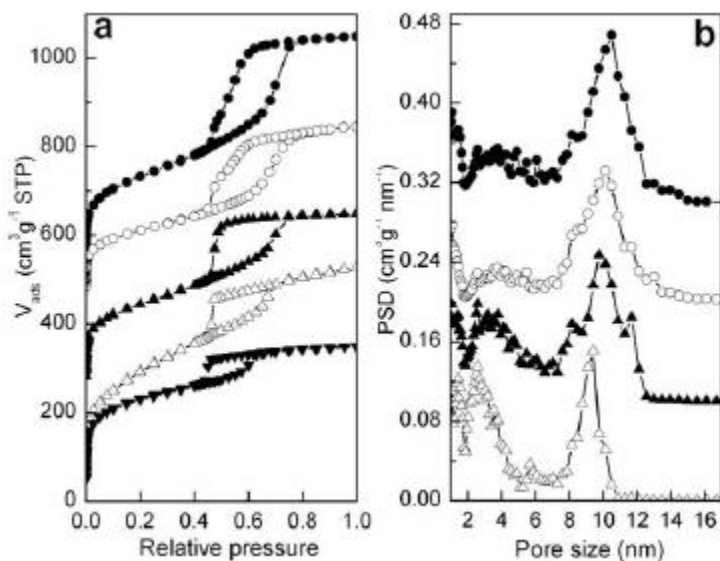


Figure 29.(a) Nitrogen isotherms of KIT-5 treated with acid for various durations. KIT-5-0h (\blacktriangledown), KIT-5-1h (\triangle), KIT-5-5h (\blacktriangle), KIT-5-10h (\circ) and KIT-5-24h (\bullet). The isotherms are shifted by

40, 260, 460 and 510 $\text{cm}^3 \text{g}^{-1}$ STP, respectively. (b) Pore size distributions of the acid-treated materials calculated from the adsorption branches by using the NLDFT method. The offset between each PSD is 0.1 $\text{cm}^3 \text{g}^{-1} \text{nm}^{-1}$. [196]

5.6. QSDFT model for silica materials.

Application of the NLDFT method for characterization of silica materials did not reveal artifacts in PSDs related to the layered structure of the theoretical isotherms as it was observed in carbons (see section 4.2). QSDFT predictions in the region of film adsorption (prior to the capillary condensation) provide excellent agreement to the experimental adsorption data on SBA-15 silica (Fig 5 b) [48], which could not be achieved with a NLDFT isotherm that exhibits layering steps. Giving the more advanced and realistic model for silica surface, QSDFT tends to replace NLDFT for characterization of silicas, including MCM-41 [197], SBA-16 [180] and others.

5.7. Cavitation as a negative factor in pore size analysis

Complexity can arise in hierarchical systems comprised of both micro-mesopores that creates a wider variety in the observed hysteretic behavior. This complexity is inherent to the adsorbed fluid and surrounding pore system and can mask phenomena such as pore blocking and cavitation resulting from desorption. From a characterization stand point this can complicate matters. However if the hysteresis loop is interpreted correctly it can provide a myriad of information about the pore network morphology. For the case of cavitation the pore size is obscured, as the point of desorption is weakly correlated with the pore size. Cavitation occurs during the desorption process resulting from the spontaneous nucleation and growth of gas bubbles in the metastable fluid confined in the pores[128]. The process leading up to this spontaneous act involves a prolonged metastable state of the condensed fluid which is overstretched by capillary pressure. It is typically inherent to spherical pore systems connected

by smaller necks seen in Figure 30. Both theoretical and experimental [23, 36] studies have shown that if this neck diameter is smaller than some critical size then cavitation will occur. In the case of nitrogen at 77.4 K this is estimated to be 5 nm.

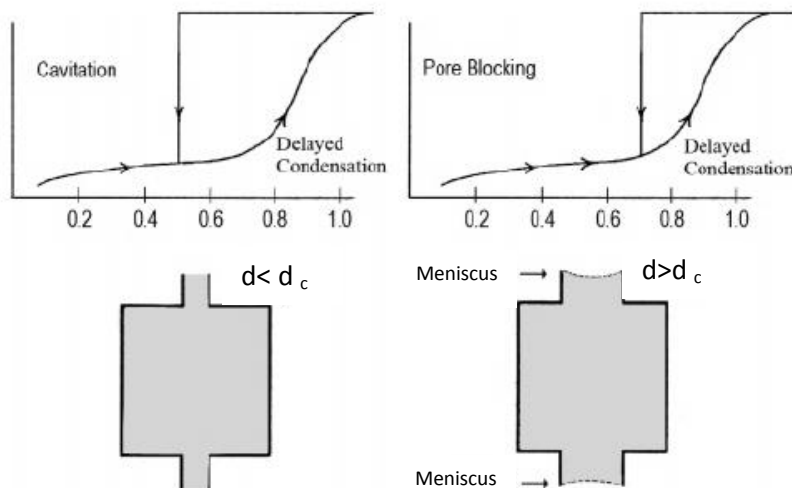
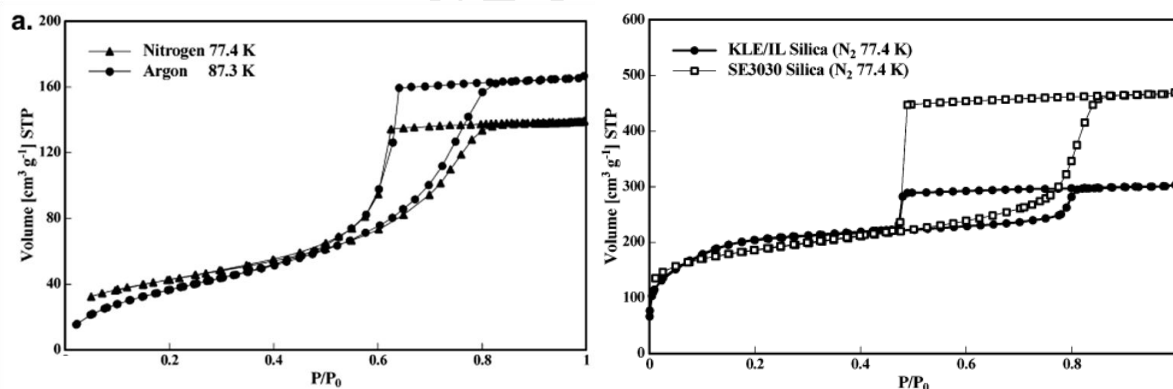


Figure 30: Schematic illustration of cavitation and pore blocking where the variable d indicates the neck size of the pore [36]

Desorption isotherms of materials with pore networks composed of unequal pores are always affected by either pore blocking [121] or cavitation effects [128]. For the case of pore-blocking, the desorption isotherm may have information on the distribution of the pore necks (connecting channels), which can be derived by applying a hybrid cylindrical-spherical kernel [36], or more elaborated percolation models[198]. How can one distinguish between the cavitation mechanism of evaporation from the pore-blocking? The first criterion is the pressure. It has been shown that homogeneous cavitation of nitrogen in pores takes place at the relative pressures of 0.4-0.5, almost irrespective of the pore size [128]. Characteristic example is shown in Figure 7, where the desorption isotherm possess the “cavitation” step that causes an artificial peak on the PSDs around 4 nm. It is worth noting, that such artificial peaks are frequently found in the literature when the PSD is calculated from the desorption isotherm, which exhibit a step about $p/p_0 = 0.4-0.5$ (in the case of nitrogen adsorption at 77.4 K). At the same time, there are

materials, e.g. MCM-41 [14], which do have pores in the range 4-5 nm and as such exhibit the capillary desorption step in the same interval relative pressure that is characteristic for cavitation.

On the basis of the DFT method Thommes et al. proposed a simple criteria to distinguish, whether the desorption branch of an isotherm is affected by pore blocking or cavitation [36]. They used experimental data from two adsorptives, nitrogen (77.4 K) and argon (87.3 K), and calculated PSDs by means of applying the N₂ and Ar hybrid NLDFT kernels to the desorption branches of the corresponding isotherms. For Vycor glass, where desorption is affected by pore blocking, the resulting PSDs were close (Figure 31 a), since they were determined by the pressure of equilibrium desorption from the connecting throats. On the contrary, for SE3030 silica, where the desorption is affected by cavitation, the resulting PSDs are noticeably different. The cavitation pressure depends weakly on the pore size, and is mainly determined by the properties of the fluid. This method was employed recently to determine the mechanism of desorption in the 3DOm carbons [61], discussed in section 4.3.2.



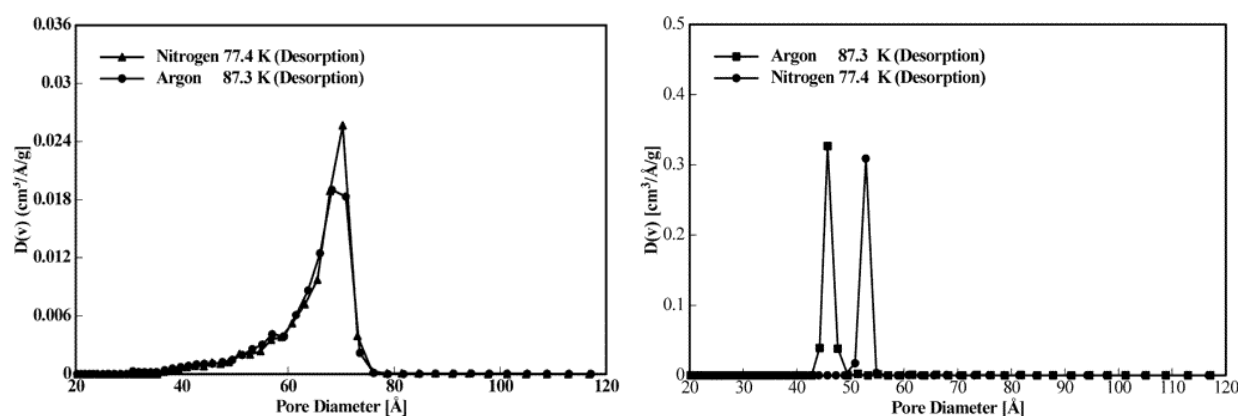


Figure 31. Distinguishing between cavitation effects in materials. Isotherms for the systems nitrogen (77.4 K)/silica and argon (87.3K) /silica. (a) for Vycor glass (b) for SE3030 silica. Their respective NLDFT pore size distribution curves obtained from the desorption branches of the sorption data by applying the NLDFT equilibrium transition kernel (on the basis of a cylindrical pore model)(Adapted from ref. [36]).

A characteristic example of the cavitation mechanism is illustrated in Figure 31. Van Der Voort et al. [28] modified the parental SBA-15 materials by synthesizing plugged hexagonal templated silica (PHTS). In the SBA-15 structure with open cylindrical channels, the adsorption-desorption isotherm forms a classical H1 hysteresis loop with the desorption branch reflecting equilibrium capillary evaporation, Figure 32A. In PHTS, the mesopore channels contain microporous silica nanocapsules or plugs, which partially block the channels and separate them into compartments that resemble ink-bottle pores. Depending on the amount of plugs, they may block either all mesopores, or keep some of mesopores open. The former case is exemplified by PHTS-3 sample with a wide hysteresis loop formed by adsorption and desorption isotherms, Figure 32B. The capillary condensation step on adsorption isotherm is located at the same position as for the parental SBA-15 (Figure 32A), while the desorption step is shifted to the lower relative pressure of ~ 0.45 characteristic of the cavitation mechanism. This behavior is typical for ink-bottle pores with narrow necks as shown in Figure 30. In the latter case, exemplified by PHTS-2, the desorption isotherm has two steps, the first step reflects evaporation

from the open pores and the second step is caused by cavitation in the blocked pores. If proper care is not taken and the PSD is calculated from the desorption branch the second step would produce an artificial peak on the PSD in the region pores of 4-5 nm, which does not exist in this material. However, when the cavitation effect is accounted for and the second step is neglected, the PSDs calculated with the NLDFT method turns out to be almost identical.

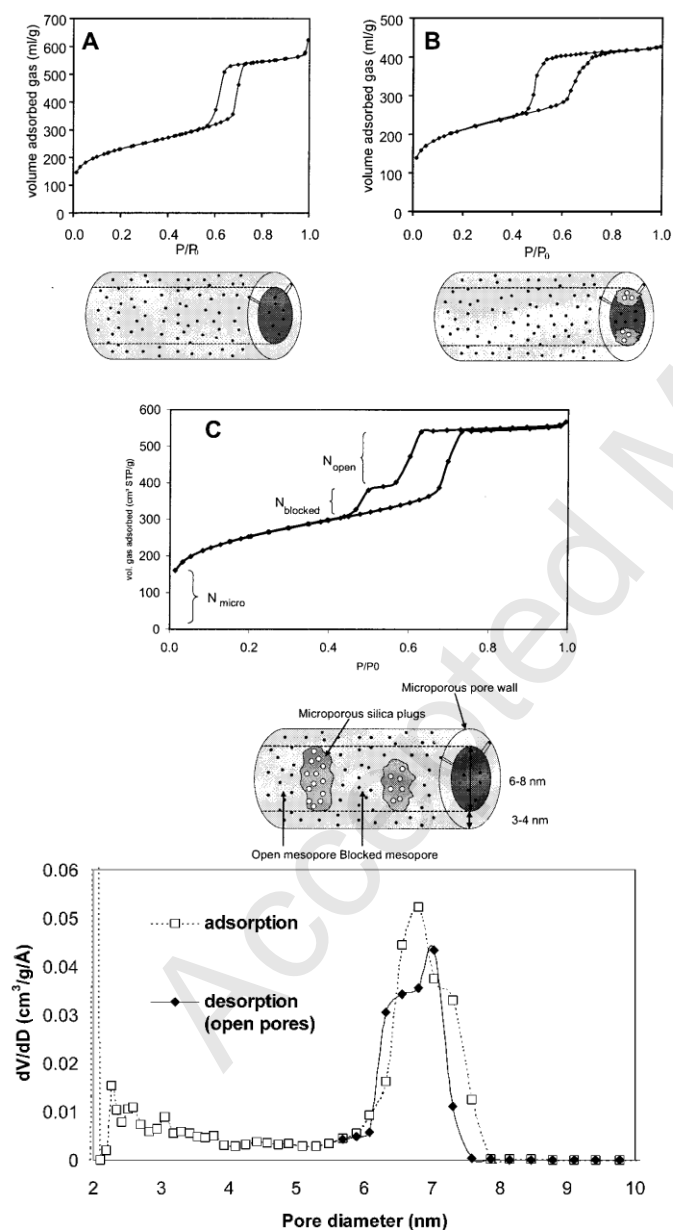


Figure 32: Nitrogen adsorption-desorption isotherms of (A) pore system with open mesopores (SBA-15); (B) pore system with plugged mesopores (ink-bottle pores) (PHTS-3), and (C) pore system with partially plugged mesopores, comprising both open and blocked mesopores (PHTS-2). (D) NLDFT pore size distributions calculated from adsorption and desorption isotherms accounting for the cavitation artifact by neglecting the second step on the desorption isotherm (PHTS-2). (Adapted from refs [27, 28])

6. DFT models for interpretation of in-situ XDR data

In a series of papers [53, 180, 197], the QSDFT method was extended to describe the observations of the in-situ XDR measurements on mesoporous crystals of MCM-41 and SBA-16 types. The strategy for the QSDFT approach for modeling of diffraction patterns is as follows. The parameters of fluid-solid interactions are taken from the literature, see Table 3. The parameters for the solid density distribution, solid density and roughness parameter, are taken from the reconstruction of the XRD patterns on the dry sample. The temperature of the XRD experiments, which is maintained by blowing liquid nitrogen and is not measured directly at the adsorbent, is determined from the agreement of the measured XRD pressure of capillary condensation pressure and the prediction by the QSDFT model with adopted energetic and structural parameters. Then, the calculation of the density profiles of adsorbed fluid is performed at a series of gas pressures and the predicted XDR patterns are obtained by the Fourier transform converting the fluid and solid densities into the electron density.

An example of such approach is illustrated in Figures 33 and 34 for the Ar adsorption on an MCM-41 sample with a mean pore diameter of 36.8 Å[53]. From the comparison with the QSDFT predictions for the hexagonal array of cylindrical silica pores with the roughness parameter of $\delta=4\text{\AA}$, the XRD experiment temperature was determined to be 83 K. The calculated fluid density profiles (DP) in the pores are in agreement with those reconstructed from the XRD patterns electron density profiles, Figure 33. Note that the QSDFT model correctly predicts the increase of adsorption in the pore wall corona and the growth of the adsorption film. In Figure 34, the calculations by the Fourier transform diffraction intensity are compared with the experimental XRD data for 10, 11, and 20 reflections. An analogous study was performed [180] for cubic cage-like structures of SBA-16 crystals. Almost quantitative correspondence of

theoretical and experimental data suggests that the QSDFT method correctly captures the main physical mechanisms of physical adsorption on mesoporous crystals with minimum additional structural and energetic parameters, which can be determined from the independent measurements.

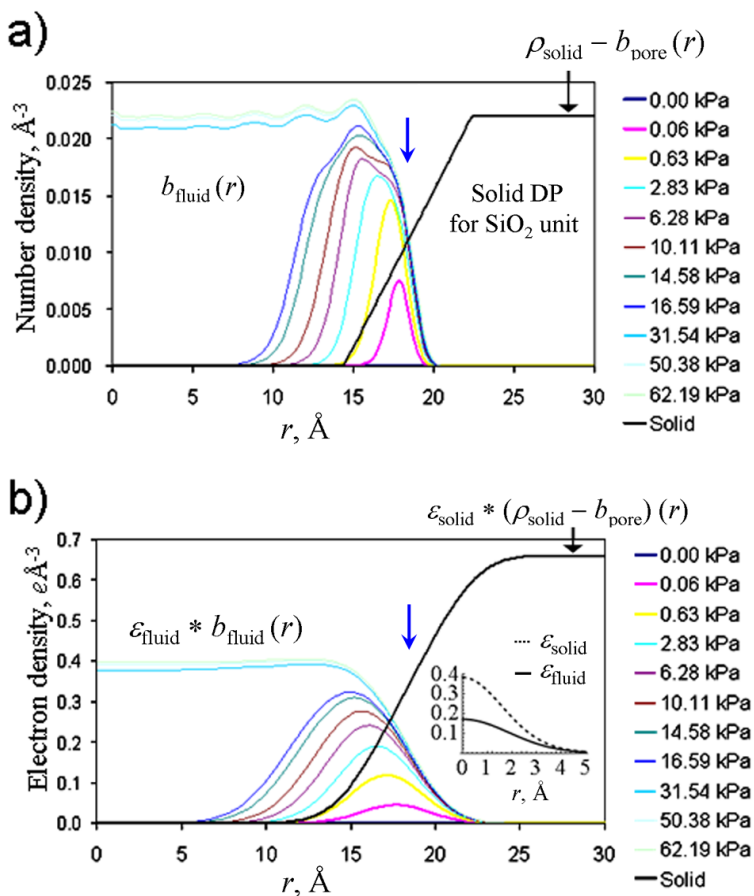


Figure 33. Evolution of the mass and electron density profiles of adsorbed fluid in the process of adsorption. Ar adsorption at T=83K in cylindrical pores of MCM-41 sample at different Ar pressures in the gas phase (the pressure values are shown in the left column). a) – QSDFT fluid density profiles in the silica pore of diameter $D=36.8\text{\AA}$ with the roughness parameter $\delta=4\text{\AA}$, the color corresponds to the pressure shown on the left, solid density is plotted in black; b) – reconstructed electron density profiles for fluid and solid from in-situ XRD measurements (kernel for the electron spread of solid and fluid shown in the insert), the color corresponds to the pressure shown on the left, solid density is plotted in black. Blue arrows indicate the position of the mean pore radius, 18.4\AA . (Adapted from ref [53])

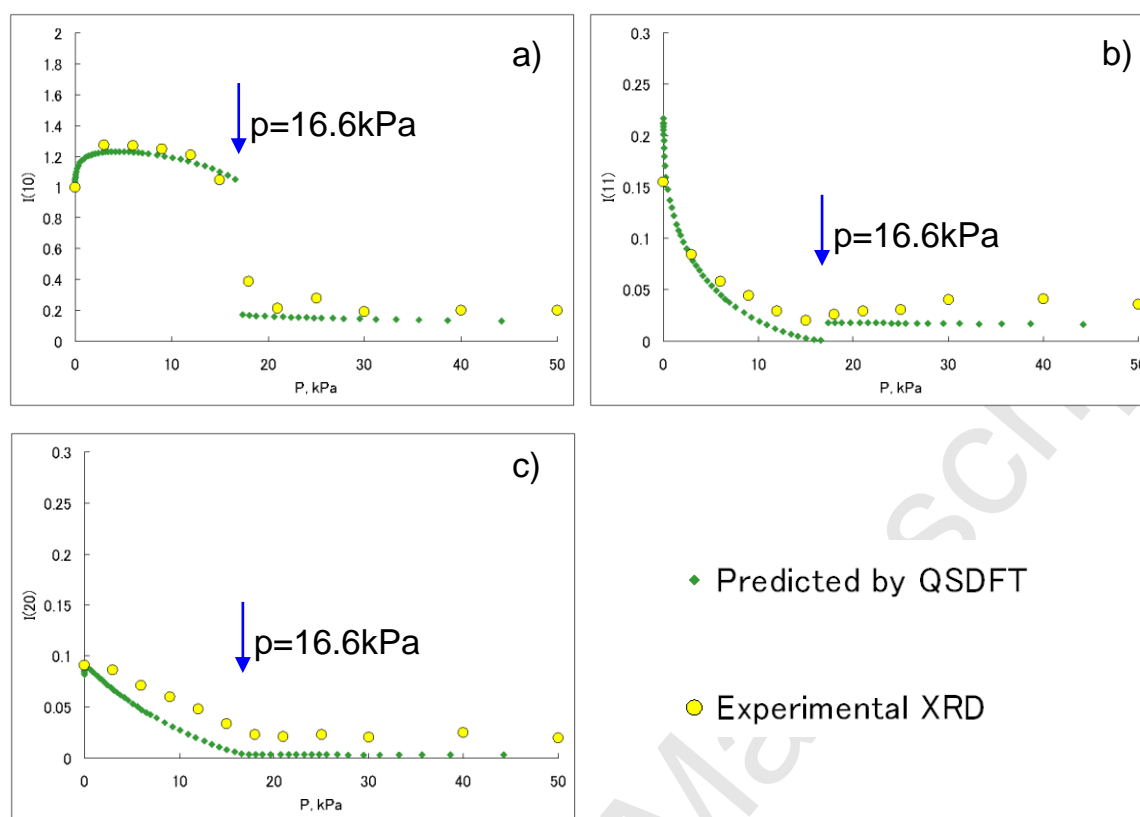


Figure 34. QSDFT prediction of the XRD intensities. Comparison of the theoretical diffraction intensities calculated from density profiles of QSDFT and the experimental diffraction intensities measured during in situ powder XRD for Ar adsorption on MCM-41 mesoporous crystal. (a) 10, (b) 11, and (c) 20 reflections are presented. The capillary condensation takes place at 16.6 kPa at $T=83$ K. (Adapted from ref [53])

7. Concluding Remarks and Future Outlook

It has been more than 20 years since the DFT method has been first suggested for calculating the pore size distribution of carbons from nitrogen adsorption data [8]. Since then with a series of modifications, the non-local density functional theory (NLDF) method [10-12] has become the most widely used method for adsorption characterization of micro-and mesoporous materials of various origins. It was implemented in the software packages of commercial adsorption instruments and recommended as a standard by ISO [16]. Recent advance of the quenched solid density functional theory (QSDFT), introduced the surface roughness as the additional structural parameter characterizing the pore wall heterogeneity. The main

advantages of the DFT methods are related to its rigorous theoretical basis that covers the whole region of micro- and mesopores and provides an opportunity of customization to different adsorbates (nitrogen, argon and carbon dioxide), materials (silicas and carbons), and pore morphologies (slit-like, cylindrical, and spherical); the hybrid models that include different groups of pores were designed for hierarchical materials. These opportunities are discussed in this review with typical examples of active carbons and carbon fibers, carbon nanotubes, templated mesoporous carbons and silicas, MOFs and COFs, disordered and hierarchical structures, alumina catalysts, *etc.*

A library of NLDFT and QDSFT kernels is in continuous development motivated by an avalanche of discoveries of novel designer porous materials, which require the characterization methods that account for the geometrical and chemical specifics of their pore architecture. As such, the users of pore structure characterization instruments, who in the past used standard BJH, BET, and DR methods for any systems considered, have now a challenge of making an educated choice, which method from the available library would be better suited for this or that particular system. Which adsorbate is more suitable for the pore size analysis? Which model pore morphology would mimic better given material? Which branch of the hysteric adsorption isotherm should be taken for the analysis? How to discriminate the pore blocking or cavitation effects that may lead to artificial PSDs? How to estimate the structural parameters of the systems, which are beyond the groups of materials, for which currently available kernels were designed and verified? These questions are addressed, at least in part, in this review, which serves as a brief guidance to the practitioners interested in getting a better understanding of the current capabilities and limitations of the DFT methods.

Finally we should note that even after two decades of DFT methods development for porous materials characterization, there still remain a number of issues, which are not currently resolved. The fundamental challenges for future advances include:

- accounting for the networking effects and transition from the models of independent pores to the pore networks. This requires a better understanding of the cooperative nature of capillary hysteresis in intersecting and corrugated pores [199], [200], [122], and developing percolation type models [198] based on the DFT description of adsorption in individual pores [210];
- accounting for the adsorption-induced deformation of porous framework. In the current DFT models, the solid structure is assumed inert and unchanged during adsorption. However, all materials contract or expand upon adsorption depending on the pore structure specifics. This effect is negligible for silicas [201, 202] and carbons [203, 204], but it is substantial for aerogels [205] and metal-organic frameworks, which can swell and breath during adsorption changing the volume by tens of percent [206]. In recent works [207-209], the DFT models were used for analysis of coal deformation during CO₂ sequestration and secondary methane recovery;
- developing the DFT methods for multicenter molecules, which would require the use of more elaborated density functional beyond the Tarazona [13] and Rosenfeld [18, 19] functionals employed in the available DFT library.

Acknowledgements

The authors are grateful to the Rutgers NSF ERC for Structural Organic Particulate Systems, Rutgers Catalyst Manufacturing Consortium, and Quantachrome Instruments for partial support of this work, and to Matthias Thommes and Richard Cimino for helpful discussions.

References

- [1] J.S. Beck, J.C. Vartuli, W.J. Roth, M.E. Leonowicz, C.T. Kresge, K.D. Schmitt, C.T.W. Chu, D.H. Olson, E.W. Sheppard, S.B. McCullen, J.B. Higgins, J.L. Schlenker, A new family of mesoporous molecular-sieves prepared with liquid-crystal templates, *Journal of the American Chemical Society* 114 (1992) 10834-10843.
- [2] C.T. Kresge, M.E. Leonowicz, W.J. Roth, J.C. Vartuli, J.S. Beck, Ordered mesoporous molecular-sieves synthesized by a liquid-crystal template mechanism, *Nature* 359 (1992) 710-712.
- [3] Brunauer S., Emmett P.H., Teller E., Adsorption of gases in multi-molecular layers, *Journal of American Chemical Society* 60 (1938) 309-319.
- [4] E.P. Barrett, L.G. Joyner, P.P. Halenda, The Determination of Pore Volume and Area Distributions in Porous Substances. I. Computations from Nitrogen Isotherms, *Journal of the American Chemical Society* 73 (1951) 373-380.
- [5] R. Evans, U.M.B. Marconi, P. Tarazona, Fluids in narrow pores: Adsorption, capillary condensation, and critical points, *The Journal of Chemical Physics* 84 (1986) 2376-2399.
- [6] R. Evans, U.M.B. Marconi, P. Tarazona, Capillary Condensation and Adsorption in Cylindrical and Slit-Like Pores, *Journal of the Chemical Society-Faraday Transactions II* 82 (1986) 1763-1787.
- [7] R. Evans, P. Tarazona, Theory of Condensation in Narrow Capillaries, *Physical Review Letters* 52 (1984) 557-560.
- [8] N.A. Seaton, J. Walton, N. Quirke, A new analysis method for the determination of the pore-size distribution of porous carbons from nitrogen adsorption measurements, *Carbon* 27 (1989) 853-861.
- [9] L.H. Cohan, Sorption Hysteresis and the Vapor Pressure of Concave Surfaces, *Journal of the American Chemical Society* 60 (1938) 433-435.
- [10] C. Lastoskie, K.E. Gubbins, N. Quirke, Pore-Size Distribution Analysis of Microporous Carbons - a Density-Functional Theory Approach, *Journal of Physical Chemistry* 97 (1993) 4786-4796.
- [11] J.P. Olivier, W.B. Conklin, M.v. Szombathely, Determination of Pore Size Distribution from Density Functional Theory: A Comparison of Nitrogen and Argon Results, in: J. Rouquerol, F. Rodriguez-Reinoso, K.S.W. Sing, K.K. Unger (Eds.), *Studies in Surface Science and Catalysis*, Elsevier, 1994, pp. 81-89.
- [12] P.I. Ravikovitch, S.C. O'Donnai, A.V. Neimark, F. Schuth, K.K. Unger, Capillary hysteresis in nanopores: Theoretical and experimental studies of nitrogen adsorption on MCM-41, *Langmuir* 11 (1995) 4765-4772.
- [13] P. Tarazona, Free-Energy Density Functional for Hard-Spheres, *Physical Review A* 31 (1985) 2672-2679.
- [14] A.V. Neimark, P.I. Ravikovitch, M. Grun, F. Schuth, K.K. Unger, Pore size analysis of MCM-41 type adsorbents by means of nitrogen and argon adsorption, *Journal of Colloid and Interface Science* 207 (1998) 159-169.
- [15] P.I. Ravikovitch, A. Vishnyakov, R. Russo, A.V. Neimark, Unified approach to pore size characterization of microporous carbonaceous materials from N₂, Ar, and CO₂ adsorption isotherms, *Langmuir* 16 (2000) 2311-2320.
- [16] ISO-15901-3, Pore size distribution and porosity of solid materials by mercury porosimetry and gas adsorption, Analysis of micropores by gas adsorption, 2007.

- [17] R. Roland, Fundamental measure theory for hard-sphere mixtures: a review, *Journal of Physics: Condensed Matter* 22 (2010) 063102.
- [18] Y. Rosenfeld, Free-Energy Model for the Inhomogeneous Hard-Sphere Fluid Mixture and Density-Functional Theory of Freezing, *Physical Review Letters* 63 (1989) 980-983.
- [19] Y. Rosenfeld, M. Schmidt, H. Lowen, P. Tarazona, Fundamental-measure free-energy density functional for hard spheres: Dimensional crossover and freezing, *Physical Review E* 55 (1997) 4245.
- [20] A.V. Neimark, Y. Lin, P.I. Ravikovitch, M. Thommes, Quenched solid density functional theory and pore size analysis of micro-mesoporous carbons, *Carbon* 47 (2009) 1617-1628.
- [21] J.D. Weeks, D. Chandler, H.C. Andersen, Role of Repulsive Forces in Determining Equilibrium Structure of Simple Liquids, *Journal of Chemical Physics* 54 (1971) 5237-&.
- [22] W.A. Steele, *The Interactions of Gases with Solid Surfaces*, Pergamon, Oxford, 1974.
- [23] P.I. Ravikovitch, A.V. Neimark, Density functional theory of adsorption in spherical cavities and pore size characterization of templated nanoporous silicas with cubic and three-dimensional hexagonal structures, *Langmuir* 18 (2002) 1550-1560.
- [24] A.V. Neimark, P.I. Ravikovitch, Capillary condensation in MMS and pore structure characterization, *Microporous and Mesoporous Materials* 44 (2001) 697-707.
- [25] P.I. Ravikovitch, A.V. Neimark, Density Functional Theory Model of Adsorption Deformation, *Langmuir* 22 (2006) 10864-10868.
- [26] P.I. Ravikovitch, A.V. Neimark, Characterization of micro- and mesoporosity in SBA-15 materials from adsorption data by the NLDFT method, *Journal of Physical Chemistry B* 105 (2001) 6817-6823.
- [27] P. Van Der Voort, P.I. Ravikovitch, K.P. De Jong, M. Benjelloun, E. Van Bavel, A.H. Janssen, A.V. Neimark, B.M. Weckhuysen, E.F. Vansant, A new templated ordered structure with combined micro- and mesopores and internal silica nanocapsules, *Journal of Physical Chemistry B* 106 (2002) 5873-5877.
- [28] P. Van Der Voort, P.I. Ravikovitch, K.P. De Jong, A.V. Neimark, A.H. Janssen, M. Benjelloun, E. Van Bavel, P. Cool, B.M. Weckhuysen, E.F. Vansant, Plugged hexagonal templated silica: a unique micro- and mesoporous composite material with internal silica nanocapsules, *Chemical Communications* (2002) 1010-1011.
- [29] A.V. Neimark, P.I. Ravikovitch, A. Vishnyakov, Bridging scales from molecular simulations to classical thermodynamics: density functional theory of capillary condensation in nanopores, *Journal of Physics-Condensed Matter* 15 (2003) 347-365.
- [30] M. Kruk, M. Jaroniec, A. Sayari, Adsorption Study of Surface and Structural Properties of MCM-41 Materials of Different Pore Sizes, *The Journal of Physical Chemistry B* 101 (1997) 583-589.
- [31] M. Carrott, A.J.E. Candeias, P.J.M. Carrott, P.I. Ravikovitch, A.V. Neimark, A.D. Sequeira, Adsorption of nitrogen, neopentane, n-hexane, benzene and methanol for the evaluation of pore sizes in silica grades of MCM-41, *Microporous and Mesoporous Materials* 47 (2001) 323-337.
- [32] W.W. Lukens, P. Schmidt-Winkel, D. Zhao, J. Feng, G.D. Stucky, Evaluating Pore Sizes in Mesoporous Materials: A Simplified Standard Adsorption Method and a Simplified Broekhoff-de Boer Method, *Langmuir* 15 (1999) 5403-5409.
- [33] Y.-H. Yue, A. Gédéon, J.-L. Bonardet, J.B. d'Espinose, N. Melosh, J. Fraissard, Direct incorporation of Al in SBA mesoporous materials: characterization, stability and catalytic activity, *Stud. Surf. Sci. Catal.* 129 (2000) 209-218.

- [34] A. Sayari, P. Liu, M. Kruk, M. Jaroniec, Characterization of Large-Pore MCM-41 Molecular Sieves Obtained via Hydrothermal Restructuring, *Chemistry of Materials* 9 (1997) 2499-2506.
- [35] P.I. Ravikovitch, A.V. Neimark, Experimental confirmation of different mechanisms of evaporation from ink-bottle type pores: Equilibrium, pore blocking, and cavitation, *Langmuir* 18 (2002) 9830-9837.
- [36] M. Thommes, B. Smarsly, M. Groenewolt, P.I. Ravikovitch, A.V. Neimark, Adsorption hysteresis of nitrogen and argon in pore networks and characterization of novel micro- and mesoporous silicas, *Langmuir* 22 (2006) 756-764.
- [37] J.P. Olivier, Improving the models used for calculating the size distribution of micropore volume of activated carbons from adsorption data, *Carbon* 36 (1998) 1469-1472.
- [38] J.P. Olivier, Modeling Physical Adsorption on Porous and Nonporous Solids Using Density Functional Theory *J. Porous Mater.* 2 (1995) 217.
- [39] T.X. Nguyen, S.K. Bhatia, Characterization of Pore Wall Heterogeneity in Nanoporous Carbons Using Adsorption: the Slit Pore Model Revisited, *The Journal of Physical Chemistry B* 108 (2004) 14032-14042.
- [40] T.X. Nguyen, S.K. Bhatia, Probing the Pore Wall Structure of Nanoporous Carbons Using Adsorption, *Langmuir* 20 (2004) 3532-3535.
- [41] P.I. Ravikovitch, J. Jagiello, D. Tolles, A.V. Neimark, Improved DFT methods for micropore size characterization of activated carbons: role of pore wall heterogeneity, Extended abstracts, Carbon '01 conference. , American Carbon Society, Lexington (Kentucky, USA), 2001.
- [42] E.A. Ustinov, D.D. Do, Modeling of adsorption in finite cylindrical pores by means of density functional theory, *Adsorption-Journal of the International Adsorption Society* 11 (2005) 455-477.
- [43] E.A. Ustinov, D.D. Do, M. Jaroniec, Application of density functional theory to equilibrium adsorption of argon and nitrogen on amorphous silica surface, *Applied Surface Science* 252 (2005) 548-561.
- [44] E.A. Ustinov, D.D. Do, M. Jaroniec, Adsorption of argon and nitrogen in cylindrical pores of MCM-41 materials: application of density functional theory, *Applied Surface Science* 252 (2005) 1013-1028.
- [45] E.A. Ustinov, D.D. Do, V.B. Fenelonov, Pore size distribution analysis of activated carbons: Application of density functional theory using nongraphitized carbon black as a reference system, *Carbon* 44 (2006) 653-663.
- [46] J. Jagiello, J.P. Olivier, A Simple Two-Dimensional NLDFT Model of Gas Adsorption in Finite Carbon Pores. Application to Pore Structure Analysis, *The Journal of Physical Chemistry C* 113 (2009) 19382-19385.
- [47] J. Jagiello, J. Kenvin, J. Olivier, A. Lupini, C. Contescu, Using a New Finite Slit Pore Model for NLDFT Analysis of Carbon Pore Structure, *Adsorption Science & Technology* 29 (2011) 769-780.
- [48] P.I. Ravikovitch, A.V. Neimark, Density functional theory model of adsorption on amorphous and microporous silica materials, *Langmuir* 22 (2006) 11171-11179.
- [49] P.I. Ravikovitch, A.V. Neimark, Density Functional Theory Model of Adsorption on Amorphous and Microporous Solids., in: P.L. Llewellyn, J. Rouquerol, F. Rodrigues-Reinoso, N.A. Seaton (Eds.), *Characterisation of Porous Solids VII*, Elsevier, 2006, pp. 9-16.
- [50] G.Y. Gor, M. Thommes, K.A. Cychosz, A.V. Neimark, Quenched solid density functional theory method for characterization of mesoporous carbons by nitrogen adsorption, *Carbon* 50 (2012) 1583-1590.

- [51] G.A. Zickler, S. Jahnert, W. Wagermaier, S.S. Funari, G.H. Findenegg, O. Paris, Physisorbed films in periodic mesoporous silica studied by in situ synchrotron small-angle diffraction, *Physical Review B* 73 (2006) 10.
- [52] N. Muroyama, T. Ohsuna, R. Ryoo, Y. Kubota, O. Terasaki, An Analytical Approach to Determine the Pore Shape and Size of MCM-41 Materials from X-ray Diffraction Data, *The Journal of Physical Chemistry B* 110 (2006) 10630-10635.
- [53] K. Miyasaka, A.V. Neimark, O. Terasaki, Density Functional Theory of in Situ Synchrotron Powder X-ray Diffraction on Mesoporous Crystals: Argon Adsorption on MCM-41, *Journal of Physical Chemistry C* 113 (2009) 791-794.
- [54] S.H. Garofalini, A molecular dynamics simulation of the vitreous silica surface, *The Journal of Chemical Physics* 78 (1983) 2069-2072.
- [55] J.M.D. MacElroy, K. Raghavan, Adsorption and diffusion of a Lennard-Jones vapor in microporous silica, *The Journal of Chemical Physics* 93 (1990) 2068-2079.
- [56] A. Roder, W. Kob, K. Binder, Structure and dynamics of amorphous silica surfaces, *The Journal of Chemical Physics* 114 (2001) 7602-7614.
- [57] T. Hofmann, D. Wallacher, P. Huber, R. Birringer, K. Knorr, A. Schreiber, G.H. Findenegg, Small-angle x-ray diffraction of Kr in mesoporous silica: Effects of microporosity and surface roughness, *Physical Review B* 72 (2005) 064122.
- [58] P.I. Ravikovitch, PhD thesis, Yale University, 1998.
- [59] C.L. Lawson, R.J. Hanson, Solving least squares problems, SIAM, Philadelphia, 1995.
- [60] J. Jagiello, Stable Numerical Solution of the Adsorption Integral Equation Using Splines, *Langmuir* 10 (1994) 2778-2785.
- [61] K.A. Cychosz, X. Guo, W. Fan, R. Cimino, G.Y. Gor, M. Tsapatsis, A.V. Neimark, M. Thommes, Characterization of the Pore Structure of Three-Dimensionally Ordered Mesoporous Carbons Using High Resolution Gas Sorption, *Langmuir* 28 (2012) 12647-12654.
- [62] M. Thommes, Textural Characterization of Zeolite and Ordered Mesoporous Materials by Physical Adsorption, in: H. Van Bekkum (Ed.), *Introduction to Zeolite Science and Practice*, Elsevier, 2007, pp. 495-525.
- [63] D. Lässig, J. Lincke, J. Moellmer, C. Reichenbach, A. Moeller, R. Gläser, G. Kalies, K.A. Cychosz, M. Thommes, R. Staudt, H. Krautscheid, A Microporous Copper Metal-Organic Framework with High H₂ and CO₂ Adsorption Capacity at Ambient Pressure, *Angewandte Chemie International Edition* 50 (2011) 10344-10348.
- [64] M. Thommes, K.A. Cychosz, A.V. Neimark, Advanced Physical Adsorption Characterization of Nanoporous Carbons in: J.M.D. Tascon (Ed.), *Novel Carbon Adsorbents*, Elsevier, 2012, pp. 107-145.
- [65] S. Sircar, Gas separation and storage by activated carbons, in: E.J. Bottani, J.M.D. Tascón (Eds.), *Adsorption by carbons*, Elsevier, Oxford, 2008.
- [66] J.M.V. Nabais, C. Laginhas, P.J.M. Carrott, M. Carrott, Thermal conversion of a novel biomass agricultural residue (vine shoots) into activated carbon using activation with CO(2), *Journal of Analytical and Applied Pyrolysis* 87 (2010) 8-13.
- [67] R.B. Rios, F.W.M. Silva, A.E.B. Torres, D.C.S. Azevedo, C.L. Cavalcante, Adsorption of methane in activated carbons obtained from coconut shells using H(3)PO(4) chemical activation, *Adsorption-Journal of the International Adsorption Society* 15 (2009) 271-277.
- [68] T.Y. Zhang, W.P. Walawender, L.T. Fan, Increasing the microporosities of activated carbons, *Separation and Purification Technology* 44 (2005) 247-249.
- [69] M. Almarri, X.L. Ma, C.S. Song, Selective Adsorption for Removal of Nitrogen Compounds from Liquid Hydrocarbon Streams over Carbon- and Alumina-Based Adsorbents, *Industrial & Engineering Chemistry Research* 48 (2009) 951-960.

- [70] R. Rios, J. Silvestre-Albero, A. Sepulveda-Escribano, F. Rodriguez-Reinoso, Liquid phase removal of propanethiol by activated carbon: Effect of porosity and functionality, *Colloids and Surfaces a-Physicochemical and Engineering Aspects* 300 (2007) 180-190.
- [71] J. Burrell, M. Kraus, M. Beckner, R. Cepel, G. Suppes, C. Wexler, P. Pfeifer, Hydrogen storage in engineered carbon nanospaces, *Nanotechnology* 20 (2009) 10.
- [72] L. Donnaperna, L. Duclaux, R. Gadiou, M.P. Hirn, C. Merli, L. Pietrelli, Comparison of adsorption of Remazol Black B and Acidol Red on microporous activated carbon felt, *Journal of Colloid and Interface Science* 339 (2009) 275-284.
- [73] A. Linares-Solano, Cazorla-Amoros, D., Adsorption on activated carbon fibers, in: E.J. Bottani, J.M.D. Tascón (Eds.), *Adsorption by carbons*, Elsevier, Oxford, 2008.
- [74] J.B. Donnet, Bansal, R.Ch., *Carbon Fibers*, Marcel Dekker, 1990.
- [75] D. Lozano-Castello, Cazorla-Amoros, D., Linares-Solano, A., Powered activated carbons and activated carbon fibers for methane storage: a comparative study, *Energy Fuels* 16 (2002) 1321-1328.
- [76] J. Miyamoto, K. Kanoh, K. Kaneko, The addition of mesoporosity to activated carbon fibers by a simple reactivation process, *Carbon* 43 (2005) 855-857.
- [77] Y.H. Chen, Q.L. Wu, N. Pan, J.H. Gong, D. Pan, Rayon-based activated carbon fibers treated with both alkali metal salt and Lewis acid, *Microporous and Mesoporous Materials* 109 (2008) 138-146.
- [78] S.J. Zhang, H.M. Feng, J.P. Wang, H.Q. Yu, Structure evolution and optimization in the fabrication of PVA-based activated carbon fibers, *Journal of Colloid and Interface Science* 321 (2008) 96-102.
- [79] N. Shiratori, K.J. Lee, J. Miyawaki, S.H. Hong, I. Mochida, B. An, K. Yokogawa, J. Jang, S.H. Yoon, Pore Structure Analysis of Activated Carbon Fiber by Microdomain-Based Model, *Langmuir* 25 (2009) 7631-7637.
- [80] S.H. Mushrif, A.D. Rey, H. Tekinalp, Effect of metal salt on the pore structure evolution of pitch-based activated carbon microfibers, *Industrial & Engineering Chemistry Research* 47 (2008) 3883-3890.
- [81] X. Wu, N.C. Gallego, C.I. Contescu, H. Tekinalp, V.V. Bhat, F.S. Baker, M.C. Thies, The effect of processing conditions on microstructure of Pd-containing activated carbon fibers, *Carbon* 46 (2008) 54-61.
- [82] K.S.W. Sing, Overview of physical adsorption by carbons, in: E.J. Bottani, J.M.D. Tascón (Eds.), *Adsorption by Carbons*, Elsevier, Oxford, 2008.
- [83] F. Charretier, F. Jaouen, S. Ruggeri, J.P. Dodelet, Fe/N/C non-precious catalysts for PEM fuel cells: Influence of the structural parameters of pristine commercial carbon blacks on their activity for oxygen reduction, *Electrochimica Acta* 53 (2008) 2925-2938.
- [84] F. Jaouen, M. Lefevre, J.P. Dodelet, M. Cai, Heat-treated Fe/N/C catalysts for O₂ electroreduction: Are active sites hosted in micropores?, *Journal of Physical Chemistry B* 110 (2006) 5553-5558.
- [85] W.J. Braida, J.J. Pignatello, Y.F. Lu, P.I. Ravikovitch, A.V. Neimark, B.S. Xing, Sorption hysteresis of benzene in charcoal particles, *Environmental Science & Technology* 37 (2003) 409-417.
- [86] M. Richou, C. Martin, R. Denoyel, P. Llewellyn, P. Roubin, Microporosity of carbon deposits collected in the Tore Supra tokamak probed by nitrogen and carbon dioxide adsorption, *Carbon* 47 (2009) 109-116.
- [87] R. Schneider, A. Rai, A. Mutzke, M. Warrier, E. Salonen, K. Nordlund, Dynamic Monte-Carlo modeling of hydrogen isotope reactive-diffusive transport in porous graphite, *Journal of Nuclear Materials* 367 (2007) 1238-1242.

- [88] M.M. Calbi, M.W. Cole, S.M. Gatica, M.J. Bojan, G. Stan, Colloquium: Condensed phases of gases inside nanotube bundles, *Reviews of Modern Physics* 73 (2001) 857-865.
- [89] R.B. Hallock, Y.H. Kahng, Adsorption of helium and other gases to carbon nanotubes and nanotube bundles, *Journal of Low Temperature Physics* 134 (2004) 21-30.
- [90] J.W. Jiang, S.I. Sandler, Nitrogen adsorption on carbon nanotube bundles: Role of the external surface, *Physical Review B* 68 (2003) 9.
- [91] F.X. Li, Y. Wang, D.Z. Wang, F. Wei, Characterization of single-wall carbon nanotubes by N₂ adsorption, *Carbon* 42 (2004) 2375-2383.
- [92] O. Byl, J. Liu, J.T. Yates, Etching of carbon nanotubes by ozone - A surface area study, *Langmuir* 21 (2005) 4200-4204.
- [93] C.M. Yang, K. Kaneko, M. Yudasaka, S. Iijima, Effect of purification on pore structure of HiPco single-walled carbon nanotube aggregates, *Nano Letters* 2 (2002) 385-388.
- [94] A. Anson, J. Jagiello, J.B. Parra, M.L. Sanjuan, A.M. Benito, W.K. Maser, M.T. Martinez, Porosity, surface area, surface energy, and hydrogen adsorption in nanostructured carbons, *Journal of Physical Chemistry B* 108 (2004) 15820-15826.
- [95] O. Byl, J. Liu, J.T. Yates, Characterization of single wall carbon nanotubes by nonane preadsorption, *Carbon* 44 (2006) 2039-2044.
- [96] A.V. Neimark, S. Ruetsch, K.G. Kornev, P.I. Ravikovitch, Hierarchical pore structure and wetting properties of single-wall carbon nanotube fibers, *Nano Letters* 3 (2003) 419-423.
- [97] F.K. Katsaros, T.A. Steriotis, G.E. Romanos, M. Konstantakou, A.K. Stubos, N.K. Kanellopoulos, Preparation and characterisation of gas selective microporous carbon membranes, *Microporous and Mesoporous Materials* 99 (2007) 181-189.
- [98] J. Jagiello, W. Betz, Characterization of pore structure of carbon molecular sieves using DFT analysis of Ar and H₂ adsorption data, *Microporous and Mesoporous Materials* 108 (2008) 117-122.
- [99] V.A. Drozdov, O.N. Baklanova, V.A. Likholobov, O.A. Chirkova, T.I. Gulyaeva, Developing the Synthesis of Homogeneously Microporous Carbon Membranes for Selective Extraction and Accumulation of Organic Molecules with a Carbon Unit as a Carrier, *Protection of Metals and Physical Chemistry of Surfaces* 45 (2009) 191-196.
- [100] H.N. Cheng, L.H. Wartelle, K.T. Klasson, J.C. Edwards, Solid-state NMR and ESR studies of activated carbons produced from pecan shells, *Carbon* 48 (2010) 2455-2469.
- [101] I.M. Lima, A.A. Boateng, K.T. Klasson, Physicochemical and adsorptive properties of fast-pyrolysis bio-chars and their steam activated counterparts, *Journal of Chemical Technology and Biotechnology* 85 (2010) 1515-1521.
- [102] K.T. Klasson, I.M. Lima, L.L. Boihem, L.H. Wartelle, Feasibility of mercury removal from simulated flue gas by activated chars made from poultry manures, *Journal of Environmental Management* 91 (2010) 2466-2470.
- [103] K.T. Klasson, I.M. Lima, L.L. Boihem, Poultry manure as raw material for mercury adsorbents in gas applications, *Journal of Applied Poultry Research* 18 (2009) 562-569.
- [104] P.J.M. Carrott, L.M. Marques, M. Carrott, Characterisation of the porosity of polymer and carbon aerogels containing Fe, Ni or Cu prepared from 2,4-dihydroxybenzoic acid by n-nonane pre-adsorption and density functional theory, *Microporous and Mesoporous Materials* 131 (2010) 75-81.
- [105] J. Weber, J. Schmidt, A. Thomas, W. Bohlmann, Micropore Analysis of Polymer Networks by Gas Sorption and (129)Xe NMR Spectroscopy: Toward a Better Understanding of Intrinsic Microporosity, *Langmuir* 26 (2010) 15650-15656.

- [106] M. Thommes, C. Morlay, R. Ahmad, J.P. Joly, Assessing surface chemistry and pore structure of active carbons by a combination of physisorption (H_2O , Ar, N_2 , CO_2), XPS and TPD-MS, *Adsorption-Journal of the International Adsorption Society* 17 (2011) 653-661.
- [107] J. Romanos, M. Beckner, T. Rash, L. Firlej, B. Kuchta, P. Yu, G. Suppes, C. Wexler, P. Pfeifer, Nanospace engineering of KOH activated carbon, *Nanotechnology* 23 (2012) 7.
- [108] X. Hu, M. Radosz, K.A. Cychosz, M. Thommes, CO_2 -Filling Capacity and Selectivity of Carbon Nanopores: Synthesis, Texture, and Pore-Size Distribution from Quenched-Solid Density Functional Theory (QSDFT), *Environmental Science & Technology* 45 (2011) 7068-7074.
- [109] K. Yang, X.C. Lu, Y.Z. Lin, A.V. Neimark, Effects of CO_2 adsorption on coal deformation during geological sequestration, *Journal of Geophysical Research-Solid Earth* 116 (2011) 11.
- [110] A.M. Puziy, O.I. Poddubnaya, B. Gawdzik, M. Sobiesiak, C.A. Reinish, M.M. Tsyba, T.P. Segeda, M.I. Danylenko, Nanostructured carbons for solid phase extraction, *Applied Surface Science* 256 (2010) 5216-5220.
- [111] S.H. Yeon, I. Knoke, Y. Gogotsi, J.E. Fischer, Enhanced volumetric hydrogen and methane storage capacity of monolithic carbide-derived carbon, *Microporous and Mesoporous Materials* 131 (2010) 423-428.
- [112] L.L. He, S.M. Chathoth, Y.B. Melnichenko, V. Presser, J. McDonough, Y. Gogotsi, Small-angle neutron scattering characterization of the structure of nanoporous carbons for energy-related applications, *Microporous and Mesoporous Materials* 149 (2012) 46-54.
- [113] Y.W. Zhu, S. Murali, M.D. Stoller, K.J. Ganesh, W.W. Cai, P.J. Ferreira, A. Pirkle, R.M. Wallace, K.A. Cychosz, M. Thommes, D. Su, E.A. Stach, R.S. Ruoff, Carbon-Based Supercapacitors Produced by Activation of Graphene, *Science* 332 (2011) 1537-1541.
- [114] M.M. Jaramillo, A. Mendoza, S. Vaquero, M. Anderson, J. Palma, R. Marcilla, Role of Textural Properties and Surface Functionalities of Selected Carbons on the Electrochemical Behaviour of Ionic Liquid based-Supercapacitors, *RSC Advances* (2012) xx-xx.
- [115] K. Jost, C.R. Perez, J.K. McDonough, V. Presser, M. Heon, G. Dion, Y. Gogotsi, Carbon coated textiles for flexible energy storage, *Energy & Environmental Science* 4 (2011) 5060-5067.
- [116] S. Jun, S.H. Joo, R. Ryoo, M. Kruk, M. Jaroniec, Z. Liu, T. Ohsuna, O. Terasaki, Synthesis of new, nanoporous carbon with hexagonally ordered mesostructure, *Journal of the American Chemical Society* 122 (2000) 10712-10713.
- [117] H. Zhou, S. Zhu, M. Hibino, I. Honma, M. Ichihara, Lithium Storage in Ordered Mesoporous Carbon (CMK-3) with High Reversible Specific Energy Capacity and Good Cycling Performance, *Advanced Materials* 15 (2003) 2107-2111.
- [118] A. Vinu, M. Miyahara, K. Ariga, Biomaterial Immobilization in Nanoporous Carbon Molecular Sieves: Influence of Solution pH, Pore Volume, and Pore Diameter, *The Journal of Physical Chemistry B* 109 (2005) 6436-6441.
- [119] S.H. Joo, R. Ryoo, M. Kruk, M. Jaroniec, Evidence for General Nature of Pore Interconnectivity in 2-Dimensional Hexagonal Mesoporous Silicas Prepared Using Block Copolymer Templates, *The Journal of Physical Chemistry B* 106 (2002) 4640-4646.
- [120] W. Fan, M.A. Snyder, S. Kumar, P.S. Lee, W.C. Yoo, A.V. McCormick, R.L. Penn, A. Stein, M. Tsapatsis, Hierarchical nanofabrication of microporous crystals with ordered mesoporosity, *Nature Materials* 7 (2008) 984-991.
- [121] A. Vishnyakov, A.V. Neimark, Monte Carlo Simulation Test of Pore Blocking Effects, *Langmuir* 19 (2003) 3240-3247.

- [122] G.Y. Gor, C.J. Rasmussen, A.V. Neimark, Capillary Condensation Hysteresis in Overlapping Spherical Pores: A Monte Carlo Simulation Study, *Langmuir* 28 (2012) 12100-12107.
- [123] H. Darmstadt, R. Ryoo, Adsorption on ordered porous carbons, in: E.J. Bottani, J.M.D. Tascón (Eds.), *Adsorption by carbons*, Elsevier, Oxford, 2008.
- [124] K.T. Lee, S.M. Oh, Novel synthesis of porous carbons with tunable pore size by surfactant-templated sol-gel process and carbonisation, *Chemical Communications* (2002) 2722-2723.
- [125] R. Ryoo, S.H. Joo, J.M. Kim, Energetically favored formation of MCM-48 from cationic-neutral surfactant mixtures, *Journal of Physical Chemistry B* 103 (1999) 7435-7440.
- [126] M. Kruk, M. Jaroniec, R. Ryoo, S.H. Joo, Characterization of MCM-48 silicas with tailored pore sizes synthesized via a highly efficient procedure, *Chemistry of Materials* 12 (2000) 1414-1421.
- [127] A. Wilke, J. Weber, Mesoporous Polymer Networks-Ultraporous DVB Resins by Hard-Templating of Close-Packed Silica Spheres, *Macromolecular Rapid Communications* 33 (2012) 785-790.
- [128] C.J. Rasmussen, A. Vishnyakov, M. Thommes, B.M. Smarsly, F. Kleitz, A.V. Neimark, Cavitation in Metastable Liquid Nitrogen Confined to Nanoscale Pores, *Langmuir* 26 (2010) 10147-10157.
- [129] A. Monnier, F. Schuth, Q. Huo, D. Kumar, D. Margolese, R.S. Maxwell, G.D. Stucky, M. Krishnamurty, P. Petroff, A. Firouzi, M. Janicke, B.F. Chmelka, Cooperative formation of inorganic-organic interfaces in the synthesis of silicate mesostructures, *Science* 261 (1993) 1299-1303.
- [130] C.Y. Chen, S.Q. Xiao, M.E. Davis, Studies on ordered mesoporous materials 3. comparison of MCM-41 to mesoporous materials derived from kanemite, *Microporous Materials* 4 (1995) 1-20.
- [131] S. Inagaki, Y. Sakamoto, Y. Fukushima, O. Terasaki, Pore wall of a mesoporous molecular sieve derived from kanemite, *Chemistry of Materials* 8 (1996) 2089-2095.
- [132] C.-Y. Chen, H.-X. Li, M.E. Davis, Studies on mesoporous materials: I. Synthesis and characterization of MCM-41, *Microporous Materials* 2 (1993) 17-26.
- [133] P.I. Ravikovitch, A.V. Neimark, Calculations of pore size distributions in nanoporous materials from adsorption and desorption isotherms, in: A. Sayari, M. Jaroniec (Eds.), *Studies in Surface Science and Catalysis*, Elsevier, 2000, pp. 597-606.
- [134] K. Schumacher, P.I. Ravikovitch, A. Du Chesne, A.V. Neimark, K.K. Unger, Characterization of MCM-48 materials, *Langmuir* 16 (2000) 4648-4654.
- [135] V. Alfredsson, M.W. Anderson, Structure of MCM-48 revealed by transmission electron microscopy, *Chemistry of Materials* 8 (1996) 1141-1146.
- [136] F. Kleitz, F. Berube, R. Guillet-Nicolas, C.M. Yang, M. Thommes, Probing Adsorption, Pore Condensation, and Hysteresis Behavior of Pure Fluids in Three-Dimensional Cubic Mesoporous KIT-6 Silica, *Journal of Physical Chemistry C* 114 (2010) 9344-9355.
- [137] W. Guo, F. Kleitz, K. Cho, R. Ryoo, Large pore phenylene-bridged mesoporous organosilica with bicontinuous cubic Ia(3)over-bard (KIT-6) mesostructure, *Journal of Materials Chemistry* 20 (2010) 8257-8265.
- [138] J.H. Clark, D.J. Macquarrie, Catalysis of liquid phase organic reactions using chemically modified mesoporous inorganic solids, *Chemical Communications* (1998) 853-860.
- [139] A.P. Wight, M.E. Davis, Design and preparation of organic-inorganic hybrid catalysts, *Chemical Reviews* 102 (2002) 3589-3613.

- [140] G. Kickelbick, Hybrid inorganic-organic mesoporous materials, *Angewandte Chemie-International Edition* 43 (2004) 3102-3104.
- [141] H. Yoshitake, Highly-controlled synthesis of organic layers on mesoporous silica: their structure and application to toxic ion adsorptions, *New Journal of Chemistry* 29 (2005) 1107-1117.
- [142] F. Hoffmann, M. Cornelius, J. Morell, M. Froba, Silica-based mesoporous organic-inorganic hybrid materials, *Angewandte Chemie-International Edition* 45 (2006) 3216-3251.
- [143] D.M. Ford, E.E. Simanek, D.F. Shantz, Engineering nanospaces: ordered mesoporous silicas as model substrates for building complex hybrid materials, *Nanotechnology* 16 (2005) S458-S475.
- [144] A. Taguchi, F. Schuth, Ordered mesoporous materials in catalysis, *Microporous and Mesoporous Materials* 77 (2005) 1-45.
- [145] J.Y. Ying, C.P. Mehnert, M.S. Wong, Synthesis and applications of supramolecular-templated mesoporous materials, *Angewandte Chemie-International Edition* 38 (1999) 56-77.
- [146] M. Vallet-Regi, F. Balas, D. Arcos, Mesoporous materials for drug delivery, *Angewandte Chemie-International Edition* 46 (2007) 7548-7558.
- [147] M. Tiemann, Porous metal oxides as gas sensors, *Chemistry-a European Journal* 13 (2007) 8376-8388.
- [148] M. Hartmann, Ordered mesoporous materials for bioadsorption and biocatalysis, *Chemistry of Materials* 17 (2005) 4577-4593.
- [149] M. Choi, F. Kleitz, D.N. Liu, H.Y. Lee, W.S. Ahn, R. Ryoo, Controlled polymerization in mesoporous silica toward the design of organic-inorganic composite nanoporous materials, *Journal of the American Chemical Society* 127 (2005) 1924-1932.
- [150] R. Guillet-Nicolas, L. Marcoux, F. Kleitz, Insights into pore surface modification of mesoporous polymer-silica composites: introduction of reactive amines, *New Journal of Chemistry* 34 (2010) 355-366.
- [151] S.J. Gregg, K.S.W. Sing, *Adsorption, Surface Area and Porosity*, Academic, London, 1982.
- [152] Q.S. Huo, D.I. Margolese, U. Ciesla, P.Y. Feng, T.E. Gier, P. Sieger, R. Leon, P.M. Petroff, F. Schuth, G.D. Stucky, Generalized synthesis of periodic surfactant inorganic composite-materials, *Nature* 368 (1994) 317-321.
- [153] Q.S. Huo, R. Leon, P.M. Petroff, G.D. Stucky, Mesostructure design with gemini surfactants - supercage formation in a 3-dimensional hexagonal array, *Science* 268 (1995) 1324-1327.
- [154] Q.S. Huo, D.I. Margolese, G.D. Stucky, Surfactant control of phases in the synthesis of mesoporous silica-based materials, *Chemistry of Materials* 8 (1996) 1147-1160.
- [155] M. Imperor-Clerc, P. Davidson, A. Davidson, Existence of a microporous corona around the mesopores of silica-based SBA-15 materials templated by triblock copolymers, *J. Am. Chem. Soc.* 122 (2000) 11925-11933.
- [156] X.Y. Bao, X.S. Zhao, X. Li, J. Li, Pore structure characterization of large-pore periodic mesoporous organosilicas synthesized with varying SiO₂/template ratios, *Applied Surface Science* 237 (2004) 380-386.
- [157] Y.C. Hsu, Y.T. Hsu, H.Y. Hsu, C.M. Yang, Facile synthesis of mesoporous silica SBA-15 with additional intra-particle porosities, *Chemistry of Materials* 19 (2007) 1120-1126.
- [158] R.A. Pollock, B.R. Walsh, J. Fry, I.T. Ghampson, Y.B. Melnichenko, H. Kaiser, R. Pynn, W.J. DeSisto, M.C. Wheeler, B.G. Frederick, Size and Spatial Distribution of Micropores in SBA-15 using CM-SANS, *Chemistry of Materials* 23 (2011) 3828-3840.

- [159] R.A. Pollock, G.Y. Gor, B.R. Walsh, J. Fry, I.T. Ghampson, Y.B. Melnichenko, H. Kaiser, W.J. DeSisto, M.C. Wheeler, B.G. Frederick, Role of Liquid vs Vapor Water in the Hydrothermal Degradation of SBA-15, *The Journal of Physical Chemistry C* 116 (2012) 22802-22814.
- [160] T. Blasco, A. Corma, M.T. Navarro, J.P. Pariente, Synthesis, characterization, and catalytic activity of Ti-MCM-41 structures, *Journal of Catalysis* 156 (1995) 65-74.
- [161] F. Berube, A. Khadhraoui, M.T. Janicke, F. Kleitz, S. Kaliaguine, Optimizing Silica Synthesis for the Preparation of Mesoporous Ti-SBA-15 Epoxidation Catalysts, *Industrial & Engineering Chemistry Research* 49 (2010) 6977-6985.
- [162] F. Berube, F. Kleitz, S. Kaliaguine, A comprehensive study of titanium-substituted SBA-15 mesoporous materials prepared by direct synthesis, *Journal of Physical Chemistry C* 112 (2008) 14403-14411.
- [163] F. Berube, B. Nohair, F. Kleitz, S. Kaliaguine, Controlled Postgrafting of Titanium Chelates for Improved Synthesis of Ti-SBA-15 Epoxidation Catalysts, *Chemistry of Materials* 22 (2010) 1988-2000.
- [164] P.I. Ravikovitch, A.V. Neimark, Characterization of nanoporous materials from adsorption and desorption isotherms, *Colloids and Surfaces a-Physicochemical and Engineering Aspects* 187 (2001) 11-21.
- [165] A. Szegedi, M. Popova, C. Minchev, Catalytic activity of Co/MCM-41 and Co/SBA-15 materials in toluene oxidation, *Journal of Materials Science* 44 (2009) 6710-6716.
- [166] T. Tsoncheva, L. Ivanova, R. Dimitrova, J. Rosenholm, Physicochemical and catalytic properties of grafted vanadium species on different mesoporous silicas, *Journal of Colloid and Interface Science* 321 (2008) 342-349.
- [167] M.L. Ojeda, A. Campero, C. Velasquez, J.G. Lopez-Cortes, C. Alvarez, J.M. Esparza, F. Rojas, SBA-15 surface functionalization via ferrocenyl Fischer chromium carbene coatings: Technology and textural properties, *Surface & Coatings Technology* 203 (2009) 1444-1451.
- [168] M.L. Ojeda, C. Velasquez, A. Campero, J.G. Lopez-Cortes, C. Alvarez, J.M. Esparza, F. Rojas, SBA-15 pore-width decrease via a one- or a two-step covalent bonding of a Fischer tungsten carbene as measured by N(2) sorption, *Surface and Interface Analysis* 40 (2008) 1262-1269.
- [169] D.P. Serrano, J. Aguado, G. Morales, J.M. Rodriguez, A. Peral, M. Thommes, J.D. Epping, B.F. Chmelka, Molecular and Meso- and Macroscopic Properties of Hierarchical Nanocrystalline ZSM-5 Zeolite Prepared by Seed Silanization, *Chemistry of Materials* 21 (2009) 641-654.
- [170] H.C. Li, Y. Sakamoto, Z. Liu, T. Ohsuna, O. Terasaki, M. Thommes, S.N. Che, Mesoporous silicalite-1 zeolite crystals with unique pore shapes analogous to the morphology, *Microporous and Mesoporous Materials* 106 (2007) 174-179.
- [171] M. Thommes, S. Mitchell, J. Perez-Ramirez, Surface and Pore Structure Assessment of Hierarchical MFI Zeolites by Advanced Water and Argon Sorption Studies, *The Journal of Physical Chemistry C* 116 (2012) 18816-18823.
- [172] J. Moellmer, E.B. Celer, R. Luebke, A.J. Cairns, R. Staudt, M. Eddaoudi, M. Thommes, Insights on Adsorption Characterization of Metal-Organic Frameworks: A Benchmark Study on the Novel soc-MOF, *Microporous and Mesoporous Materials* 129 (2010) 345-353.
- [173] A.P. Cote, A.I. Benin, N.W. Ockwig, M. O'Keeffe, A.J. Matzger, O.M. Yaghi, Porous, crystalline, covalent organic frameworks, *Science* 310 (2005) 1166-1170.
- [174] H. Furukawa, O.M. Yaghi, Storage of Hydrogen, Methane, and Carbon Dioxide in Highly Porous Covalent Organic Frameworks for Clean Energy Applications, *Journal of the American Chemical Society* 131 (2009) 8875-8883.

- [175] J. Kullmann, D. Enke, S. Thraenert, R. Krause-Rehberg, A. Inayat, Characterization of nanoporous monoliths using nitrogen adsorption and positronium annihilation lifetime spectroscopy, *Colloids and Surfaces a-Physicochemical and Engineering Aspects* 357 (2010) 17-20.
- [176] F. Chavez, C. Felipe, E. Lima, V. Lara, C. Angeles-Chavez, M.A. Hernandez, Preparation of self-organized porous tungsten oxide using HFCVD technique, *Materials Chemistry and Physics* 120 (2010) 36-41.
- [177] L. Zhou, Q.J. Ren, X.F. Zhou, J.W. Tang, Z.H. Chen, C.Z. Yu, Comprehensive understanding on the formation of highly ordered mesoporous tungsten oxides by X-ray diffraction and Raman spectroscopy, *Microporous and Mesoporous Materials* 109 (2008) 248-257.
- [178] D. Chandra, S. Mridha, D. Basak, A. Bhaumik, Template directed synthesis of mesoporous ZnO having high porosity and enhanced optoelectronic properties, *Chemical Communications* (2009) 2384-2386.
- [179] J. Landers, M. Devadas, A.V. Neimark, H.K. Timken, A. Ojo, A.W. Chester, Effect of Mixing on the Pore Structure of Alumina Extrudates, *Particle & Particle Systems Characterization* 27 (2010) 42-47.
- [180] K. Miyasaka, H. Hano, Y. Kubota, Y. Lin, R. Ryoo, M. Takata, S. Kitagawa, A.V. Neimark, O. Terasaki, A Stand-Alone Mesoporous Crystal Structure Model from in situ X-ray Diffraction: Nitrogen Adsorption on 3D Cagelike Mesoporous Silica SBA-16, *Chemistry - A European Journal* 18 (2012) 10300-10311.
- [181] A. Vinu, V. Murugesan, M. Hartmann, Pore size engineering and mechanical stability of the cubic mesoporous molecular sieve SBA-1, *Chemistry of Materials* 15 (2003) 1385-1393.
- [182] C.C. Ting, H.Y. Wu, A. Palani, A.S.T. Chiang, H.M. Kao, Facile synthesis and morphology control of highly ordered cubic mesoporous silica SBA-1 using short chain dodecyltrimethylammonium chloride as the structure-directing agent, *Microporous and Mesoporous Materials* 116 (2008) 323-329.
- [183] H.M. Kao, C.C. Ting, A.S.T. Chiang, C.C. Teng, C.H. Chen, Facile synthesis of stable cubic mesoporous silica SBA-1 over a broad temperature range with the aid of D-fructose, *Chemical Communications* (2005) 1058-1060.
- [184] H.M. Kao, J.D. Wu, C.C. Cheng, A.S.T. Chiang, Direct synthesis of vinyl-functionalized cubic mesoporous silica SBA-1, *Microporous and Mesoporous Materials* 88 (2006) 319-328.
- [185] H.M. Kao, C.H. Liao, T.T. Hung, Y.C. Pan, A.S.T. Chiang, Direct synthesis and solid-state NMR characterization of cubic mesoporous silica SBA-1 functionalized with phenyl groups, *Chemistry of Materials* 20 (2008) 2412-2422.
- [186] D.Y. Zhao, Q.S. Huo, J.L. Feng, B.F. Chmelka, G.D. Stucky, Nonionic triblock and star diblock copolymer and oligomeric surfactant syntheses of highly ordered, hydrothermally stable, mesoporous silica structures, *Journal of the American Chemical Society* 120 (1998) 6024-6036.
- [187] C.Z. Yu, Y.H. Yu, D.Y. Zhao, Highly ordered large caged cubic mesoporous silica structures templated by triblock PEO-PBO-PEO copolymer, *Chemical Communications* (2000) 575-576.
- [188] T. Yu, H. Zhang, X.W. Yan, Z.X. Chen, X.D. Zou, P. Oleynikov, D.Y. Zhao, Pore structures of ordered large cage-type mesoporous silica FDU-12s, *Journal of Physical Chemistry B* 110 (2006) 21467-21472.
- [189] J.M. Esparza, M.L. Ojeda, A. Campero, G. Hernandez, C. Felipe, M. Asomoza, S. Cordero, I. Kornhauser, F. Rojas, Development and sorption characterization of some model mesoporous and microporous silica adsorbents, *Journal of Molecular Catalysis a-Chemical* 228 (2005) 97-110.

- [190] F. Kleitz, T. Czuryzkiewicz, L.A. Solovyov, M. Linden, X-ray structural modeling and gas adsorption analysis of cage-like SBA-16 silica mesophases prepared in a F127/butanol/H₂O system, *Chemistry of Materials* 18 (2006) 5070-5079.
- [191] F. Kleitz, T.W. Kim, R. Ryoo, Phase domain of the cubic im3m mesoporous silica in the EO106PO70EO106-butanol-H₂O system, *Langmuir* 22 (2006) 440-445.
- [192] J. Fan, C.Z. Yu, J. Lei, Q. Zhang, T.C. Li, B. Tu, W.Z. Zhou, D.Y. Zhao, Low-temperature strategy to synthesize highly ordered mesoporous silicas with very large pores, *Journal of the American Chemical Society* 127 (2005) 10794-10795.
- [193] Y. Meng, D. Gu, F.Q. Zhang, Y.F. Shi, H.F. Yang, Z. Li, C.Z. Yu, B. Tu, D.Y. Zhao, Ordered mesoporous polymers and homologous carbon frameworks: Amphiphilic surfactant templating and direct transformation, *Angewandte Chemie-International Edition* 44 (2005) 7053-7059.
- [194] F. Kleitz, D.N. Liu, G.M. Anilkumar, I.S. Park, L.A. Solovyov, A.N. Shmakov, R. Ryoo, Large cage face-centered-cubic Fm3m mesoporous silica: Synthesis and structure, *Journal of Physical Chemistry B* 107 (2003) 14296-14300.
- [195] C.M. Yang, W. Schmidt, F. Kleitz, Pore topology control of three-dimensional large pore cubic silica mesophases, *Journal of Materials Chemistry* 15 (2005) 5112-5114.
- [196] C.Y. Wu, Y.T. Hsu, C.M. Yang, Structural modulation of cage-like mesoporous KIT-5 silica by post-synthesis treatments with ammonia and/or sulfuric acid, *Microporous and Mesoporous Materials* 117 (2009) 249-256.
- [197] N. Muroyama, A. Yoshimura, Y. Kubota, K. Miyasaka, T. Ohsuna, R. Ryoo, P.I. Ravikovitch, A.V. Neimark, M. Takata, O. Terasaki, Argon adsorption on MCM-41 mesoporous crystal studied by in situ synchrotron powder X-ray diffraction, *Journal of Physical Chemistry C* 112 (2008) 10803-10813.
- [198] A.V. Neimark, Percolation Theory of Capillary Hysteresis Phenomena and Its Application for Characterization of Porous Solids, in: F. Rodriguez-Reinoso, J. Rouquerol, K.S.W. Sing, K.K. Unger (Eds.), *Studies in Surface Science and Catalysis*, Elsevier, 1991, pp. 67-74.
- [199] P.A. Monson, Understanding adsorption/desorption hysteresis for fluids in mesoporous materials using simple molecular models and classical density functional theory, *Microporous and Mesoporous Materials* 160 (2012) 47-66.
- [200] C.J. Gommers, Adsorption, Capillary Bridge Formation, and Cavitation in SBA-15 Corrugated Mesopores: A Derjaguin-Broekhoff-de Boer Analysis, *Langmuir* 28 (2012) 5101-5115.
- [201] G.Y. Gor, A.V. Neimark, Adsorption-Induced Deformation of Mesoporous Solids, *Langmuir* 26 (2010) 13021-13027.
- [202] G. Guenther, J. Prass, O. Paris, M. Schoen, Novel insights into nanopore deformation caused by capillary condensation, *Physical Review Letters* 101 (2008) 086104.
- [203] C. Balzer, T. Wildhage, S. Braxmeier, G. Reichenauer, J.P. Olivier, Deformation of Porous Carbons upon Adsorption, *Langmuir* 27 (2011) 2553-2560.
- [204] P. Kowalczyk, A. Ciach, A.V. Neimark, Adsorption-induced deformation of microporous carbons: Pore size distribution effect, *Langmuir* 24 (2008) 6603-6608.
- [205] G. Reichenauer, G.W. Scherer, Nitrogen adsorption in compliant materials, *J. Non-Cryst. Solids* 277 (2000) 162-172.
- [206] A.V. Neimark, F.X. Coudert, A. Boutin, A.H. Fuchs, Stress-Based Model for the Breathing of Metal-Organic Frameworks, *J. Phys. Chem. Lett.* 1 (2010) 445-449.

- [207]. K. Yang, X. Lu, Y. Lin, and A.V. Neimark, - Deformation of coal induced by methane adsorption at geological conditions, *Energy&Fuel*, 2010, V.24, p.5955–5964.
- [208] K. Yang, X. Lu, Y. Lin, and A.V. Neimark, - Effects of coal deformation upon CO₂ adsorption and sequestration, *Journal of Geophysical Research - Solid Earth*, 2011, V.116, B08212.
- [209] K. Yang, X. Lu, Y. Lin, and A.V. Neimark, - Solvation Forces between Molecularly Rough Surfaces, *Journal of Colloid and Interface Science*, 2011, V.362, p.382-388.
- [210] R. Cimino, K. A. Cychos, M. Thommes, and A. V. Neimark, - Theoretical and Experimental Studies of Scanning Isotherms, - *Colloids and Surfaces A*, this issue.

Highlights

The state-of-the-art DFT methods for adsorption characterization of micro- and mesoporous materials is presented.

DFT allows for the customization to different adsorbates, materials and pore geometries.

A rigorous theoretical background is provided for the development of both NLDFT and QSDFT methods.

A wealth of examples is provided for practitioners that serve as a guide to which kernel to choose from.

Hysteresis due to capillary condensation, cavitation and pore blocking and how to distinguish among them is discussed.